Establishing Fluid Dynamics Scales Critical to Dynamic Interface Applications and their Impact on Handling Qualities

Quarterly Status Report 3

Period of Performance: 9/5/2021 – 12/4/2021

Prepared by:

G. R. Whitehouse
Continuum Dynamics, Inc.
34 Lexington Avenue
Ewing, NJ 08618-2302

Prepared for:

David Gonzalez
Office of Naval Research
875 North Randolph
Street
Arlington VA 22203

Under Contract No. N00014-21-C-1044

Glen R. Whitehouse

December 8, 2021

Project Summary

One of the most demanding tasks for naval aviators is landing on a moving flight deck in high sea-states (i.e. the dynamic interface (DI) problem - see Figure 1). This task is made even more difficult by aerodynamic disturbances at the landing spot from the flow around the ship's bow, superstructure and deck edges. This highly unsteady ship airwake can lead to significant pilot workload. Flight simulation has long been recognized as a valuable tool for augmenting engineering development and pilot training in DI operations, however, it is most effective when the underlying simulation model has appropriately characterized the complex aerodynamic interactions between the rotorcraft and ship airwake. Given the complexity of the problem, a fundamental difficulty when assessing the simulation approaches is the quantification of "good enough", both from the standpoint of understanding and predicting the underlying physics and also with regards to trainer fidelity (i.e. can the pilot feel/tell a difference). The premise of the proposed effort is to quantify "good enough" with regards to understanding the fundamental aero-physics of a rotorcraft interacting with an external disturbance field to quantify which length and time scales - such as those present in a ship airwake or in the wake of a an upstream aircraft during formation flight/refueling - directly impact the aircraft's fundamental response and flying qualities (FQ) along with the aeromechanics modeling fidelity required to simulate interactions adequately.

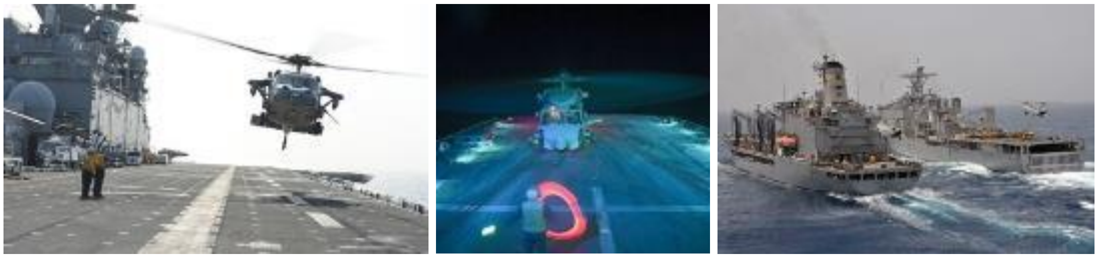

Figure 1: DI scenarios: landing on a moving deck (left), night operations (center) and approaching a pair ships (right)

Several ONR funded efforts that seek to quantify "good enough" have recently completed, or are underway, at the University of Maryland, Georgia Institute of Technology and NAVAIR, where the academic researchers are focusing on understanding the response of a wing to the wake shed by canonical structures [1] and the latter (Generalized Airwake Goodness Evaluation) program seeks to represent the entire DI scenario with a variety of methods. This effort does not seek to duplicate that work, rather to complement it by focusing on several fundamental unknowns in the rotorcraft community, namely:

1. What spatial and temporal scales, present in a disturbance field, matter from Flight Dynamics (FD) and FQ standpoints? Beyond the obvious constraints (i.e. larger than a rotor radius and those that induce velocities larger than the wake induced velocity), how does a rotor respond to different size disturbances and how does the rotor type influence this? For example, in general, a rotor acts to filter the influence of a disturbance field, but the level of filtering will vary significantly between an articulated flexible rotor (H-60) and a gimballed stiff one (V-22). Moreover, rotors typically respond ~90^{o} out of phase of the disturbance, whereas fixed aerodynamic surfaces response directly in-phase, which results in a fundamentally different response between rotorcraft types (i.e. helicopter vs. tiltrotor).

2. How do these scales vary when the effects on the full aircraft are accounted for? The primary response from the helicopter will be dominated by that of the rotor, though there may still be significant response associated with the disturbance induced flow on the fuselage, empennage and tail rotor.
3. How do these scales vary with aircraft configuration/type (i.e. conventional helicopter vs. tiltrotor)? The primary response from the helicopter will be dominated by that of the rotor, whereas the tiltrotor may respond primarily in a fixed wing manner associated with the induced flow on the wing. Of course, the tiltrotor's response will also vary with nacelle angle, and it is well known that the V-22's response to wake disturbances (i.e. during formation flight) is quite different to other rotorcraft in the Navy's inventory [2].
4. How do these scales vary with aircraft flight condition, and can valid modeling simplifications be made (i.e. distorting vs. classical frozen disturbance field)? Work by Whitehouse and Brown for helicopter rotors [3-7] suggests that for high speed flight, the traditional frozen field (superposition) assumption may be adequate, but that at the low speeds associated with DI operations, a distorting disturbance field and wake are required because the response is critically different.

Developing an understanding of fundamental aircraft aeromechanic response, FD, and FQ to the unknowns outlined above would provide great utility to the community with regards to establishing the level of modeling fidelity required to accurately simulate disturbance interactions, the level of fidelity required to be output by CFD simulation generated ship airwake databases for training scenarios, and the quantification and specification of handling qualities to types of disturbance fields that can be used to define future and ongoing training and aircraft performance requirements and specifications, such as ADS-33 [8].

Technical Objectives

The goal of the effort is to develop a fundamental understanding of the relationship between the length and time scales typically present in disturbance fields experienced by Naval aviators (i.e. ship airwakes, wing wakes etc.) and rotorcraft FD and FQ when the fully-interacting fluid dynamics of the airwake and rotor wake and flight mechanics are accounted for. With this information in hand, the engineering community would be better able to understand the relationship between aircraft type, ride quality, FD and FQ during flight conditions where disturbance fields are encountered. The community would be able to more accurately define trainer requirements, minimum experimental campaign requirements, minimum CFD modeling requirements and consequently establish a benchmark to evaluate CFD predictive capability. Furthermore, the conclusions of this work would also directly impact the development of requirements for new aircraft given the direct correlation between FD and FQ. The proposed effort would undertake the research required to develop such an understanding, with disseminating the observations and conclusions of the work to the Navy and the broader FD, FQ and handling qualities communities - a key objective from the outset. The effort will be structured using a build-up approach that first focuses on defining relevant disturbance fields followed by predicting and understanding the fundamental aeromechanics response (i.e. aerodynamic forces and moments and rotor dynamics). The effort would culminate in predicting the flight dynamics and handling qualities for realistic, but generic, helicopter and tiltrotor configurations that include representations of flight controls, propulsion system and crosscoupling characteristics. The key objectives for the effort roughly form the main tasks and are as follows:

1. Define the spatial and temporal fluid dynamic scales present in relevant disturbance fields and develop numerical representations for testing (Year 1).
2. 6-DOF generic model assembly and shakedown testing to ensure correct operation and functionality.(Year 1)
3. Define aeromechanics performance and HQ metrics along with a detailed simulation test matrix that includes systematic and consistent model fidelity build-up (Year 1-2).
4. Undertake simulation of a generic helicopter interacting with frozen and distorting disturbance fields to establish fundamental response characteristics (Year 2).
5. Undertake simulation of a generic tiltrotor interacting with frozen and distorting disturbance fields to establish fundamental response characteristics (Year 2).
6. Develop a realistic full helicopter model and undertake simulations of interactions with frozen and distorting disturbance fields to establish flight dynamics and handling qualities response (Year 3).
7. Develop a realistic full tiltrotor model and undertake simulations of interactions with frozen and distorting disturbance fields to establish flight dynamics and handling qualities response (Year 3).
8. Documentation and dissemination of observations and conclusions to the Navy and the wider FD/HQ community (Years 1-3).

Summary of Work Conducted During Reporting Period

During this reporting period work has continued investigating the type of disturbance fields experienced by Naval aviators, and how to define the relevant primary flow structures and time scales. Emphasis was placed on characterizing corner flows, wake parameterization and setting up CFD predictions to provide insight into cases where the literature is lacking. As in prior reports, the initial discussion presented in the prior progress reports is included in the write-up below for contextual clarity.

Discussions were also held with engineers at NAVAIR’s Manned Flight Simulator (MFS) in regards to the procedure to obtain permission to use the Navy’s CASTLE simulation environment, the example helicopter model and a tiltrotor model for this project. From discussions, it appears that the general request process is fairly straightforward and procedurally consists of an email request to Alex Kokolios and/or Keith Balderson from either CDI or ONR program personnel on CDI’s behalf. MFS program personnel see no reason why access to CASTLE and/or the H-60 example helicopter model would be denied.

At this time, MFS has not developed a generic tiltrotor model for use with CASTLE, and thus a request use to the V-22 model would have to be made in order to support the project. Given the proprietary nature of some of the components in the CASTLE V-22 model, NAVAIR/MFS restricts access to this model on an as needed basis. Since the CASTLE V-22 model is not explicitly called out as Government-Furnished Software in the contract/SOW, it is therefore recommended that during the next period of performance CDI, MFS and ONR program personnel liaise with each other in order to simplify and expedite the request process as much as possible. For example, it may be advisable for CDI to request (and carbon copy ONR personnel) access to CASTLE and the example helicopter directly, and have ONR make the request for the V-22 model on CDI's behalf.

Disturbance Field Characterization

Flow Characteristics

Properties of flow over two-dimensional obstacles are described first, followed by a description of characteristics over 3D obstacles. For 3D geometries, the direction of the incoming wind plays an important role on flow characteristics [9-11], and this influence will be discussed. In the context of DI environments, flat-topped ships have unique wake structures, and receive special attention in this document. The influence of ship motion on airwake features will be discussed as well.

Backward-Facing Step (2D)

Figure 2 illustrates the general flow features associated with a backward-facing step [12], where an unstable shear layer is formed when the upstream boundary layer separates at the sharp corner [13, 14]. This shear layer consists of concentrated vorticities with fluctuating velocity gradients that become increasingly more turbulent as the shear layer propagates downstream with increasing curvature towards the reattachment zone, where part of it is deflected upstream towards the recirculation zone (where the pressure is lower), and part of it is entrained downstream up to as much as 50 step heights [13].

In the recirculation zone, a primary larger "bubble" can be identified, where flow velocities directed upstream can reach up to 20% of freestream velocities, and where negative skin-friction coefficients have been measured in tests [13]. A secondary smaller recirculation zone can also result when 3D effects due to the presence of side walls are accounted for – see discussion below and in [15, 16].

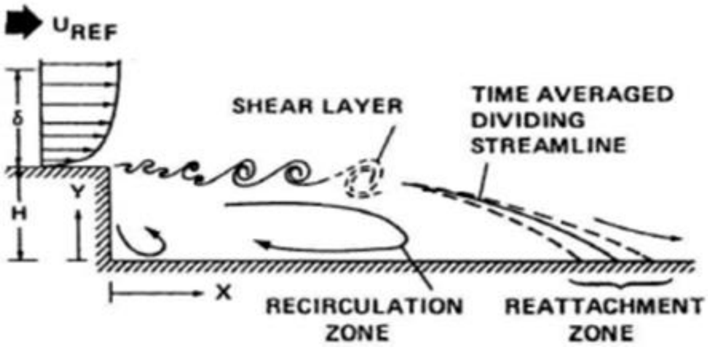

Figure 2: Flow topology over backward-facing step [4].

Flow in the reattachment zone is highly unsteady with coherent structures with length scales at least as large as the step height passing through this region [13, 17]. Coherent structures are large scale vortex structures that conserve their spatial features for prolonged durations. The location where the shear layer impinges on the wall fluctuates, shifting the reattachment zone upstream and downstream at low frequency [13, 14, 18, 19], with the primary recirculation bubble shrinking and expanding accordingly. Driver et al [12] suggest that this "flapping" motion results when part of the shear layer having greater momentum entrains more of the flow downstream, resulting in less flow being diverted towards the recirculation region. This causes the recirculation region to shrink and increases the shear layer curvature, which, in turn, increases the adverse pressure gradient in the reattachment zone, forcing flow back into the recirculation region. The amplitude of this flapping motion is estimated to be approximately 20% of the shear layer width b, which is given by

$$b = \Delta U/(d\bar{u}/dy)_{max}, \tag{1}$$

where U is the mean velocity in the stream wise direction, $\bar{u}$ is the streamwise velocity fluctuation, and the y coordinate is as defined in Figure 2 [12]. Driver et al further note that this low frequency motion does not have a strong impact on flow turbulence [12]. It should be noted that there is no consensus on the origin of the flapping motion in literature, for example see [17].

The mean reattachment length x_R, which represents the point of zero skin friction, is generally used to characterize the reattachment zone and can vary from 4.9H to 8.2H, where H is the step height, depending on the following parameters:

a) Reynolds number of the initial boundary layer,
b) boundary layer thickness,
c) free stream turbulence, and
d) blockage effects (for wind tunnel tests) [13].

In general, x_R is sensitive to the boundary layer Reynolds number only in the laminar and transition regimes (see Figure 3), and the effect of boundary layer thickness δ is noted to be more pronounced when δ/H << 1 [13]. Eaton and Johnston [13] suggest that x_R decreases with high levels of freestream turbulence, and that its effect would likely be dependent on the spectrum of the turbulence.

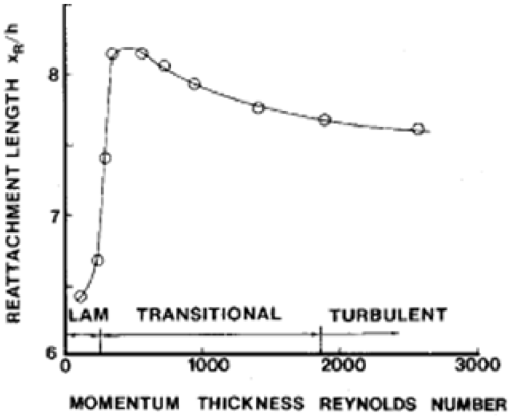

Figure 3: Influence of Reynolds number on reattachment length [13].

Eaton and Johnston [13] further show that maximum turbulence intensity I, defined as the ratio of root-mean-square of turbulent velocity fluctuations to mean absolute velocity

$$I = \frac{\bar{u}}{U_0}, \tag{2}$$

tends to be close to $I = 20\%$, and is typically observed approximately 1H upstream of the mean reattachment point. Beyond 1H, the maximum turbulence intensity decays rapidly.

Vortex shedding is characterized by the Strouhal number which is defined as

$$St = \frac{fb}{U}, \tag{3}$$

where f is the vortex shedding frequency and b is the characteristic length. Through spectral analysis of the pressure fluctuations at two streamwise locations $x/H = 5.5$ and $x/H = 8.0$, Driver et al. [12] identify a dominant frequency of $St = 0.2$, which is comparable to the characteristic frequency noted in the spanwise vortical structures of free shear layers, and is consistent with shedding from a flat plate aligned perpendicular to the flow [20].

Rectangular Prism (2D)

In 2D flow over a rectangular prism, free shear layers are shed from the sharp edges of the cross-section as depicted in Figure 4 [21], where streamlines over four rectangular prisms with different width-to-length aspect ratios are shown. It is evident that aspect ratio influences the mean reattachment length, and for aspect ratios 1:3 and 1:4, the mean flow reattaches to the lateral sides of the rectangle. The resulting mean (time averaged) flow features are also symmetric. The Strouhal number for vortices shed by rectangular prisms can vary from 0.1 to 0.18 depending on the aspect ratio and Reynolds number [22].

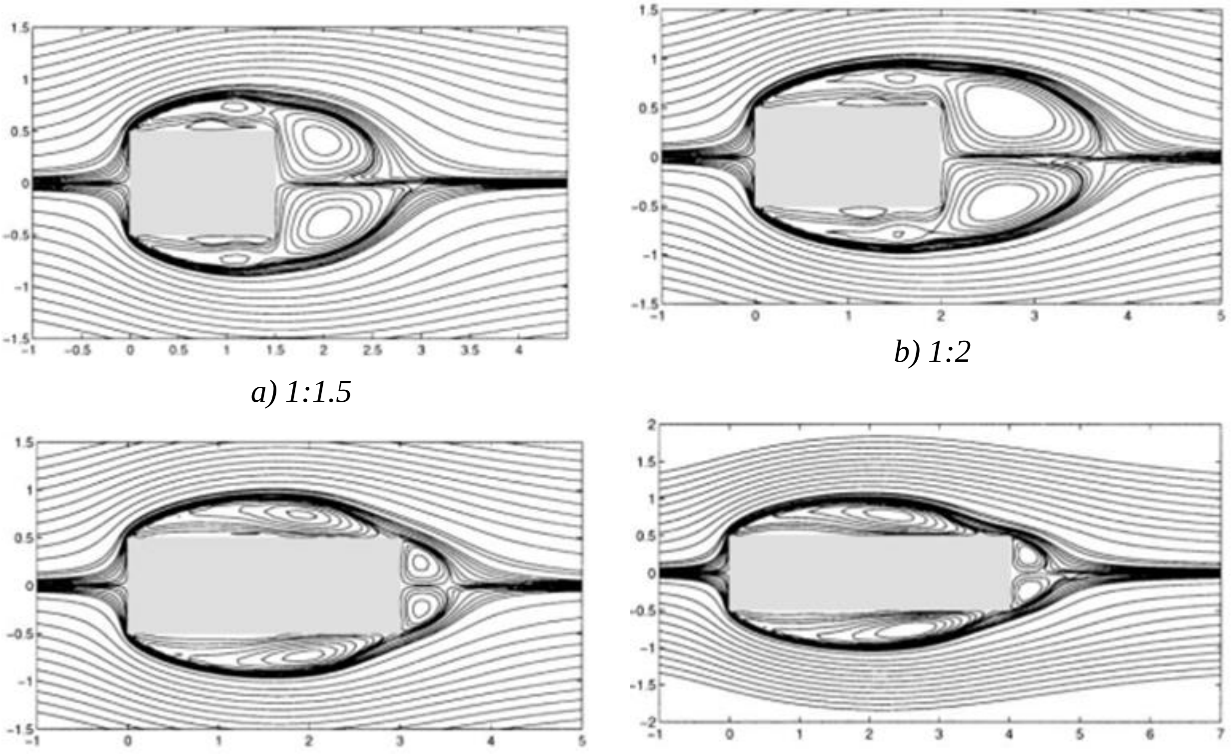

a) 1:1.5

b) 1:2

c) 1:3

d) 1:4

Figure 4: Streamline of mean flow around rectangular prisms with different aspect ratios [21].

Surface-Mounted Cuboid (3D)

Flow over 3D obstacles, such cuboids, introduce additional complexity relative to the 2D case as end and side wall effects become important [23, 24]. Flow features around a surface-mounted cuboid are depicted in Figure 5 and Figure 6 [23]. Upstream of the obstacle, horseshoe vortices form that extend over the sides of the obstacle and interact with the downstream separation region, resulting in high flow unsteadiness [25]. An arch vortex forms on the leeward side of the obstacle, and flow detaches at the top edge of the wind-facing surface of the obstacle and reattaches downstream of the arch vortex. The mean reattachment length in 3D is shorter than that noted for 2D backward facing step due to side wall effects. Note from Figure 5 that time-averaged flow features are symmetric.

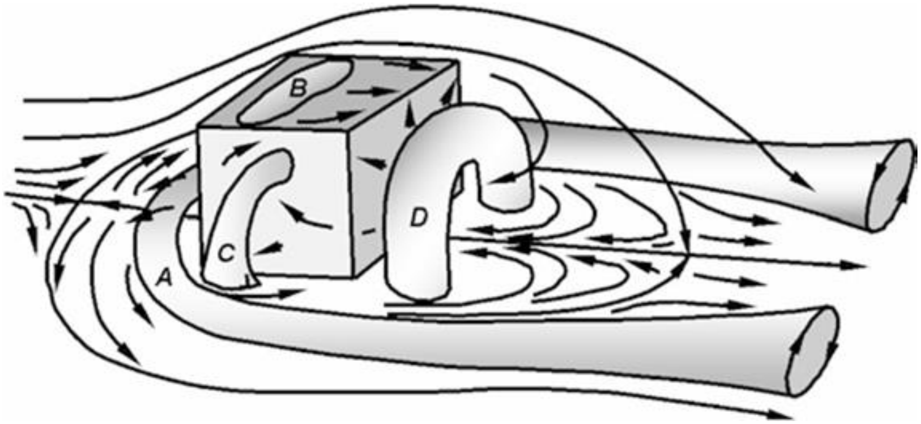

Figure 5: Schematic of principal flow features around surface-mounted obstacle [23].

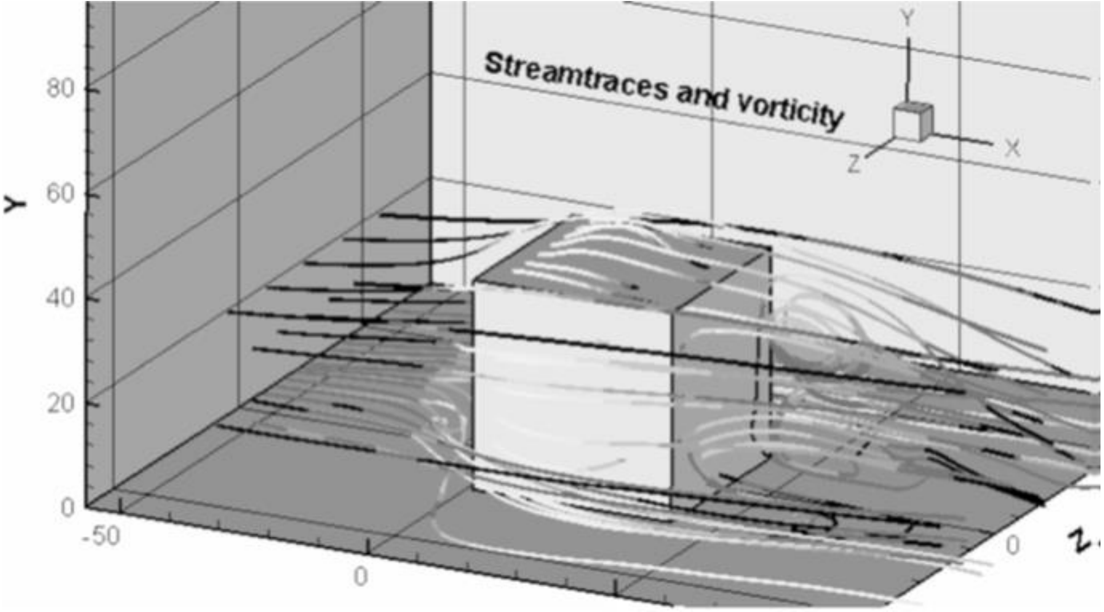

Figure 6: Perspective view of streaklines around surface-mounted obstacle [23].

Similar flow features are noted with 3D rectangular prisms [26], though they are sensitive to aspect ratio [27]. If the height is less than the length and width, the flow reattaches on the top surface of the prism, and up to three recirculation regions are observed, as shown in Figure 7 [26]. The location of the reattachment point on the top surface and behind the prism varies in the spanwise direction as depicted in Figure 8 [26]. Herry [27] notes that the location of the reattachment point is sensitive to the obstacle length-to-height aspect ratio, width-to-height aspect ratio, and Reynolds number. There is a minimum Reynolds number Re_c above which flow features become independent of Reynolds number for bluff bodies with sharp edges [10, 28, 29], however, a general rule for obtaining Re_c based on geometrical properties does not seem to have been established [28]. Not surprisingly, however, the mean velocity and turbulence of any upstream atmospheric boundary layer also influences downstream flow turbulence levels [10, 29, 30].

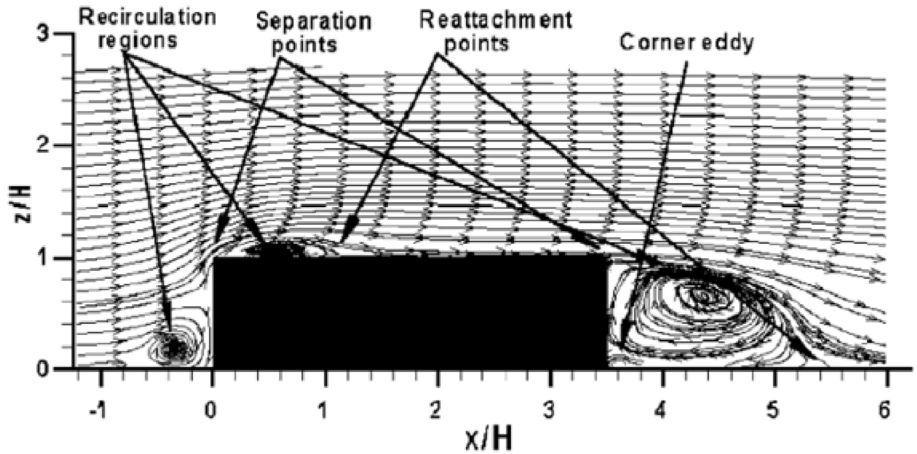

Figure 7: PIV derived streamlines at center plane around surface-mounted obstacle [26].

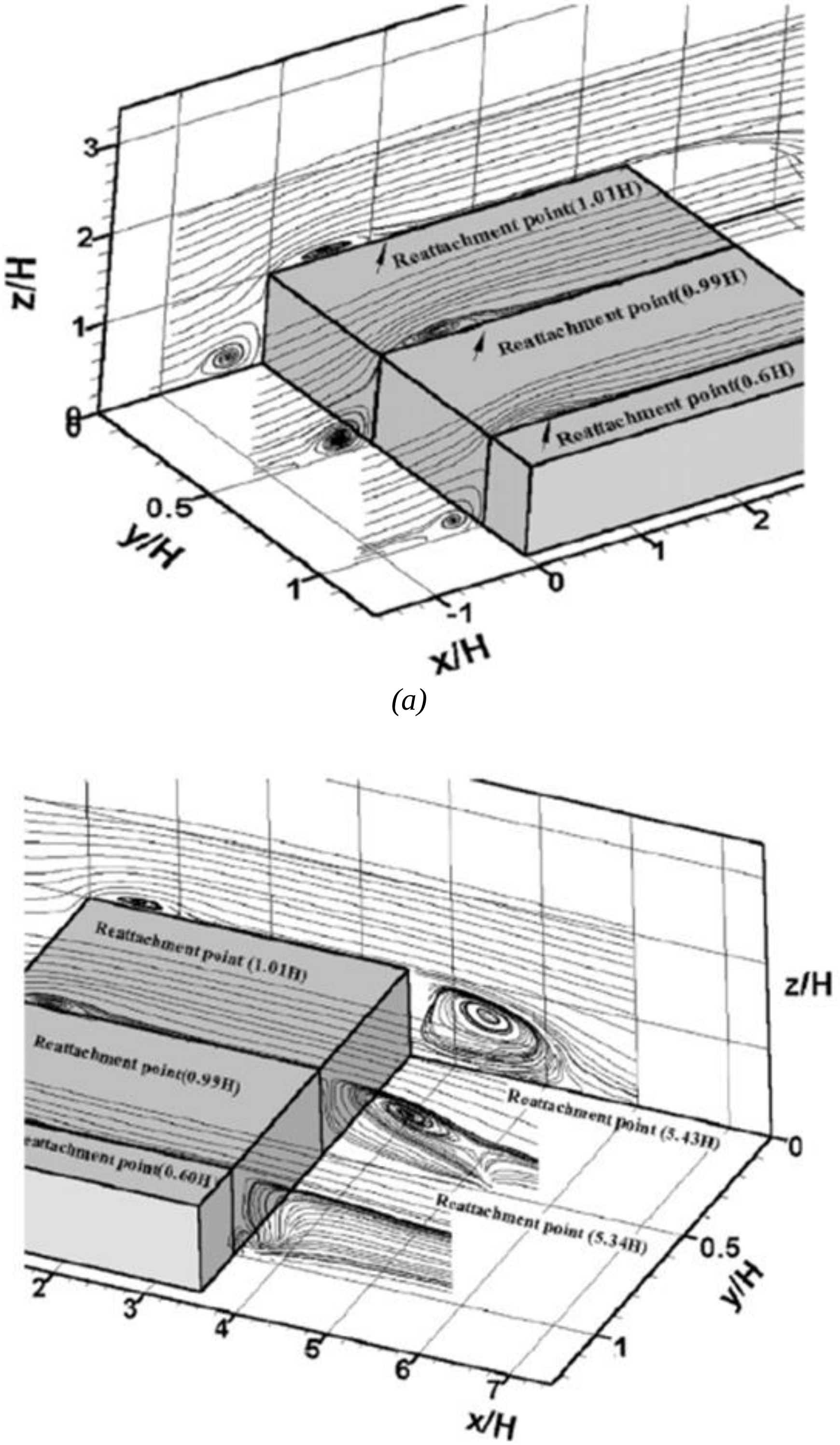

(a)

(b)

Figure 8: Streamlines of flow over surface mounted obstacle seen from (a) windward and (b) leeward directions [26].

An important parameter used to quantify flow turbulence is the turbulent kinetic energy (TKE) defined as [26]

$$TKE = \frac{1}{2}\left(\overline{u^2} + \overline{v^2} + \overline{w^2}\right), \tag{4}$$

where, $\bar{u}, \bar{v}, \bar{w}$ represent fluctuating streamwise, spanwise and vertical velocity components. TKE can be related to turbulence intensity, introduced previously, as:

$$I = \sqrt{\frac{2}{3}TKE} \tag{5}$$

Kim et al. [26] observed peak TKE levels on the top surface of a 3.5H long rectangular prism at $x \approx 0.5H$, see Figure 9. Becker et al. [10], on the other hand, examined flow over a rectangular prism with a shorter length of 0.25H and observe peak turbulence levels at $x = 3H$, as depicted in Figure 10, demonstrating the influence of aspect ratio on flow characteristics. Their spectral analysis further indicates dominant frequencies at $St_H = 0.15$, with little sensitivity to Reynolds number and the width-to-height aspect ratios (1:2, 1:3, 1:4 were considered) [10]. Note that this Strouhal number is higher than $St_H = 0.104$ noted for flow over cubes [25]. The subscript "H" indicates that the obstacle height was used as characteristic length in computing the Strouhal number, see Eq. (3).

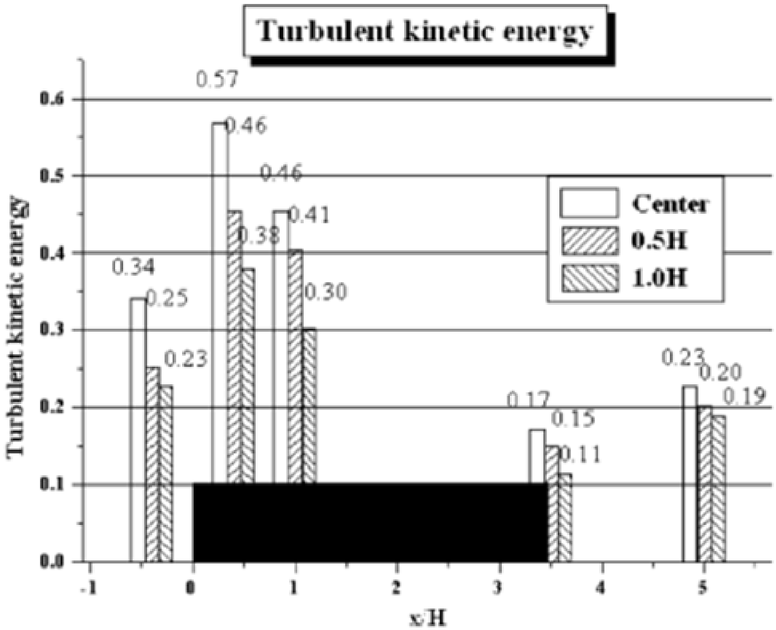

Figure 9: Turbulent kinetic energy peaks at different locations for flow over a 3D rectangular prism from Ref. [26] (boundary layer thickness of $\delta = 0.06H$ and Reynolds number (based on step height) of 7.9×10^3)

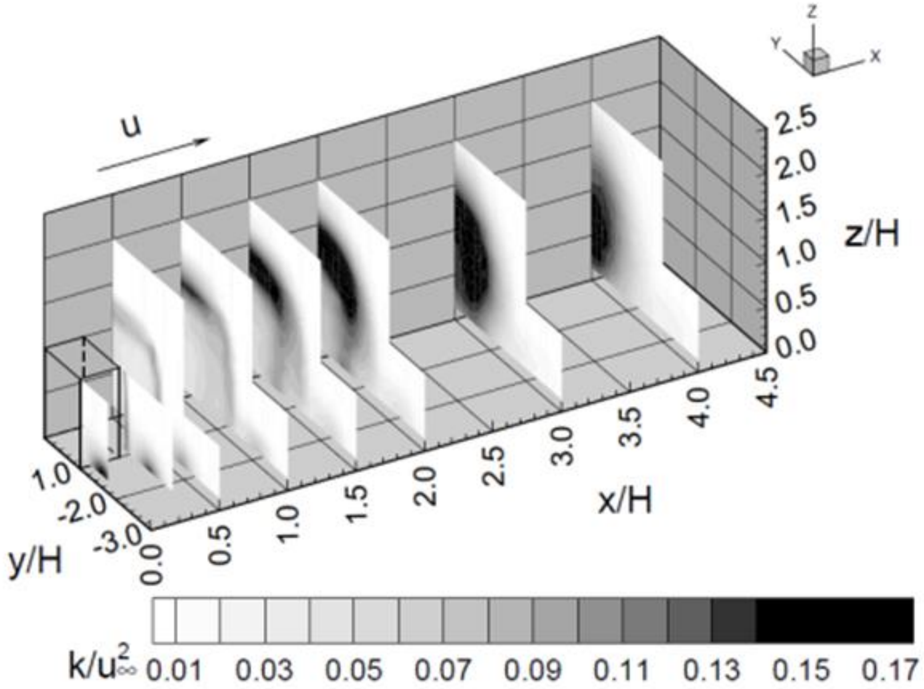

Figure 10: Turbulent kinetic energy at different locations for flow over a 3D rectangular prism from Ref. [10].

<u>Small-Deck Ships (3D)</u>

The double-backward facing step geometry, depicted in Figure 11 along with prevalent flow features [31], closely matches the aft region of typical small-deck aviation ship geometries and is thus of particular interest. Tinney and Ukeiley [31] derived the flow features in the figure using both PIV and oil-flow visualizations at $Re = 9000$ for the ship geometry shown in Figure 12. The flow features in Figure 11 are similar to those for flow over a surface mounted cube shown in Figure 5, with some notable differences. In the flow aligned case, the upstream horseshoe vortex seen in Figure 5 is no longer present in Figure 11 due to flow reattaching on the walls of the structure before the first step. Streak lines that start along the edges of the ship structure from the nose curl up into vortex tubes, denoted as “wing vortex” in Figure 11, due to pressure gradients between the side and top surfaces of the structure and interact with flow downstream of the reattachment region to produce counter-rotating vortex tubes on both sides of the streamsurface bifurcation point on the figure.

Although Figure 11 depicts a symmetric upside-down arch vortex aft of the first step, this structure is unsteady and at any instant in time is asymmetric, see Figure 13 from [27]. This is a consequence of bi-stability of the flow, which causes the resulting asymmetric flow features to switch intermittently between portside and starboard locations. The influence of this asymmetry on helicopter-shipboard operations remains to be examined.

Tinney and Ukeiley [31] observe peak longitudinal turbulence intensity near the recirculation zone at $1H \leq x \leq 2H$ downstream of the first step (see Figure 14a) and peak vertical turbulence intensity closer to the reattachment zone in the $2H \leq x < 4H$ region (see Figure 14b). Turbulent kinetic energy is dominated by longitudinal velocity fluctuations, and peak TKE is observed in $1H \leq x < 2.5H$ region in Figure 14d. Note that the TKE was computed using only longitudinal

$\bar{u}$ and vertical $\bar{v}$ components. The longitudinal and vertical turbulent intensities in the figure are noted to be greater than those observed with 2D obstacles [31]. The dominant frequency was characterized by a Strouhal number of $St_H = 0.17$ [31].

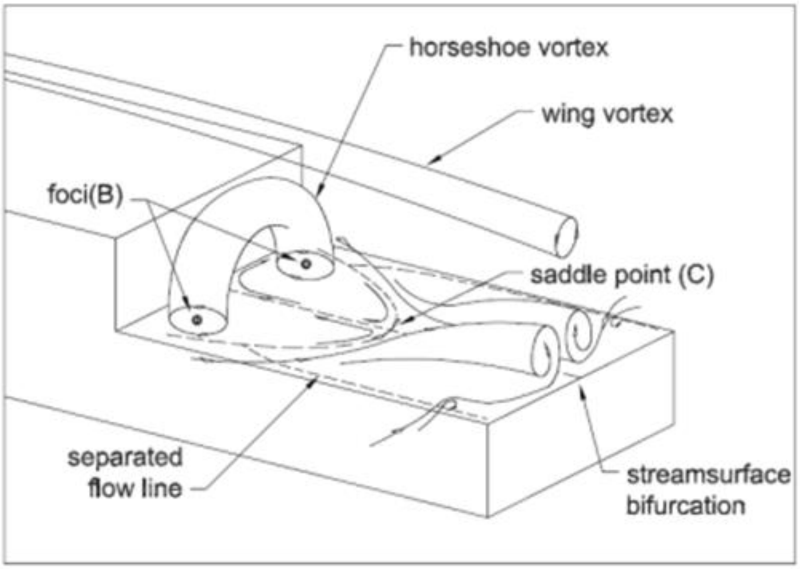

Figure 11: Flow feature for a 3D double-backward facing step [31].

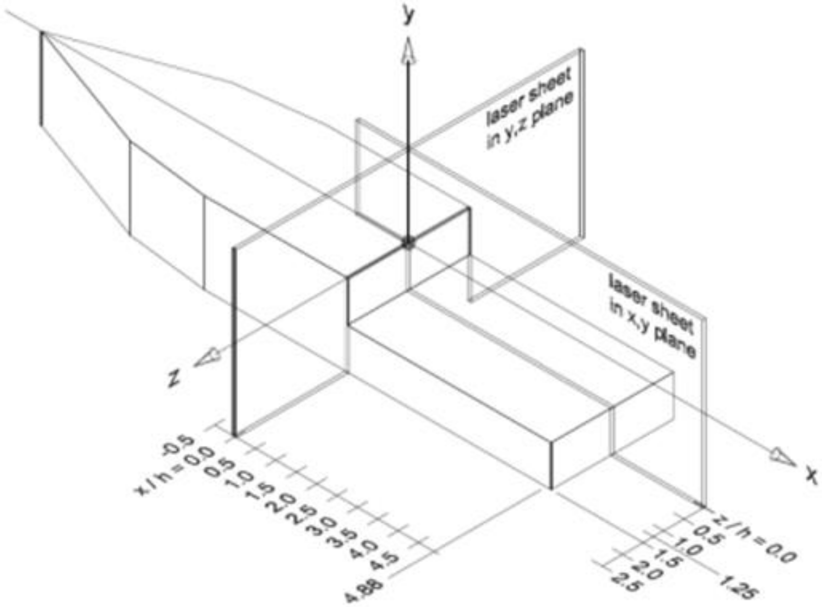

Figure 12: Ship geometry used to derive flow features for a 3D double-backward facing step [31].

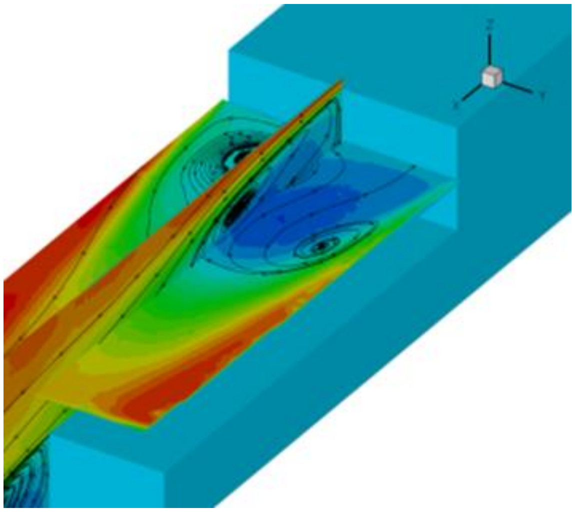

Figure 13: Asymmetry in arch vortex behind 3D double-backward facing step [27].

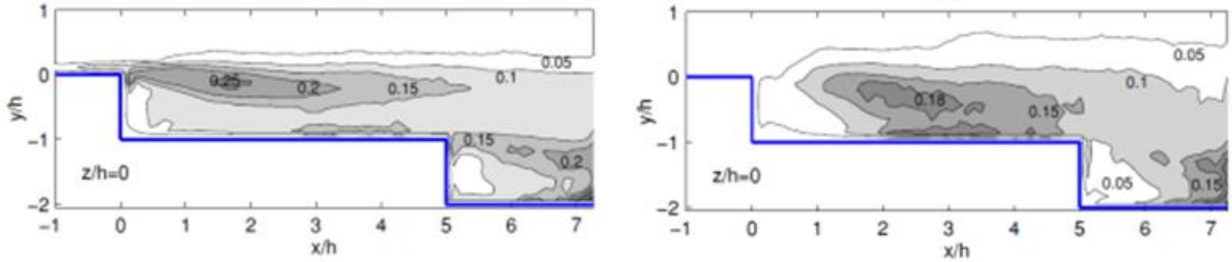

(a) $\langle \overline{\boldsymbol{u}}\overline{\boldsymbol{u}} \rangle^{\mathbf{0.5}}/\boldsymbol{U}$ (b) $\langle \overline{\boldsymbol{v}}\overline{\boldsymbol{v}} \rangle^{\mathbf{0.5}}/\boldsymbol{U}$

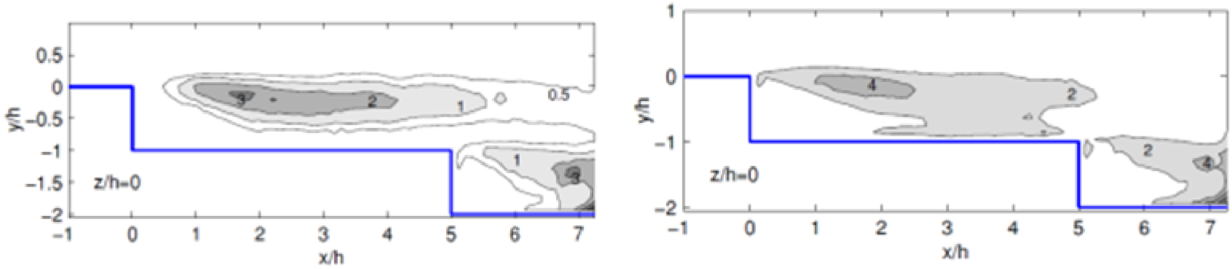

(c) $-\langle \overline{\boldsymbol{u}}\overline{\boldsymbol{v}} \rangle^{\mathbf{0.5}}/\boldsymbol{U}^{\mathbf{2}} \times \mathbf{10}^{\mathbf{2}}$ (d) $\boldsymbol{TKE}/\boldsymbol{U}^{\mathbf{2}} \times \mathbf{10}^{\mathbf{2}}$

Figure 14: Contours of turbulence parameters for a 3D double-backward facing step [31].

Flat-Topped Ships (3D) and Wind-Over-Deck

Flat-topped ships, such as aircraft carriers and Landing Helicopter Assault (LHA) ships (e.g. Figure 15), are characterized by sharp-edged flat decks and superstructures located towards the starboard side of the ship. While helicopter landing spots are distributed across the entire deck, the fixed wing landing zone typically takes up most of the port side of the deck.

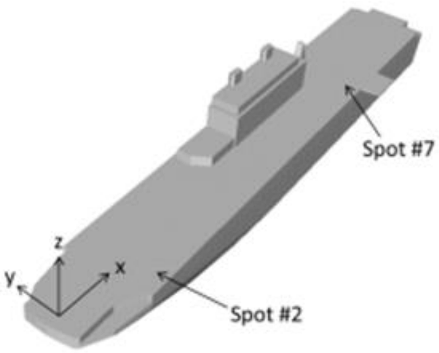

Figure 15: LHA ship geometry with landing spots #2 and #7 highlighted, adapted from Fig. 1b in Ref. [32].

A unique aspect of the flow characteristics around such configurations is the existence of "wing-vortex" like structures that originate and propagate from the edges of the ship structure, denoted as "deck-edge vortices" in Figure 16 [32]. From Figure 16a, headwinds produce a large separation at the bow, though strong coherent wind aligned deck-edge vortices also form. These vortices are generated due to pressure differences between the side and top surfaces of the deck. Vortical structures denoted as "burbles" in Figure 16a shed periodically from the bow towards the superstructure at frequencies of 0.2 – 0.3 Hz [32]. The interaction between the superstructure, burbles, freestream, and deck-edge vortices produces the highly turbulent region over and aft of the superstructure.

The airwake in the lee side of ship is highly unsteady and separated, producing downwash fields that can cause fixed-wing aircraft to bolter during landing, resulting in a touch-and-go maneuver on the deck and requiring an additional landing attempt. This region of high turbulence is known as the "burble," (not to be confused with the burble structures shed from the bow) and the associated loss of altitude and deviation from desired glideslope experienced by pilots during landing is known as the "burble effect" [33]. The ambient wind interacting with the ship structure, combined with the ship velocity, is referred to as "wind-over-deck" (WOD). For a starboard WOD condition at 30° (measured clockwise relative to the ship longitudinal axis), no bow separation or burble structure is present in Figure 16b. The starboard deck-edge vortex rolls unto the deck and spreads spanwise over the deck while the portside one detaches from the ship and is blown over the ocean, with significant flow separation over the superstructure.

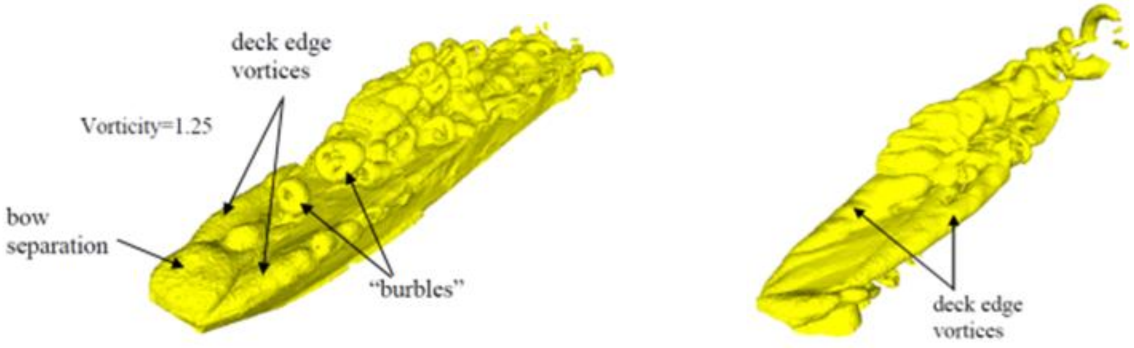

(a) 0° *(b) 30°*

Figure 16: Snapshot of vorticity iso surfaces for a 30 kts WOD from Ref. [32]

Figure 17 shows instantaneous iso-surfaces for the headwind and 30° starboard WOD conditions from Ref. [34], where both time-accurate and time-averaged flow conditions over a full-scale LHA ship geometry were examined using the PUMA2 solver. In Figure 17b, a vortical coherent structure from the starboard edge that runs diagonally across the fore of the ship is evident for the 30° WOD condition. This vortical structure results in lateral velocities of approximately -11 m/s over spot #2 (see Figure 18a [34]), which is 40% greater than the freestream value of -7.7 m/s ($-15.43 \sin 30^\circ$ m/s). The largest velocity fluctuations were noted in the time-histories ~6 m above spot #7 for the 30° starboard WOD condition, see Figure 18b [34]. From spectral analysis of longitudinal and vertical velocity time-histories, Sezel-Uzol et al. note peak frequencies at 0.1 Hz ($St = 1.3$) and 0.2 Hz ($St = 2.6$) over spot #2, and a peak frequency of 0.5 Hz ($St = 6.5$) over spot #7 for both headwind and starboard 30° conditions. Note that Strouhal numbers were not computed in Ref. [34] and are provided here using the full-scale beam width of 31.8 m as characteristic length and the free stream velocity magnitude of 15.43 m/s.

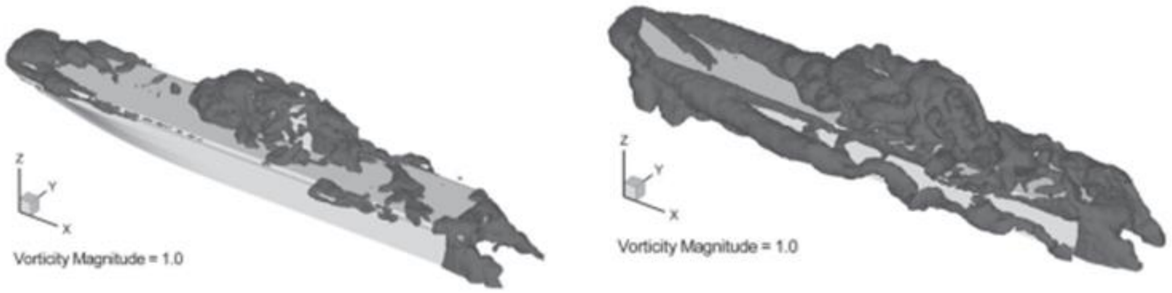

(a) 0° *(b) 30°*

Figure 17: Snapshot of vorticity iso surfaces for a 30 kts WOD from Ref. [34]

The influence of WOD angle on longitudinal u and vertical w velocity airwake components are shown on the time-averaged flow contour plots for a plane 6 m above the deck in Figure 19 and Figure 20, respectively [34]. From the figures, oblique and beam WOD conditions produce the greatest fluctuations in velocity components. For beam winds, regions with negative longitudinal velocities are noted in the fore of the ship in Figure 19. The sharp edges of the deck and the superstructure generate regions with reduced u velocity magnitudes in the oblique conditions. The contours in Figure 20 reveal regions with significant negative vertical velocities (up to -6 m/s) in the fore of the ship, which may adversely influence rotor inflow during piloted operations. These contours also indicate large upwash velocities of approximately 15 m/s on the windward edges of the ship, as flow rolls over the edges. It should be noted that the study by Sezer-Uzol et al. [34] did not account for atmospheric boundary layer (ABL), which is needed for better predictions of turbulence intensities at full-scale [35], however, it is not anticipated that including the ABL would fundamentally alter the primary flow structures in the wake. Rather, the ABL would serve to introduce additional frequency components, and likely accelerate the breakdown of bluff structures. In an accompanying paper [36], instantaneous vorticity magnitude plots for the PUMA2 based simulation of flow of the LHA ship were provided (see Figure 21). The deck-edge vortices are noted to have magnitudes in the 0.7 - 2.0 sec^{-1} range for the headwind condition and peak magnitudes of 3.0 sec^{-1} in the starboard 30° WOD case.

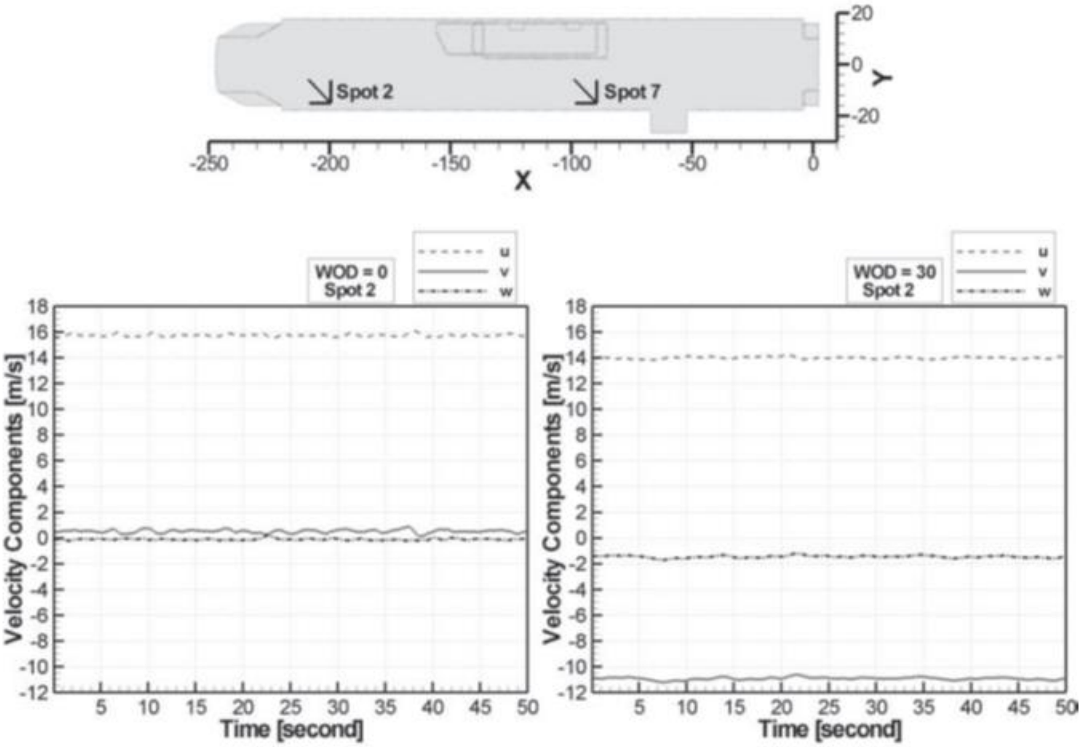

(a) Spot #2

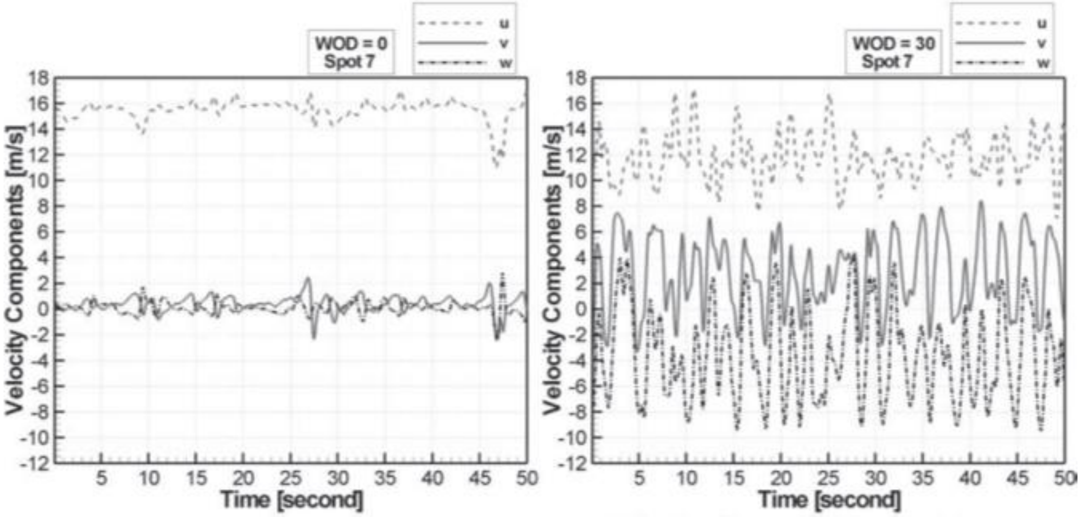

(b) Spot #7

Figure 18: Time histories of velocity components for 30 kts WOD 6m above landings spots #2 and #7 [34]

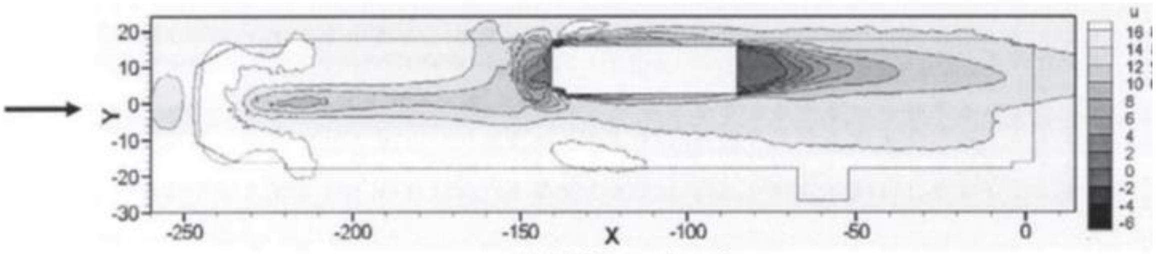

(a) WOD angle = 0

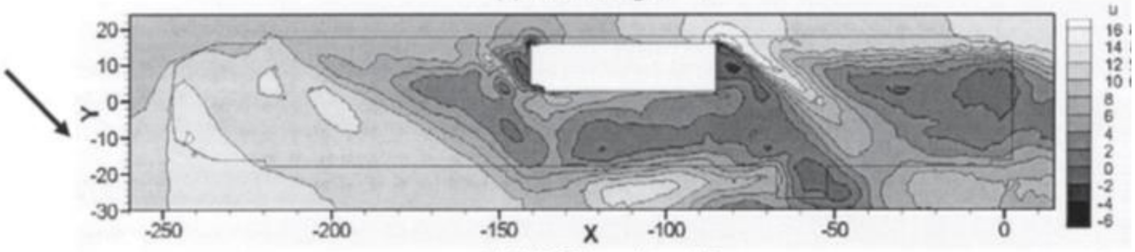

(b) WOD angle = 45

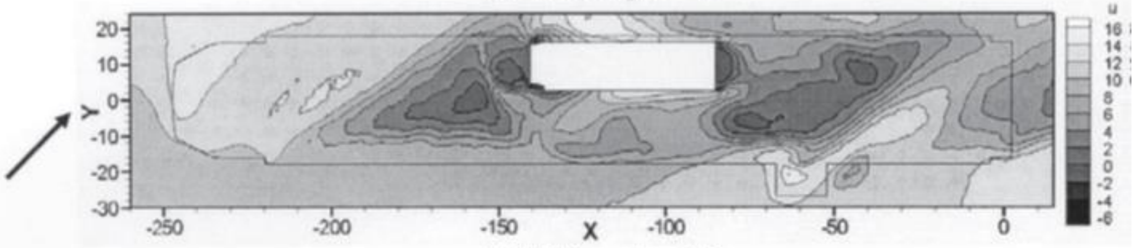

(c) WOD angle = 315

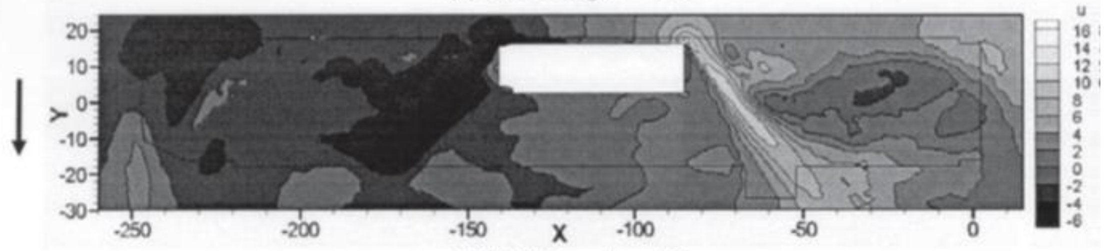

(d) WOD angle = 90

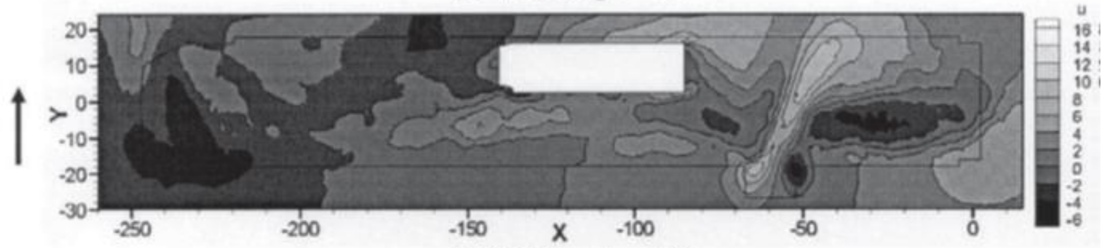

(e) WOD angle = 270

Figure 19: Time-averaged contours of longitudinal velocity for different WOD conditions [34]

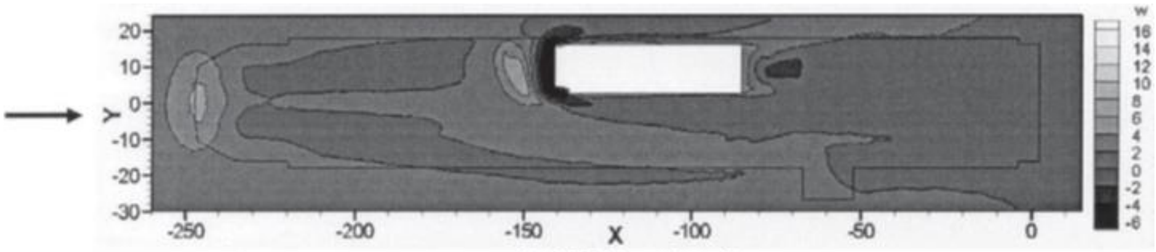

(a) WOD angle = 0

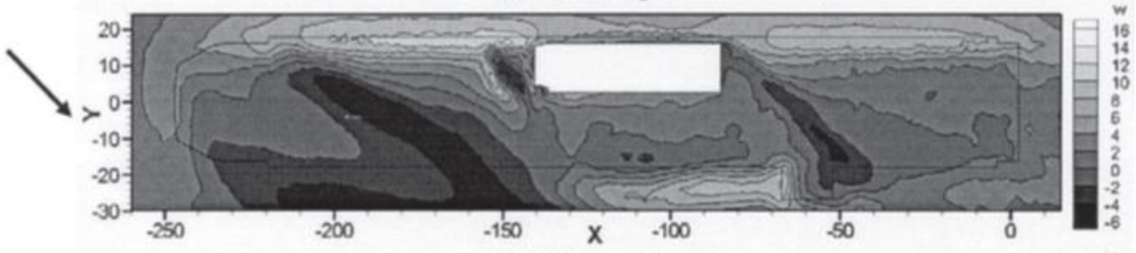

(b) WOD angle = 45

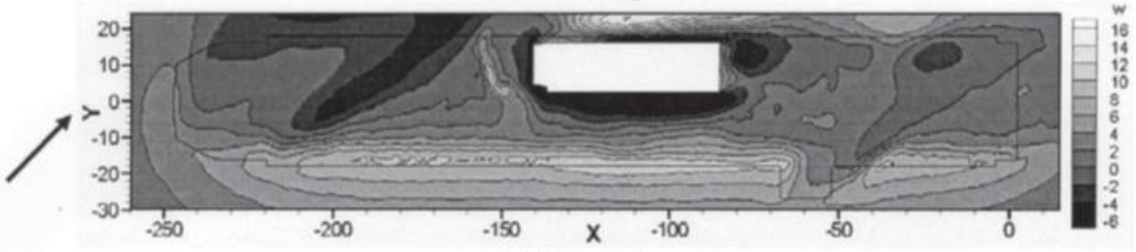

(c) WOD angle = 315

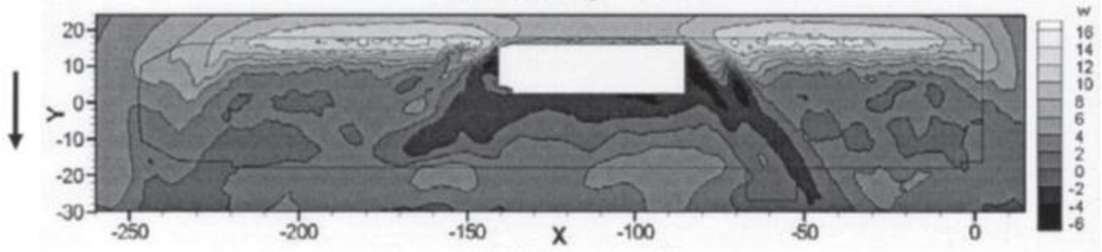

(d) WOD angle = 90

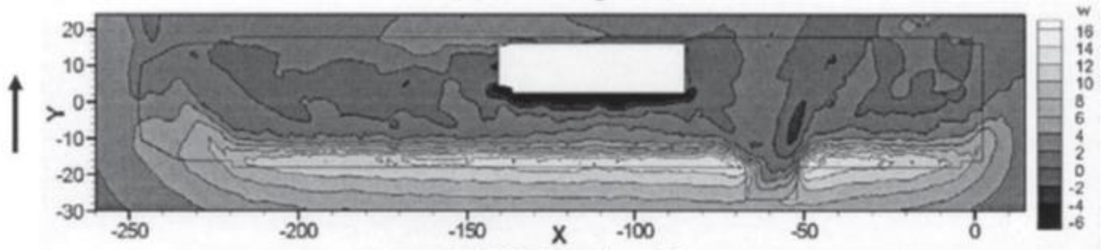

(e) WOD angle = 270

Figure 20: Time-averaged contours of vertical velocity for different WOD conditions [34]

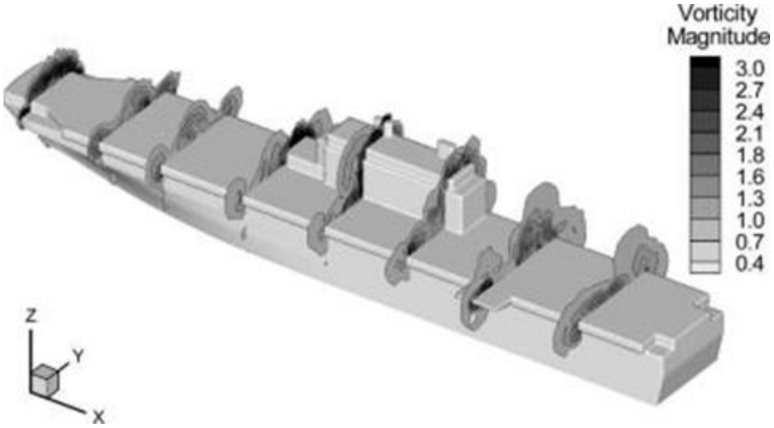

(a) 0° WOD

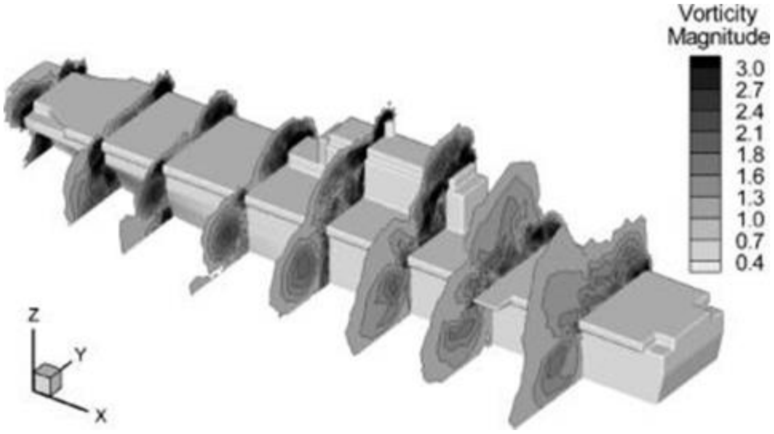

(b) 30° starboard WOD

Figure 21: Instantaneous vorticity contour magnitude across ship deck [36]

Although CFD predictions provide valuable insight into ship airwake characteristics, they can only be considered reliable when validated against experimental data (model or full-scale) since factors such as solution type (RANS, DES, LES), time step size and mesh resolution can influence predictions [37]. Wind tunnel experiments are easier to setup, control and interrogate than full-scale tests, which are sensitive to changes in at-sea conditions, but usually fail to replicate full-scale Reynolds number due to tunnel limitations. This has been generally considered acceptable since the wakes shed from the sharp edges of ship decks and superstructures tend to be Reynolds number independent [32]. Turbulence in the wake at wind-tunnel scale experiments also tend to occur at much higher frequencies than full-scale tests [32], but the cause of this is not entirely clear. Polsky and Bruner in Refs. [32] and [38] compare time-averaged and steady-state CFD solutions to wind tunnel data obtained using a 1/120th scale model of the LHA ship for a headwind condition. Only time-averaged measurements were made during the experiment. Velocities along the data plane shown in Figure 22 are shown in Figure 23 for $z = 0.2315$ in (equivalent to $z = 2.315$ ft. at full-scale) [38]. Time-averaged predictions from CFD were obtained from time-accurate simulations. Corresponding standard deviation bounds are also plotted in Figure 23 to highlight velocity fluctuations in the time-accurate solution.

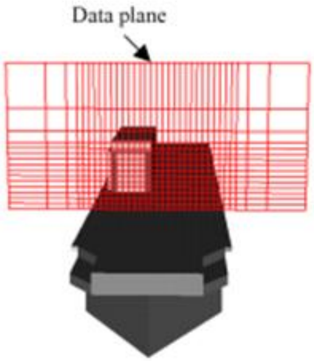

Figure 22: Plane considered for CFD comparison with experimental data in Ref. [32]

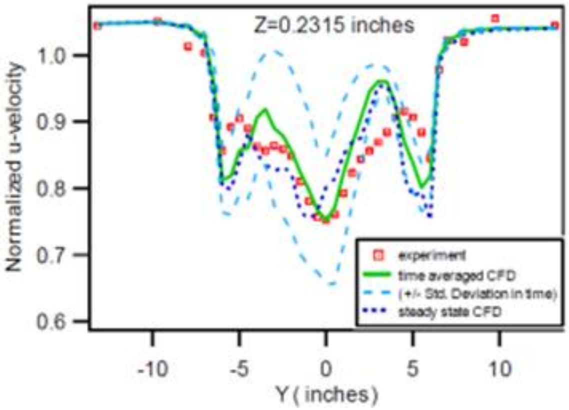

(a) u-velocity

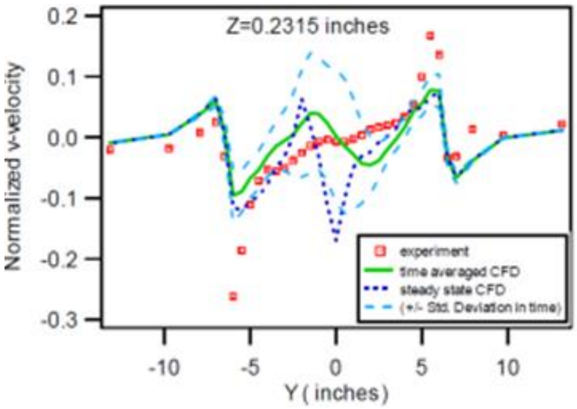

(b) v-velocity

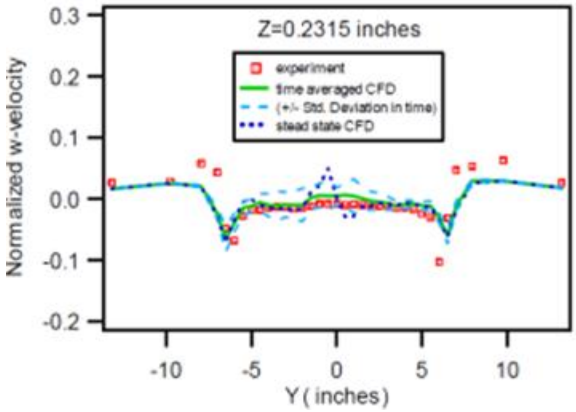

(c) w-velocity

Figure 23: Comparison of velocities from CFD with wind tunnel data, z=0.2315 in [38]

Discrepancies between CFD predictions (with standard deviation) and experiments are noted near the edges of the deck at $y = \pm 5$ inches in the lateral and vertical velocity components, potentially due to deck-edge vortex effects not being modeled properly in CFD. Time-averaged velocity predictions for $z = 0.7315$ in (equivalent to $z = 7.315$ ft. full-scale) are shown in Figure 24 [32]. Similar offsets are evident in the lateral and vertical velocity components near the edge locations at $y = \pm 5$ in.

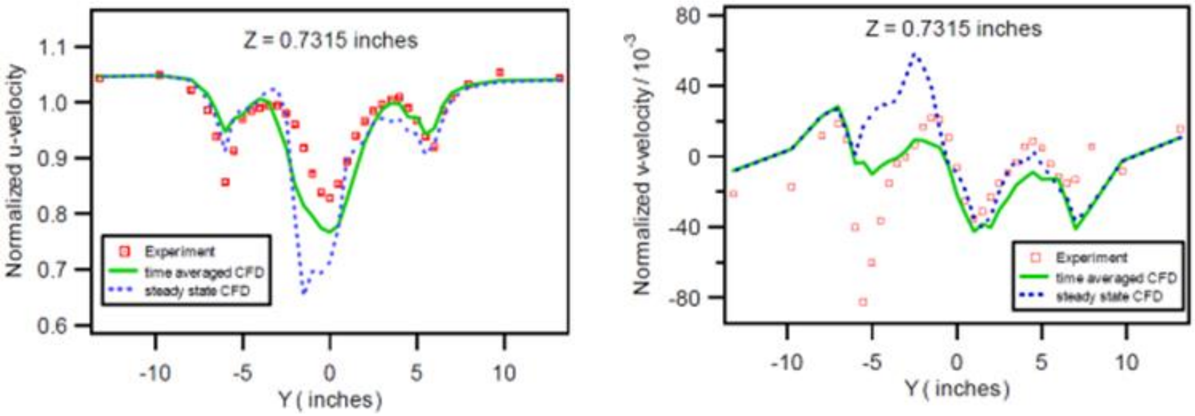

(a) u-velocity *(b) v-velocity*

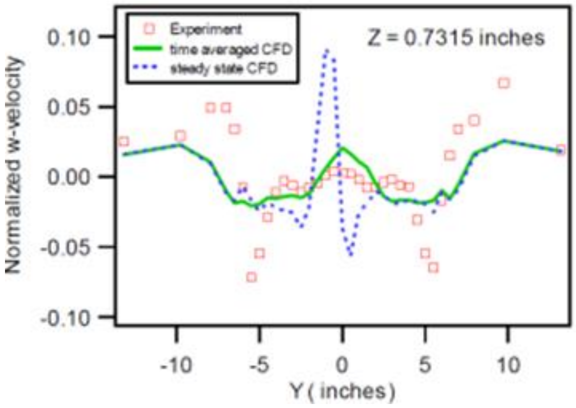

(c) w-velocity

Figure 24: Comparison of velocities from CFD with wind tunnel data, z=0.7315 in [32]

The discrepancy between CFD predictions and experimental data was also noted in a study by Rajagopalan et al. [39], where mean velocity predictions from the Rot3DC unsteady, incompressible flow solver were compared to PIV data obtained for a 1/48th scale model of the LHA ship for 0° and starboard 15° WOD conditions. This study was part of a comprehensive effort by NAVAIR to better understand ship-aircraft dynamic interface after an on-deck V-22 aircraft experienced an uncommanded roll due to the combined upstream airwake from the ship and a CH-46 aircraft. Figure 25 shows streamwise velocity contours across landing spots #2, #4, #7 and #8. The deck-edge vortices are evident at spots #2 and #4. The influence of the superstructure is shown as well, resulting in velocities with magnitudes of up to 20% of freestream near spot #7. Comparisons of predicted and measured mean vertical velocities at the four landing spots at $z = 5.206$ in (equivalent to $z = 20.83$ ft. at full-scale) are shown in Figure 26. Note that this height corresponds to the height of V-22 rotors when the wheels are on the deck. Figure 26 shows that CFD fails to capture the peaks at $y = \pm 0.6$ near the edges of the ship (spot #4), similar to Ref. [38], but this discrepancy does not seem to have been discussed in literature.

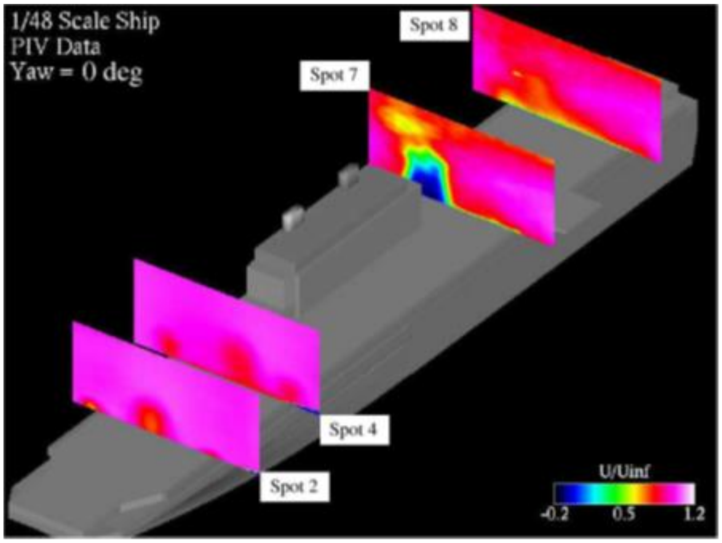

Figure 25: Streamwise velocity contour plots as determined from PIV data for headwind condition [39]

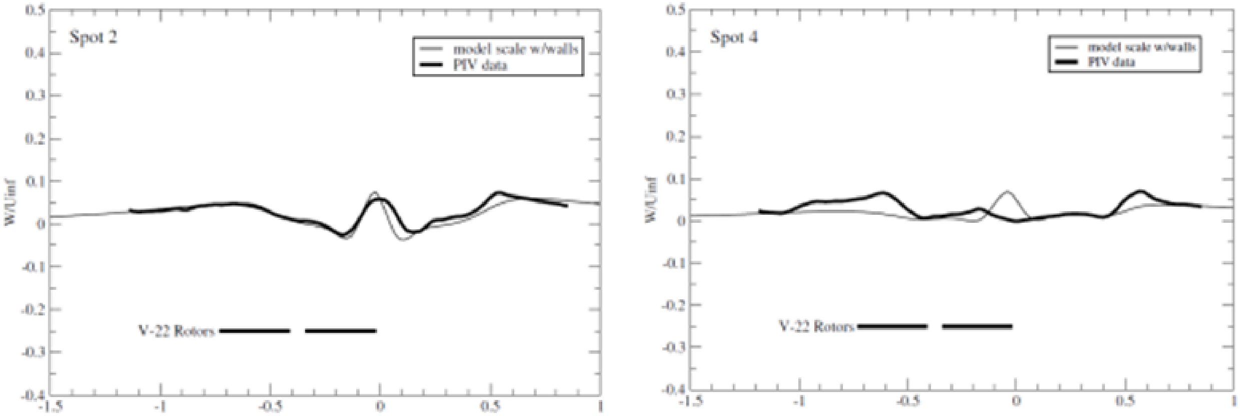

(a) Spot #2

(b) Spot #4

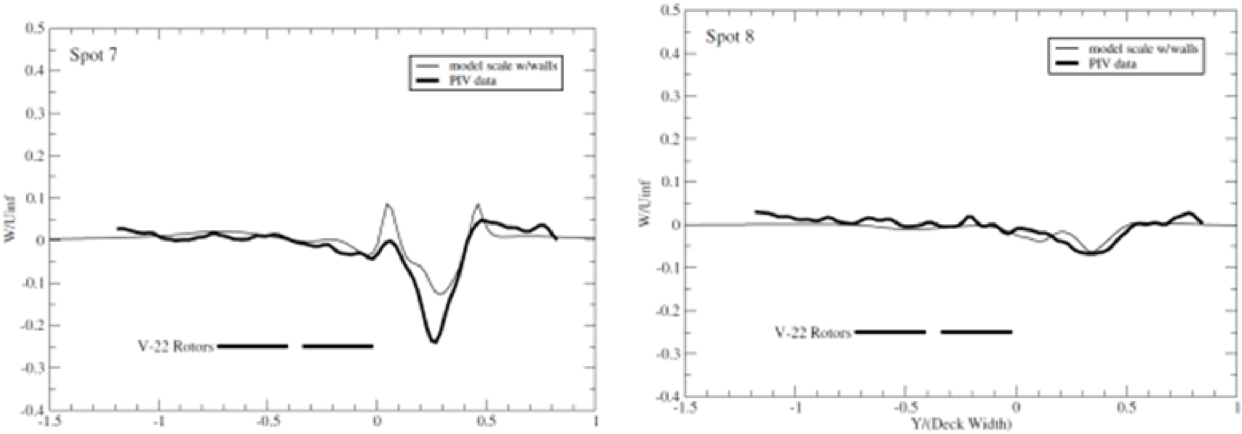

(c) Spot #7

(d) Spot #8

Figure 26: Mean vertical velocities at transverse planes across four landing spots for z=5.206 in [39]

In recent years, the need for a more systematic approach to studying airwake characteristics for flat-topped ships has been highlighted [40], and more recent studies have attempted to provide quantification metrics such as turbulence intensities [41-43] to enable direct comparison between tests and simulations.

An extensive CFD investigation of flow over a LHA ship was performed using OpenFOAM in Ref. [41], and qualitative agreement with results from [34] was noted. Mean velocity magnitudes across the ship beam at spots #2, #4, #7 and #8 are shown in Figure 27 for $z = 3$ m (9.8 ft.) and $z = 6$ m (19.7 ft.). The large drop in velocities at spots #2 and #4 are due to bow separation while those at spots #7 and #8 are due to the shedding downstream of the superstructure. It is interesting to note that the influence of deck-edge vortices is more pronounced closer to the deck at $z = 3$ m at spot #4. Corresponding turbulence intensity plots are shown in Figure 28, where bow separation produces the greatest turbulence at spots #2 and #4. Unfortunately, the definition of "turbulence intensity" is not specified by the author, and thus these figures should be viewed from a qualitative perspective. Streamwise turbulence intensity plots across the ship centerline and a line through the portside landing spots are shown in Figure 29 for two mesh resolutions. At the centerline, a peak in turbulence is noted due to bow separation and predictions from the two mesh resolutions show good agreement. Agreement in predictions deteriorates slightly on the portside line with differences of up to ~7% evident at $z = 3$ m.

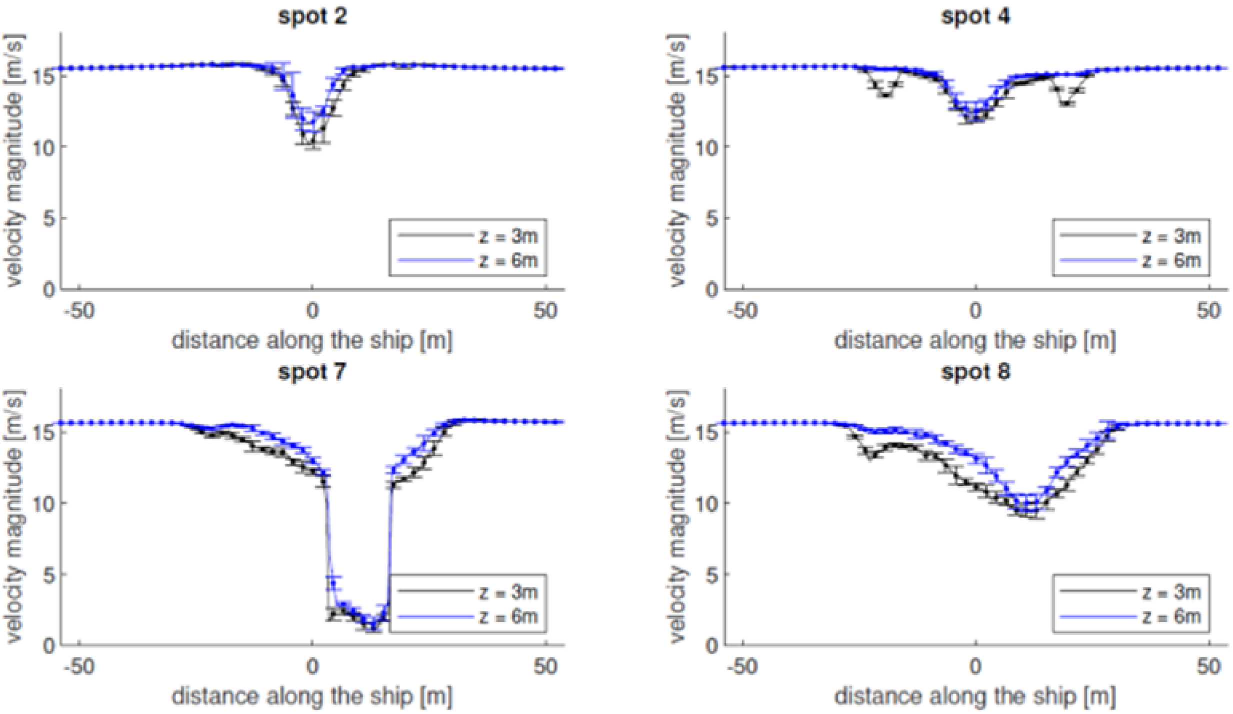

Figure 27: Mean velocity magnitude across landing spots of the LHA ship for a headwind condition [41]

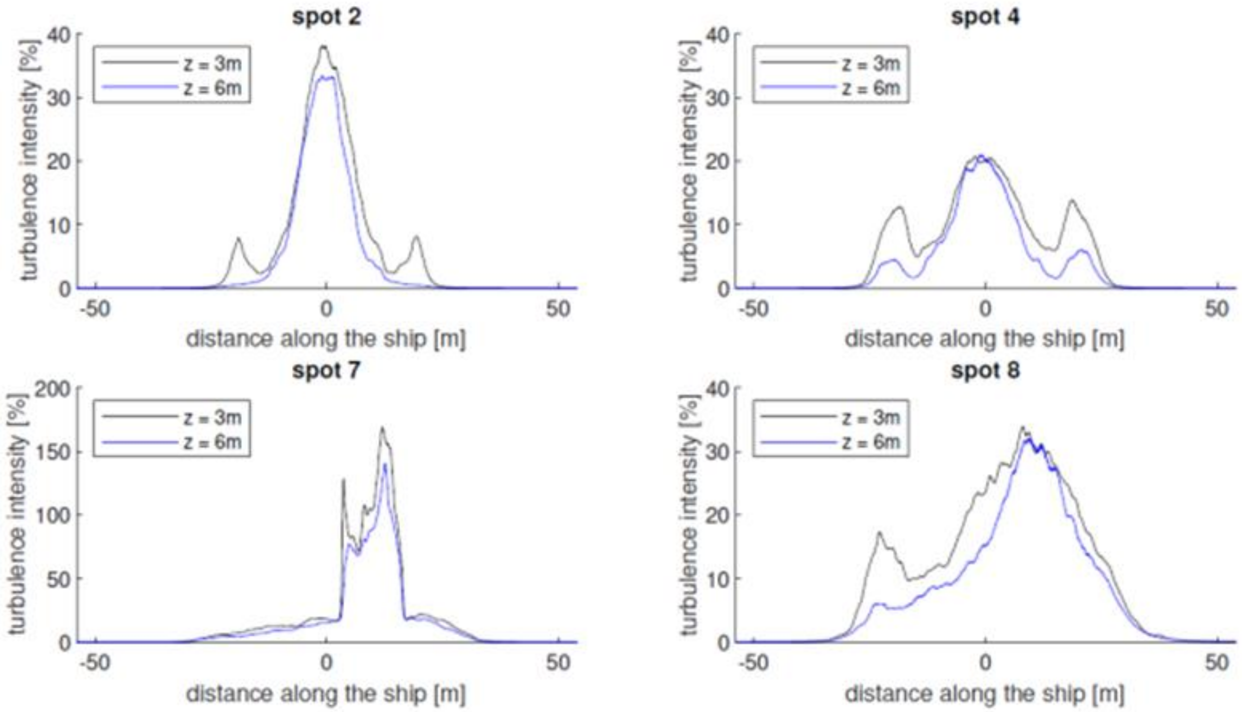

Figure 28: Turbulence intensities across landing spots of the LHA ship for a headwind condition [41]

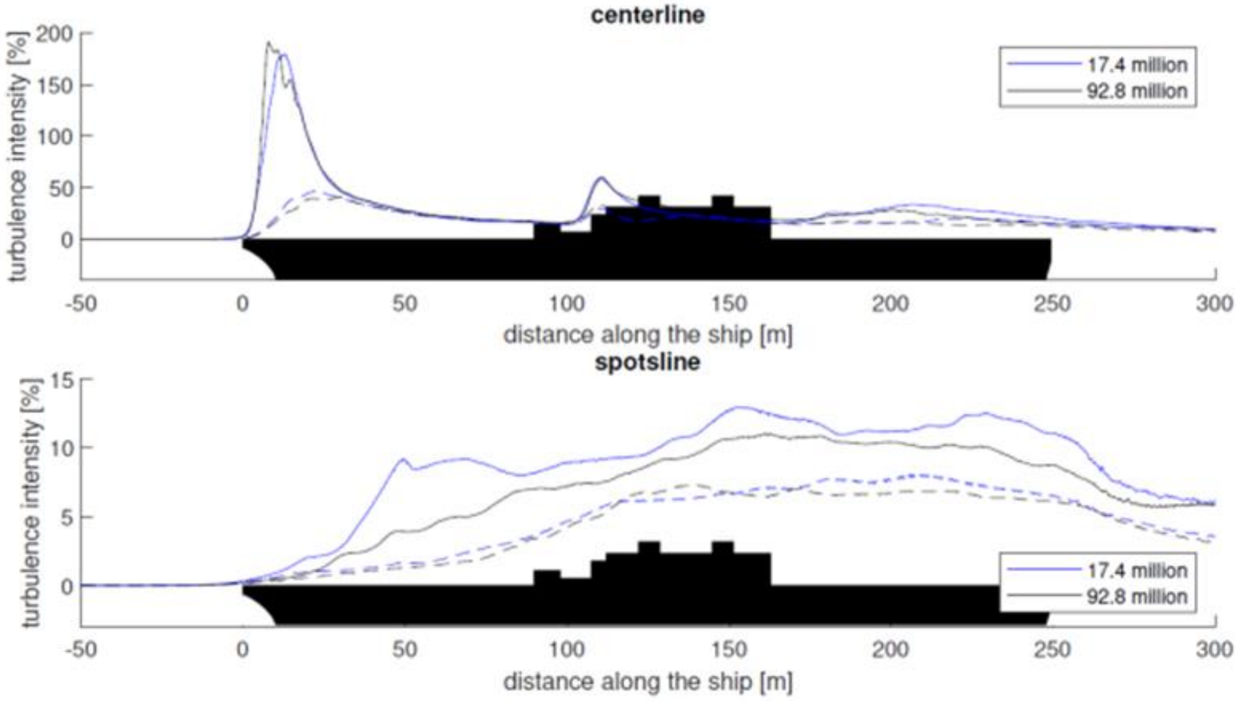

Figure 29: Turbulence intensities across LHA ship length for headwind condition; full line corresponds to $\boldsymbol{z} = \mathbf{3}$ *m and dashed line to* $\boldsymbol{z} = \mathbf{6}$ *m [41]*

The influence of WOD direction was assessed also in Ref. [41]. Figure 30 shows turbulence intensity plots for 6 WOD conditions over spots #2, #4, #7 and #8, where "green" winds denote winds from the starboard of the ship and "red" winds from the portside. As the wind conditions become more oblique, turbulence intensity over the landing spots increases significantly, with beam winds resulting in peak turbulence intensity values of ~1000%. For turbulence intensities across the ship length shown in Figure 31, the magnitudes of the turbulence intensities for 60° and 90° winds are similar, with the latter condition producing greater turbulence over the entire flight deck including the fore section. Note that no validation against experimental or full-scale test data was performed in this study [41].

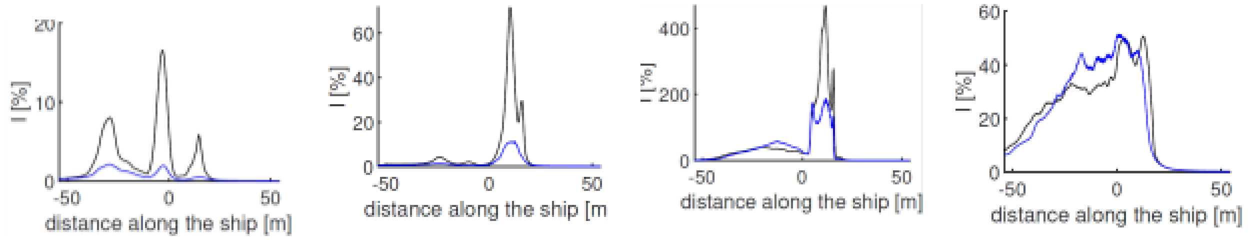

a) Green 30°

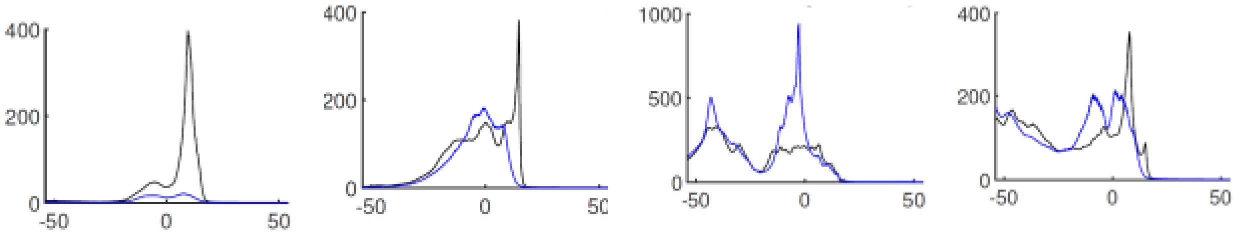

b) Green 60°

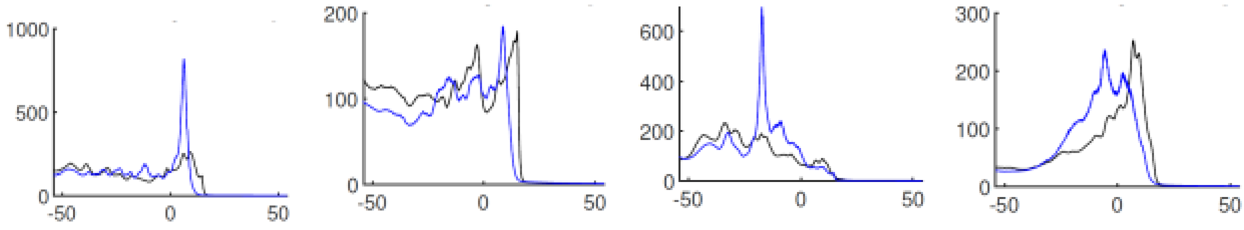

c) Green 90°

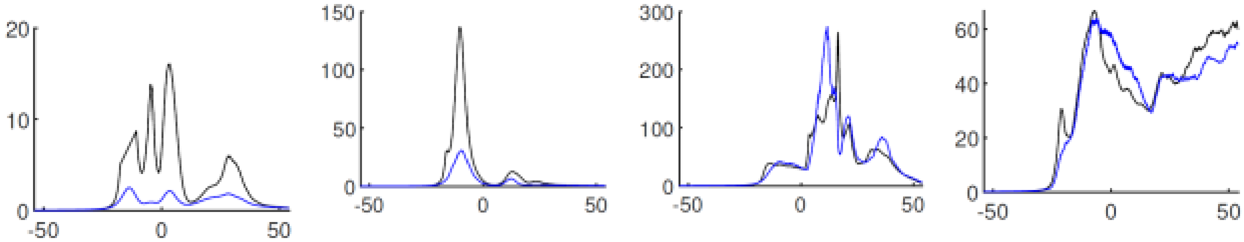

d) Red 30°

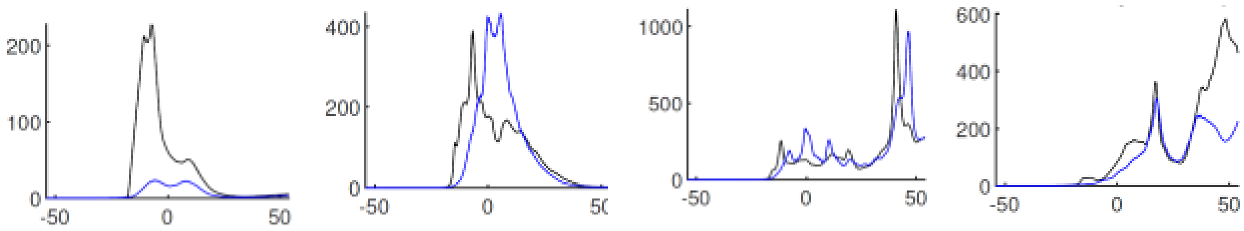

e) Red 60°

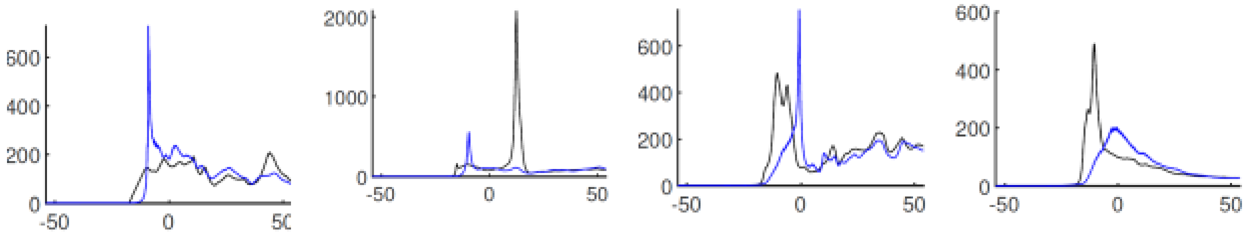

f) Red 90°

Figure 30: Turbulence intensities across landing spots #2, #4, #7 and #8 (in that order from the left) for various WOD directions; black line corresponds to $\mathbf{z} = \mathbf{3}$ *m while blue line corresponds to* $\mathbf{z} = \mathbf{6}$ *m; "green" winds are from the starboard side of the ship and "red" winds from the portside [41]*

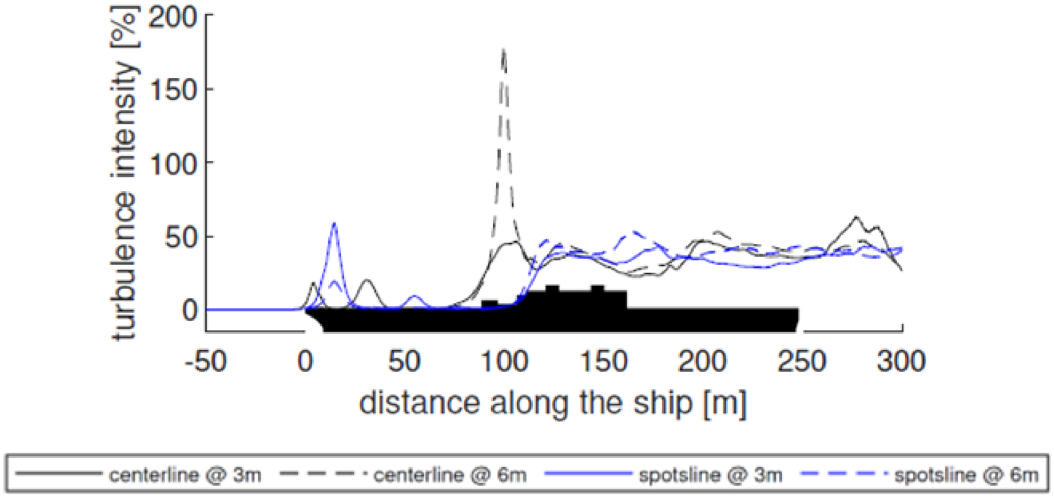

a) Green 30°

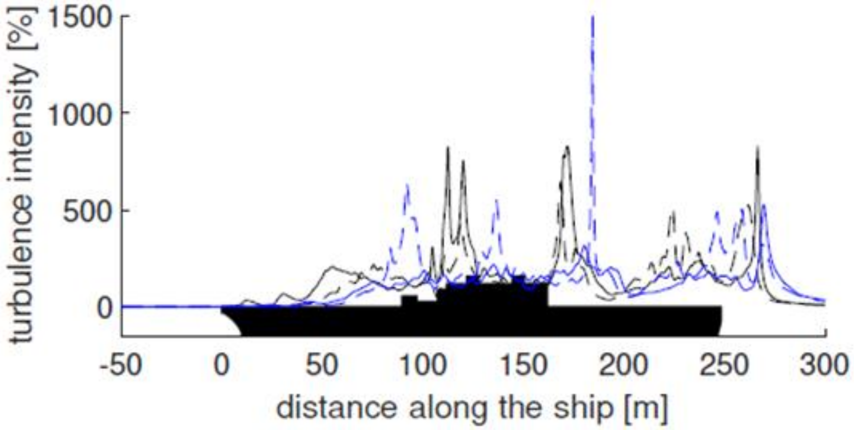

b) Green 60°

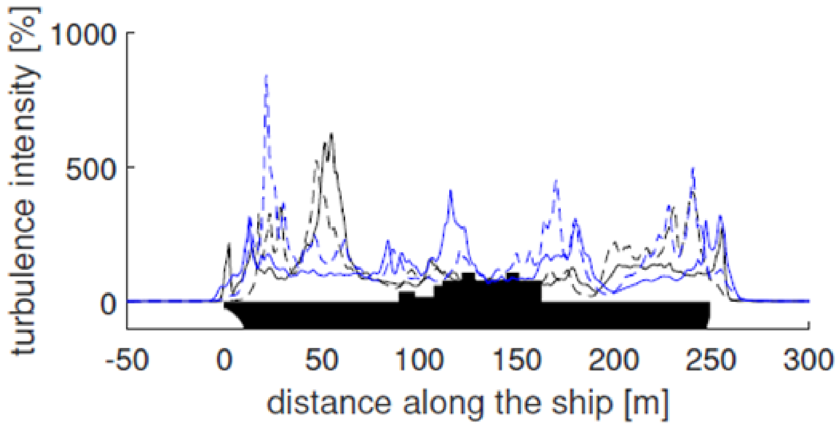

c) Green 90°

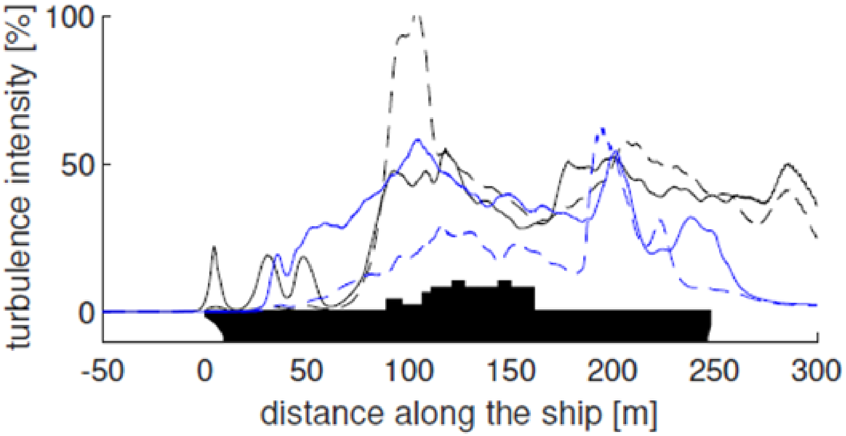

d) Red 30°

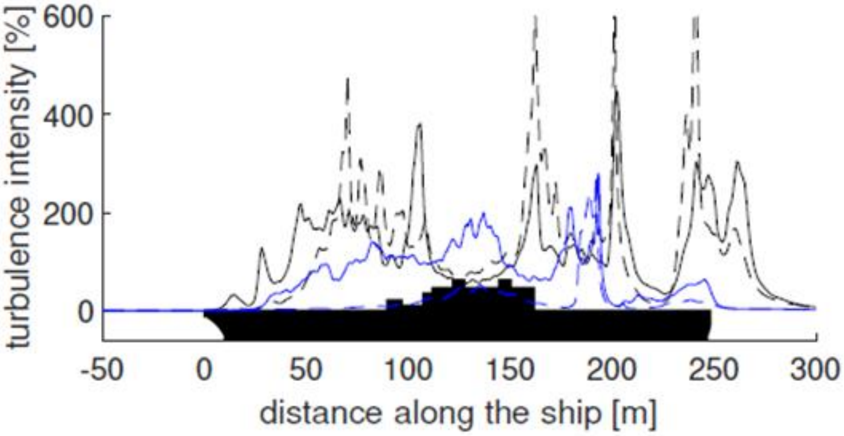

e) Red 60°

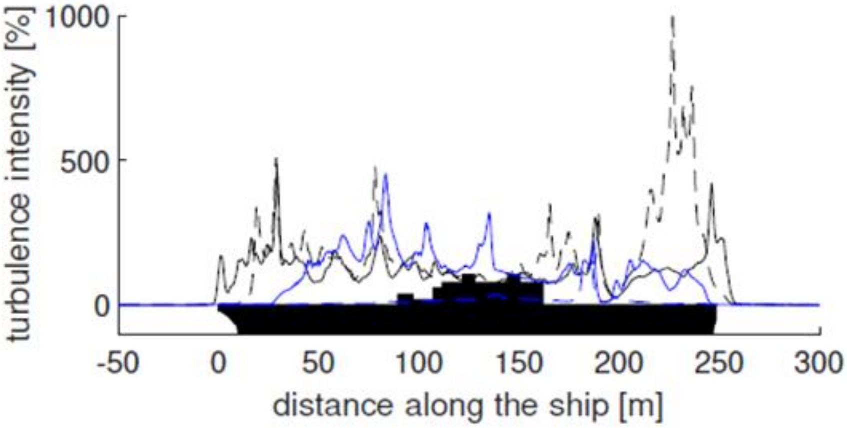

f) Red 90°

Figure 31: Turbulence intensities across LHA ship length for various WOD conditions; "green" winds are from the starboard side of the ship and "red" winds from the portside [41]

CFD and experimental investigations of flow over Her Majesty's Ship (HMS) Queen Elizabeth Class (QEC) aircraft carrier shown in Figure 32 were performed in Refs. [42, 43].

HMS QEC provides a 4-acre flight deck to support fixed- and rotary-wing aircraft, and includes a take-off ramp or “ski jump” to support short take-off, specifically for Lockheed Martin F-35B Advanced Short Take-Off and Vertical Landing (ASTOVL). A notable feature of this carrier is the twin island configuration with the front island serving as base for ship control and navigation and the rear one as base for flight operations. This twin island configuration results in greater turbulence over the deck span when compared to LHA class ships which have one island [42]. Watson et al. validated Delayed Detached Eddy Simulation (DDES) of flow over HMS QEC with measurements obtained from water-tunnel experiments of a 1/200th scale model [43]. Two Acoustic Doppler Velocimetry (ADV) probes were used to measure mean velocity components and lateral and vertical velocity fluctuations. Water-tunnel experiments were performed to match Reynolds number to full-scale tests. CFD predictions of turbulence intensity, defined as

$$I = \frac{\left[\frac{1}{3}\left(\overline{u'^2} + \overline{v'^2} + \overline{w'^2}\right)\right]^{\frac{1}{2}}}{U_\infty}, \tag{6}$$

for the 1/200th scale model showed good agreement with experiments, as evident in Figure 33 [43].

Figure 32: HMS Queen Elizabeth aircraft carrier [43]

Subsequently, full-scale CFD simulations were performed with the atmospheric boundary layer modeled using surface roughness properties typical of oceanic surfaces [43]. Streamlines for headwind condition with turbulence intensity (see Eq. (6)) across a horizontal plane at $z = 10$ m are shown in Figure 34. Turbulence intensities of ~12% are noted due to the portside deck-edge vortex. Not surprisingly, peak turbulence occurs downstream to the superstructures, and similar plots for oblique WOD conditions are shown in Figure 35. For the green and red 25° and 45° WOD conditions, deck-edge vortices have turbulence intensities of ~20% across the deck. The greatest turbulence across the entire flight deck is evident in the green 90° condition.

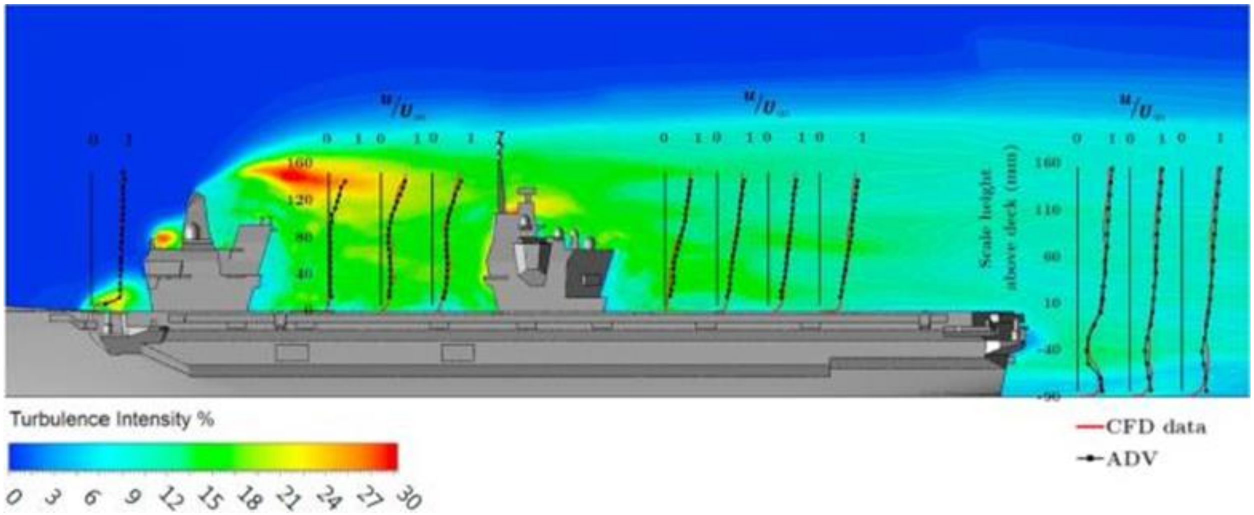

Figure 33: Comparison of experimental and CFD u-velocity components in a plane through center of islands [43]

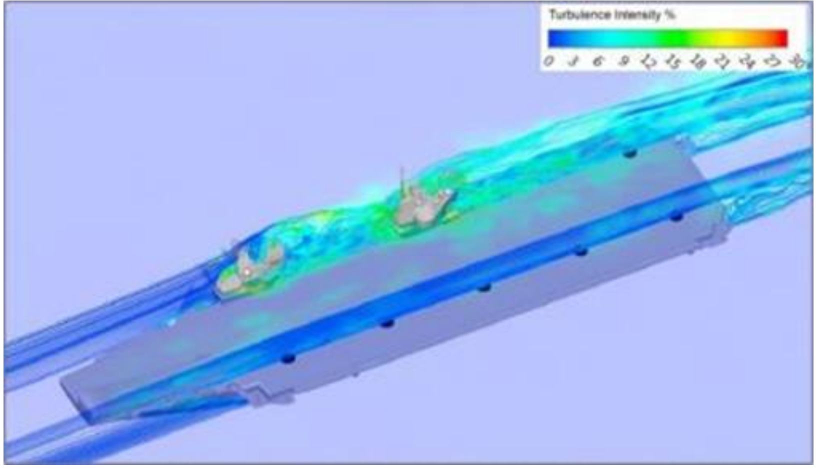

Figure 34: Streamlines for headwind condition in vertical planes through landing spots (black dots) and turbulence intensity contours in a horizontal plane 10 m above deck [43]

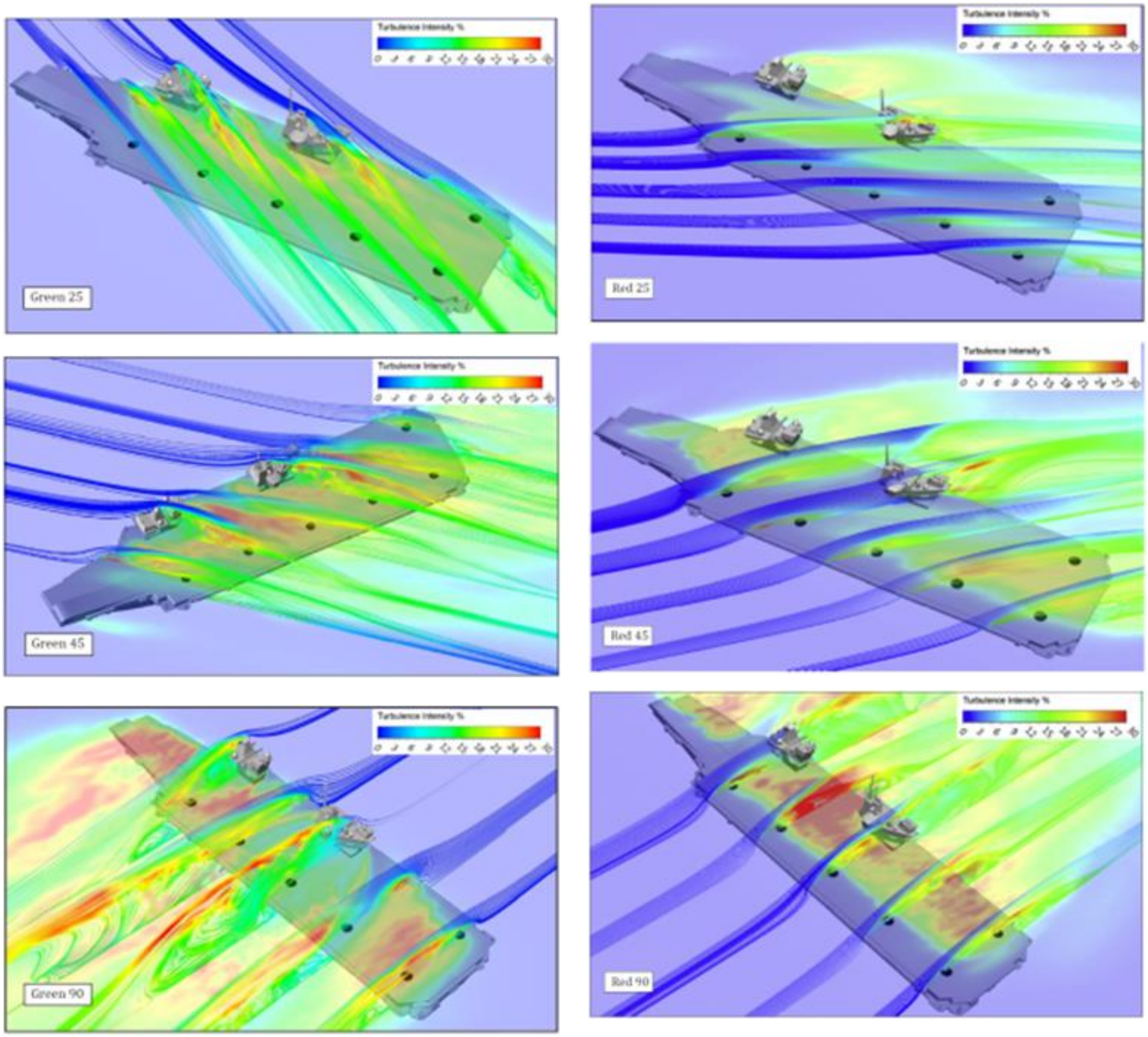

Figure 35: Streamlines in vertical planes for various WOD directions and turbulence intensity contours in a horizontal plane 10 m above deck [43]

From the preceding discussions, it is evident that the geometry of a ship superstructure greatly affects the flow patterns observed in the aft of ship. A comparison of the mean flow characteristics around the windward vertical edge of the hangar for an oblique WOD condition is shown in Figure 36 for the Simple Frigate Shape 2 (SFS2) and Type 23 (T-23) Frigate ship geometries [35]. The ship geometries are shown in Figure 37 for reference. The superstructure of the T-23 Frigate does not cover the entire width of the deck as that of the SFS2 and includes a "notch". Geometrical differences such as these greatly influence the resulting flow characteristics; the interaction of wind, the deck-edge vortex, and the superstructure results in a high vorticity region around the notch, which is not noted with the SFS2 in Figure 36.

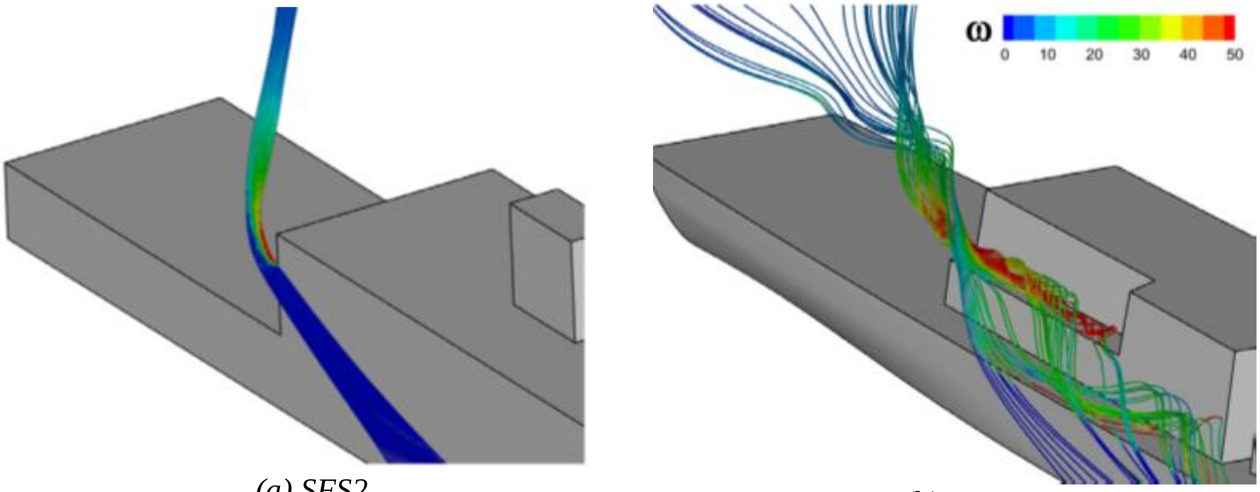

(a) SFS2

(b) T-23

Figure 36: Mean path lines colored by vorticity magnitude for starboard 45° WOD condition highlighting separation characteristics from windward hangar edge [35]

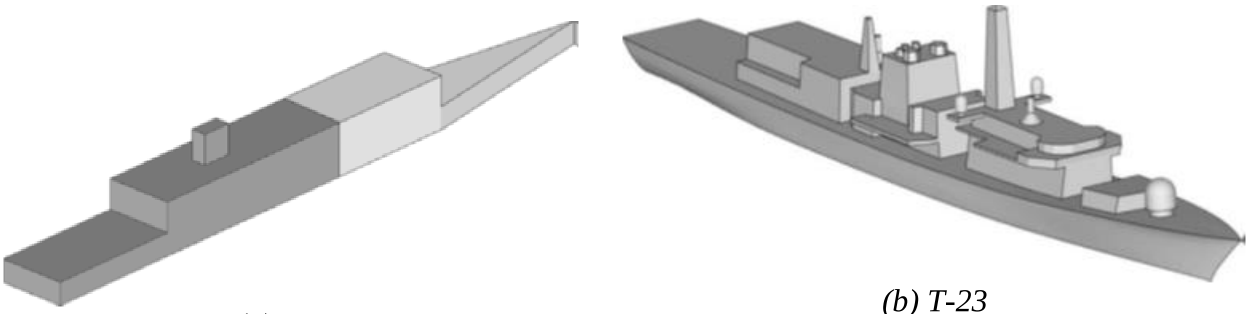

(a) SFS2

(b) T-23

Figure 37: SFS2 and T-23 ship geometries [35]

<u>Characterization of Corner Vortex Flow</u>

Deck-edge vortices on a ship originate from corners and propagate along edges of the deck and superstructure. In oblique WOD conditions, relatively strongcoherent vortical structures that can influence aircraft dynamics and handling qualities are shed from the corners. Characterization of flow features resulting from corner winds is lacking in ship airwake literature, but such phenomena have been looked at extensively by the wind engineering community given that vortices generated by corner winds can generate high suction regions on roofs of buildings, which, in turn, can lead to severe structural damage [44-47]. The large suction pressure regions are associated with two counter-rotating deck edge vortices that originate from the corner, as illustrated in Figure 38. In a similar manner to shear layers on backward facing steps, these vortices generate fluctuating pressure gradients by flapping over the top surface [44]. The size of each vortex depends on building dimensions, wind speed, wind incidence angle with the corner, and upstream (atmospheric) turbulence levels. Each vortex grows and decays alternatively (driven by the asymmetric shedding from the body), producing asymmetric instantaneous pressure distributions over the roof [48, 49]. Flow perpendicular to an edge produces separation bubbles over the edge and flow at an incidence angle of 45° results in symmetric vortices along the edges. The magnitude of the peak suction pressure over the top surface tends to be greater for flow with low turbulence [44].

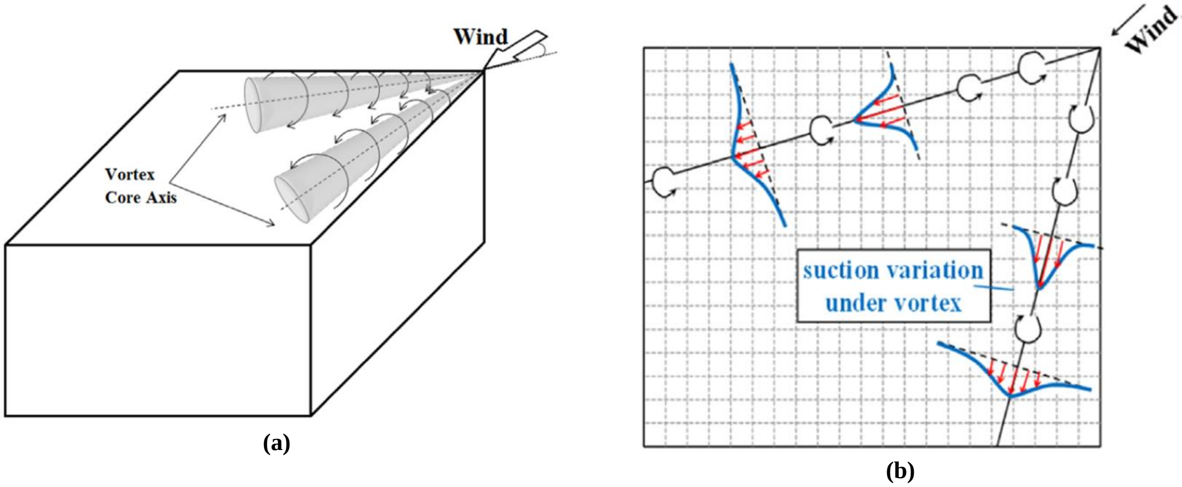

Figure 38: (a) Illustration of counter-rotating vortices generated, and (b) variation of suction pressure due to counter-rotating vortices over a flat roof from a corner wind [46].

Liu et al. in Ref. [45] performed wind tunnel experiments to assess the efficiency of passive vortex generators (PVGs) in mitigating pressure suction effects of the counter-rotating vortices on the top surface of a 1:244 scale model of a building that is 110 m long, 65.8 m wide, 22 m high and has a 5% roof slope—the centerline along the length of the roof is 1.64 m higher than the edges (5% of half of 65.8 m). An atmospheric turbulent boundary layer was simulated in the tunnel using the power law wind profile

$$U(z) = U_{ref}\left(\frac{z}{z_{ref}}\right)^{\alpha}, \tag{7}$$

where the power index α is set equal to 0.16, the roof height is taken as reference height z_{ref} with a corresponding reference speed U_{ref} of 8.6 m/s. Pressure measurements were undertaken following the pressure tape layout in Figure 39. Given the interest in flow phenomenology, only the baseline results without PVGs are of interest here.

Peak pressure coefficient C_p for various incidence angles are shown in Figure 40, indicating that the highest suction occurs at $\beta = 40°$ and tap #21, close to the left edge in the blue corner zone in Figure 39. In the context of shipboard landing, the vortex along this edge is similar to a deck-edge vortex on an aircraft carrier that can influence aircraft that are on or near landing spots close to the edge of the ship.

Liu et al. [45] also quantify the size of the vortices for the $\beta = 40°$ incidence condition, as shown in Figure 41. The vortex center axis (red line on the figure) is determined using the position of maximum mean suction pressure on cross-sections perpendicular to the wind direction. The radius of the vortex (black line on the figure) is estimated using the position of maximum root-mean-square (RMS) of pressure on the cross sections. The vortex along the longer edge of the building continually expands and moves away from the edge, while the vortex along the shorter edge expands slightly and remains closer to the edge. In general, the vortex along the edge that is at a smaller angle relative to the incoming flow is larger in size [44].

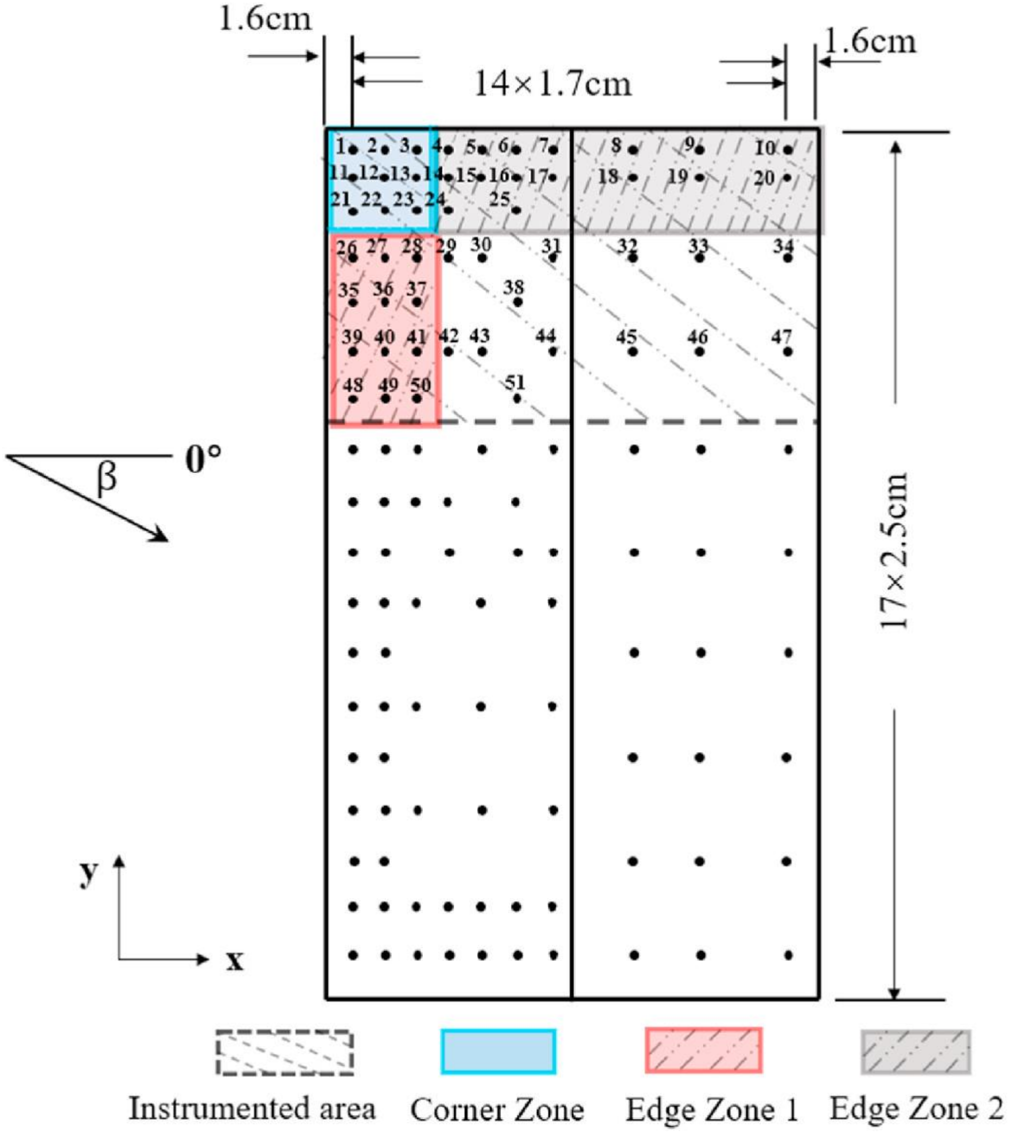

Figure 39: Pressure tap arrangement on top surface of building in Ref.[45].

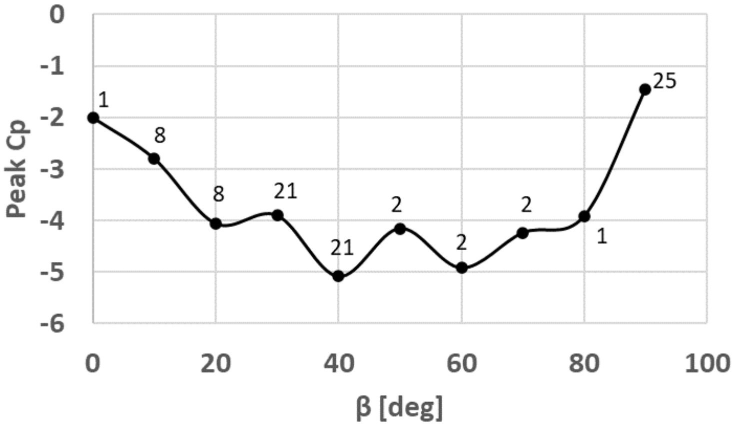

Figure 40: Peak C_p measured for different incidence angles; tap number indicated [45].

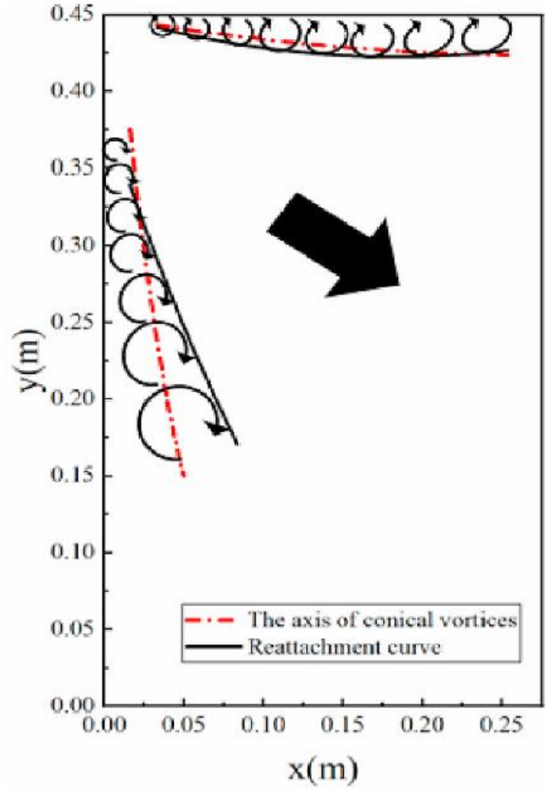

Figure 41: Range of counter-rotating vortices for $\boldsymbol{\beta} = \mathbf{40}°$ *condition. Adapted from [45]. Please note that there is an error in the original paper that shows the sign of the vortex along the shorter edge pointing in the opposite direction.*

Power spectral density (PSD) plots of pressure measurements at tap #21 for $\beta = 40°$ and tap #2 for $\beta = 70°$ are shown in Figure 42 and Figure 43 respectively, where $f \cdot H/U$ is the Strouhal characterization frequency with building height H as the characteristic dimension, and $f \cdot S(f)/\sigma^2$ is the dimensionless power spectrum with $S(f)$ being the measured pressure spectrum and σ^2 is the variance of the measurements [45]. It should be noted that pre-multiplying the frequency by $S(f)/\sigma^2$ always results in peaks in the spectrum, even if the pure signal does not contain any dominating periodicity [44]. The "NO PVG" plots in Figure 42 and Figure 43 are of interest here, and show that for $\beta = 40°$, the most energetic flow feature occurs at a Strouhal frequency of 0.07 with additional peaks at higher values such as 0.15 and 0.17. For $\beta = 70°$, the most energetic flow features occur at Strouhal frequencies of 0.07, 0.13 and 0.19.

Kozmar in Ref. [44] experimentally investigated the pressure distribution and fluctuations over the top surface of a 0.2 m wall-mounted cube due to corner winds for three simulated atmospheric boundary layers corresponding to low- (LT), mid- (MT) and high-turbulence (HT) levels. The power index α in Eq. (7) was set to 0.17, 0.21 and 0.35, for values of U_{ref} of 14.97, 13.48 and 10.14 m/s, respectively with flow incidence angle of 40°. Contours of the steady pressure distribution over the cube are shown in Figure 44 showing that the magnitude of the suction peak on the top surface decreases with increasing upstream turbulence level.

The root-mean-square (RMS) of the pressure coefficient ($C_{p,rms}$) along three lines on the top surface of the cube are shown in Figure 45. Figure 45(a) shows $C_{p,rms}$ underlying the conical vortex along the leading edge. The pressure peaks close to the corner of the cube and decreases downstream as the vortex tube expands. In Figure 45(b), a decrease in suction pressure is noted closer to the edge, where the boundaries of the two counter-rotating vortices interact. The line considered in Figure 45(c) starts at a region outside the vortex, progresses towards the center, and ends in a region underlying it. Suction pressure underneath the vortex is approximately 3-4 times higher than that outside the vortex, indicating the potential adverse impact these vortices can have on the surface and on aircraft operating within it. For all three profiles, increasing the upstream turbulence level results in greater flow diffusion over the top surface. Greater fluctuations in $C_{p,rms}$ were observed, but it is not clear whether this is a consequence of unsteadiness in the inflow, or the vortices moving more.

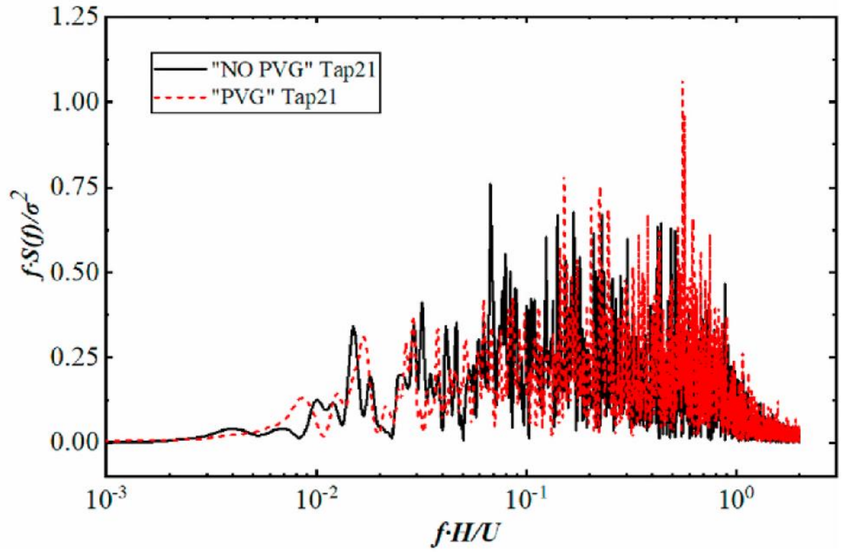

Figure 42: Power spectrum of pressure measurements at tap #21 for $\boldsymbol{\beta} = \mathbf{40}°$ *[45].*

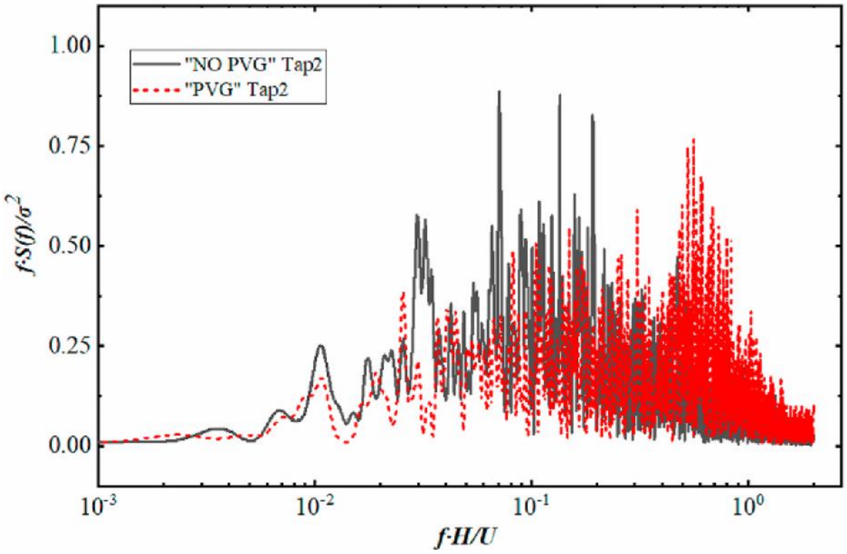

Figure 43: Power spectrum of pressure measurements at tap #2 for $\boldsymbol{\beta} = \mathbf{70}°$ *[45].*

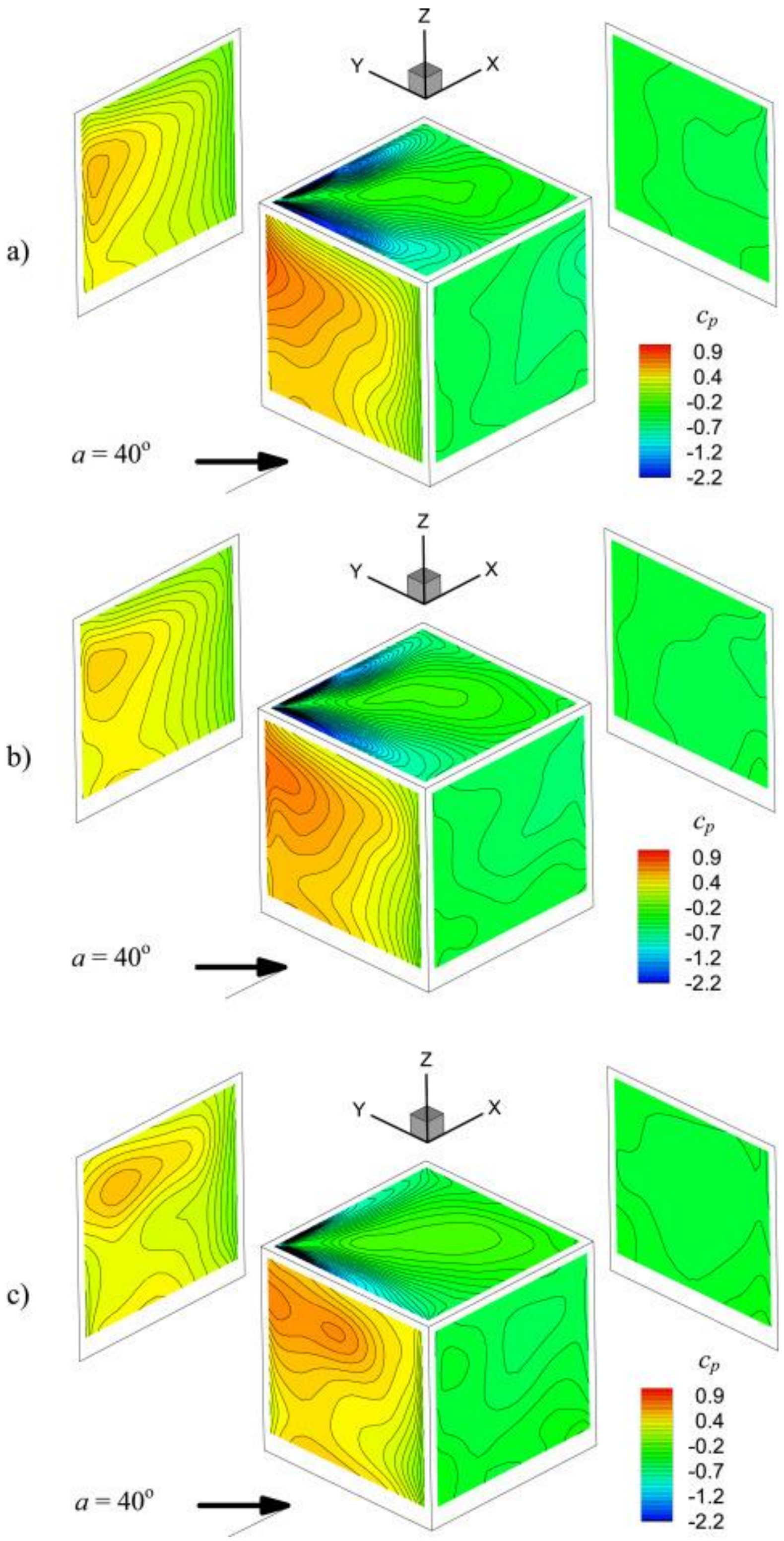

Figure 44: Contours of steady pressure distribution over surfaces of a cube for a corner wind at an incidence angle of 40° [44].

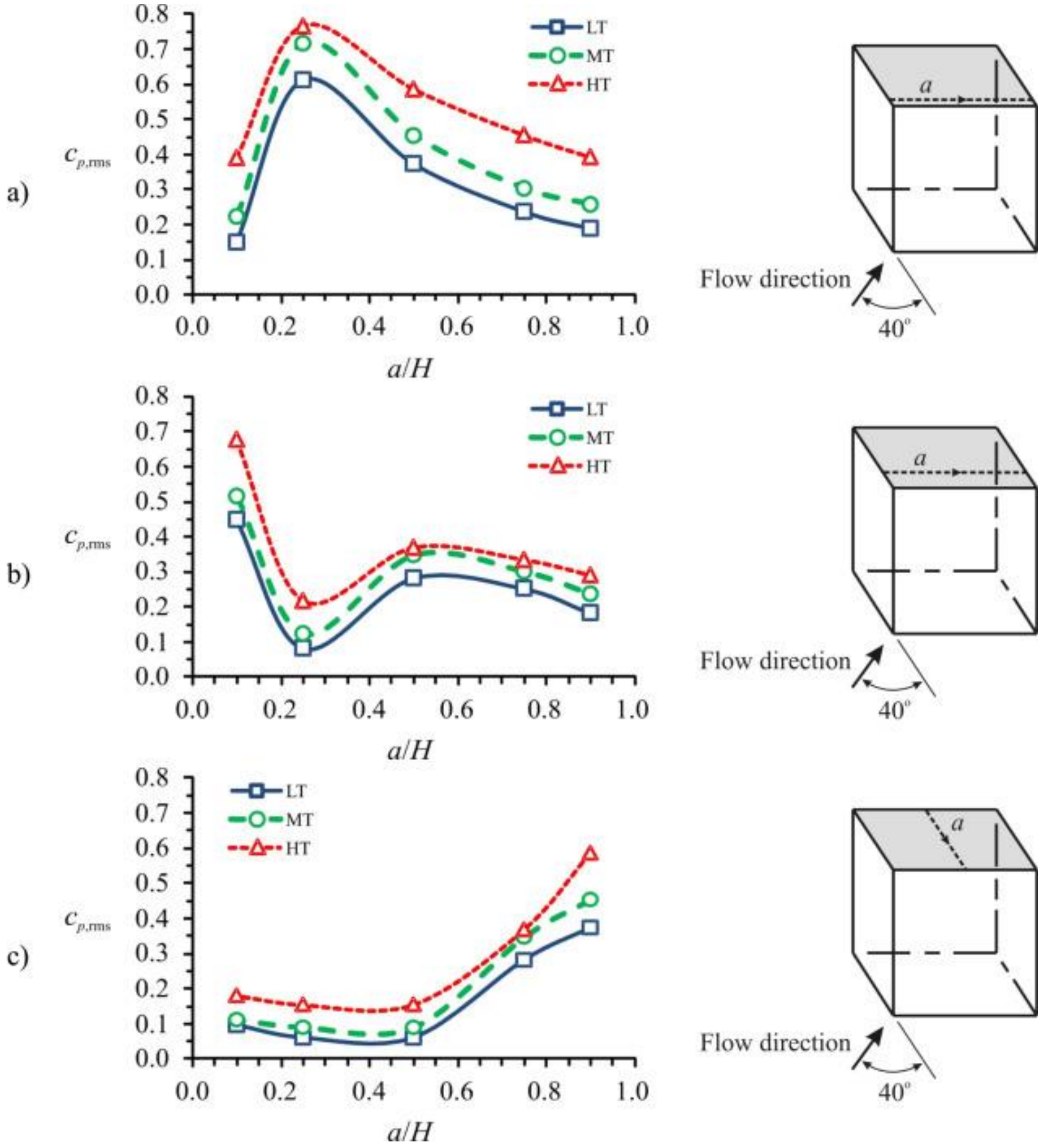

Figure 45: Profiles of $\boldsymbol{C_{p,rms}}$ coefficients on the top surface of the wall-mounted cube at (a) $\boldsymbol{x/H = 0.1}$, (b) $\boldsymbol{x/H = 0.25}$ and (c) $\boldsymbol{y/H = 0.5}$ [44].

Power spectral density plots of surface pressure fluctuations at various points along the three lines considered in Ref. [44] (see Figure 46 to Figure 48). Close to the corner at point #1 in Figure 46 , vortex shedding due to the body edges occurs at a characteristic (for a cube [25]) Strouhal frequency of 0.1. As the vortex develops from point #1 to #5, the primary frequency progressively shifts to ~0.03 and a secondary peak at $St = 1.0$ emerges and becomes dominant. This change in periodicity has been attributed to reattachment of the flow on the top surface downstream from the corner [44]. The shift in primary periodicity is also noted in PSD plots for the $x/H = 0.25$ profile in Figure 47. The secondary high-frequency peak is not as pronounced along this profile. The PSD plots in Figure 48 correspond to a profile where points #3 and #8 are outside the conical vortex region and points #11 and #12 are underneath the conical vortex. Outside the conical vortex region, the dominant periodicity occurs at $St = 0.03$ with a less pronounced secondary peak at $St = 2.0$. As we move along the profile into the region underneath the vortex, the secondary peak at $St = 2.0$ becomes more dominant.

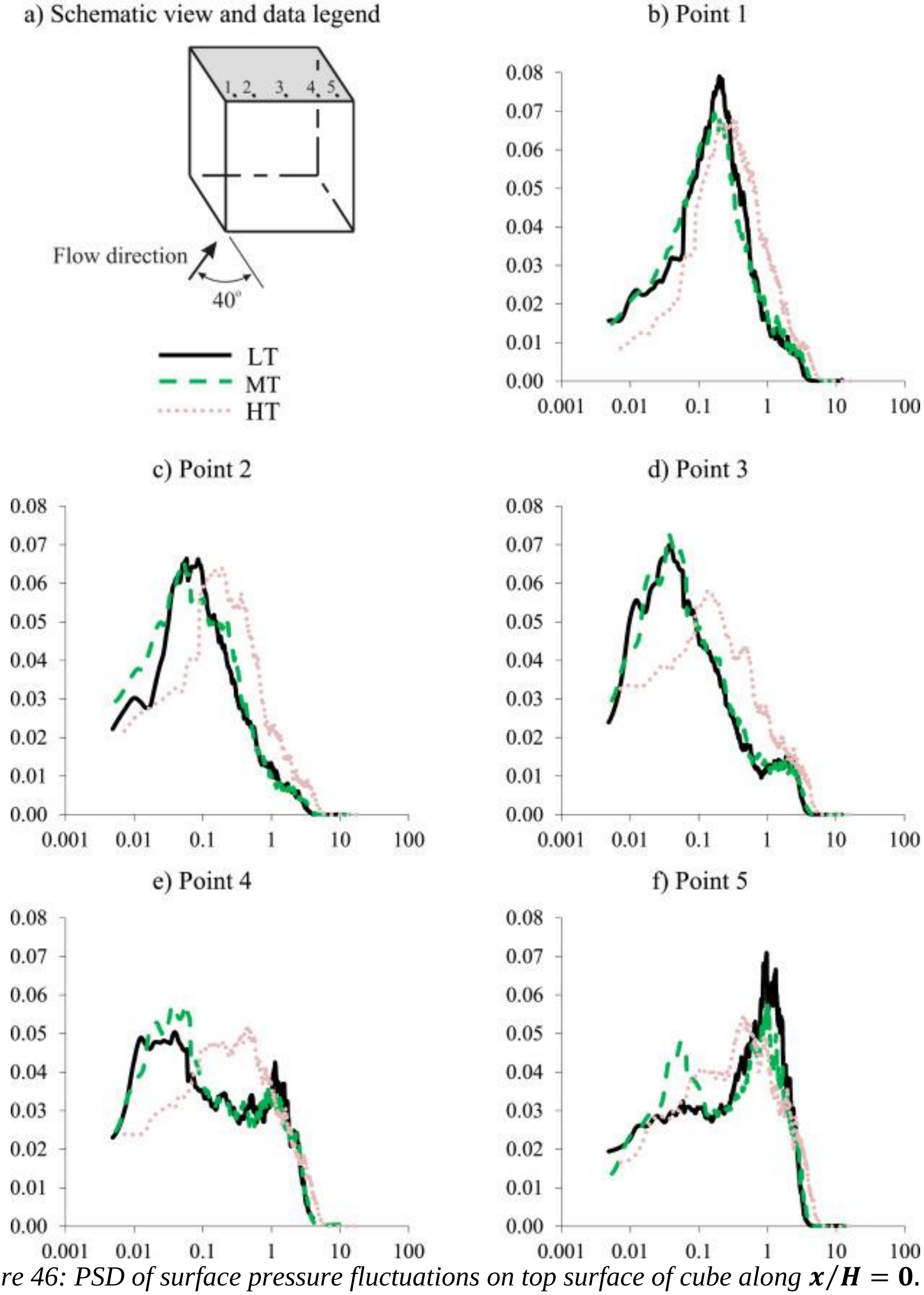

Figure 46: PSD of surface pressure fluctuations on top surface of cube along $\boldsymbol{x/H = 0.1}$; $\boldsymbol{x}$-axis is Strouhal frequency $\boldsymbol{f \cdot H/U}$ and $\boldsymbol{y}$-axis is the dimensionless power spectrum [44].

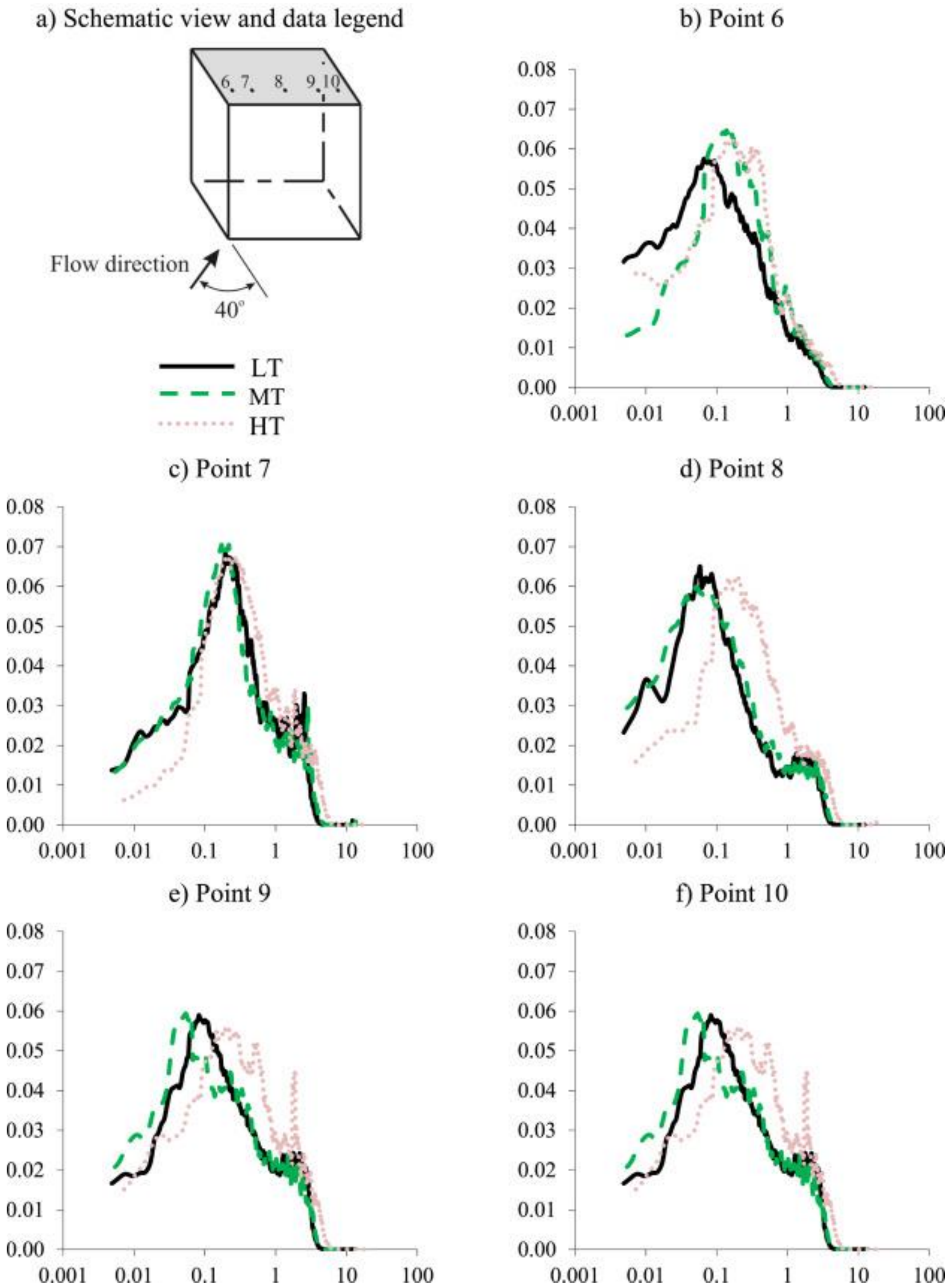

Figure 47: PSD of surface pressure fluctuations on top surface of cube along $x/H = 0.25$; x-axis is Strouhal frequency $f \cdot H/U$ and y-axis is the dimensionless power spectrum [44].

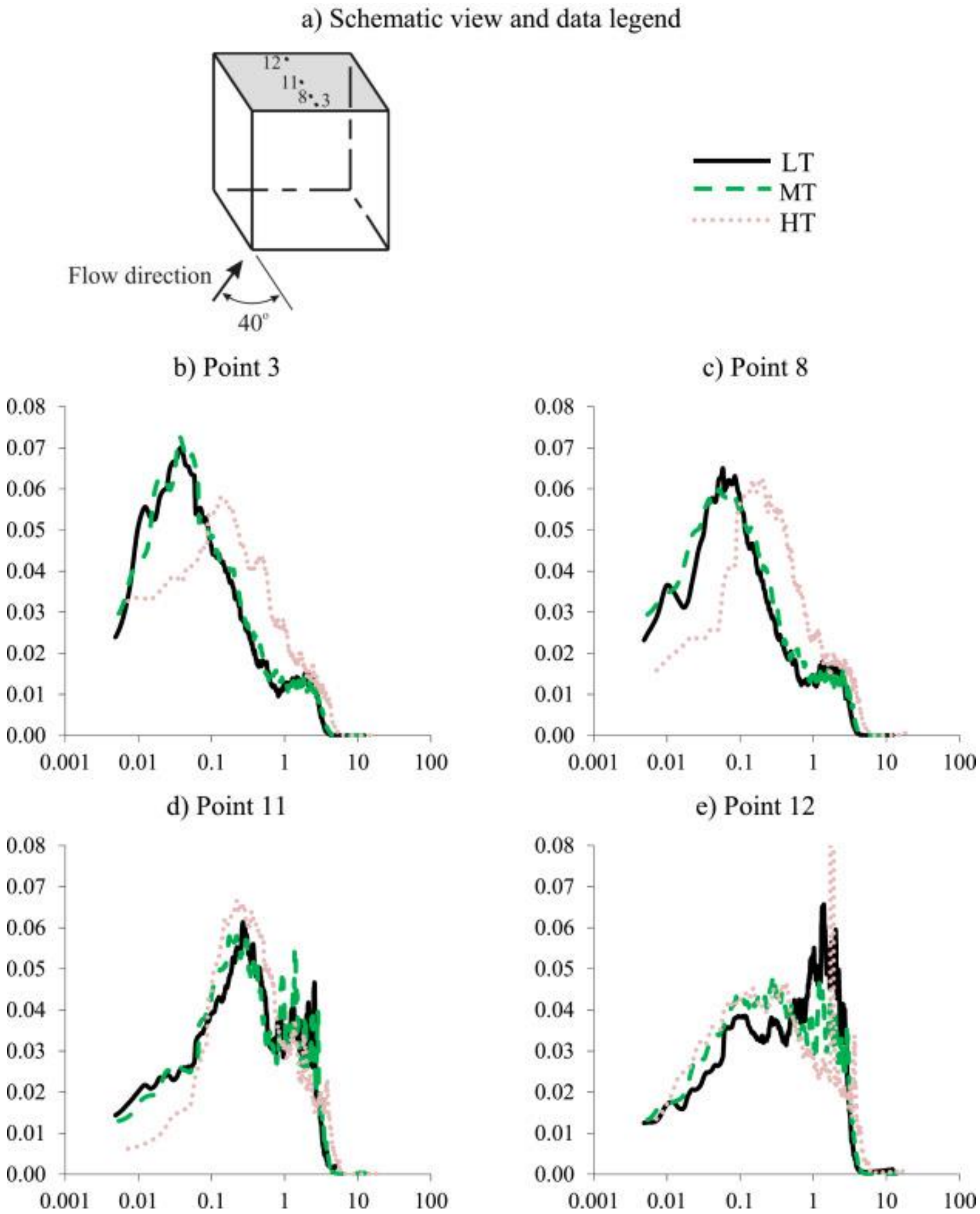

Figure 48: PSD of surface pressure fluctuations on top surface of cube along $\boldsymbol{y/H = 0.5}$; $\boldsymbol{x}$-axis is Strouhal frequency $\boldsymbol{f \cdot H/U}$ and $\boldsymbol{y}$-axis is the dimensionless power spectrum [44].

From the preceding discussion, corner flow produces a complex distribution of pressure with varied periodicity over a surface. It is important to note that the wind engineering community tends to focus on surface level measurements. For the ship-helicopter DI scenario, we also need to characterize corner flow properties above and beyond the surface since those are the regions where aircraft operate.

Influence of Ship Motion on Ship Airwake

The ship-helicopter DI is further complicated by wave induced motion of the ship [50], which can alter the vortex shedding strength and frequency of the airwake, and also induce a phenomena known as vortex “lock-in” [51], where the natural airwake shedding frequencies are reinforced by oscillatory motion of the ship. These effects can in turn, influence pilot workload during shipboard operations. Most investigations in literature tend to focus on airwake over static ship configurations, with ship motion receiving attention only recently [51-54].

The influence of static and dynamic pitch attitude of a 1/100 scale model of the SFS2 ship geometry (see Figure 37) on ship airwake was investigated by Sydney et al. in Ref. [51] using PIV measurements of longitudinal and vertical velocities along the symmetry plane of the ship model. Time-averaged velocity magnitude contours for the baseline condition with the ship at an even keel in a headwind are shown in Figure 49 with relevant flow features highlighted.

When the ship is statically pitched, the wake boundary – the layer between the ship airwake and freestream - translates higher, as evident in Figure 50 [51]. Note that the pitch angle is applied relative to waterline point of the bow. Wake boundary translation is due to airwake from the bow and front step of the superstructure, both of which are located at greater heights when the ship is pitched compared to the baseline case. Corresponding TKE contours are shown in Figure 51. As pitch attitude increases, the point at which turbulent airwake contributions from the front step, funnel or stack, and rear step interact moves closer to the hangar, and the recirculation region immediately aft of the hangar shrinks. The magnitude of the turbulence above the ship also increases relative to the baseline case.

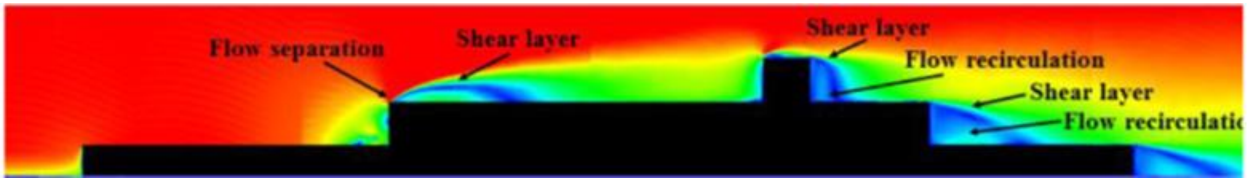

Figure 49: Time-averaged velocity magnitude over SFS2 model ship at even keel in a headwind; red indicates high velocity and blue indicates low velocity [51]

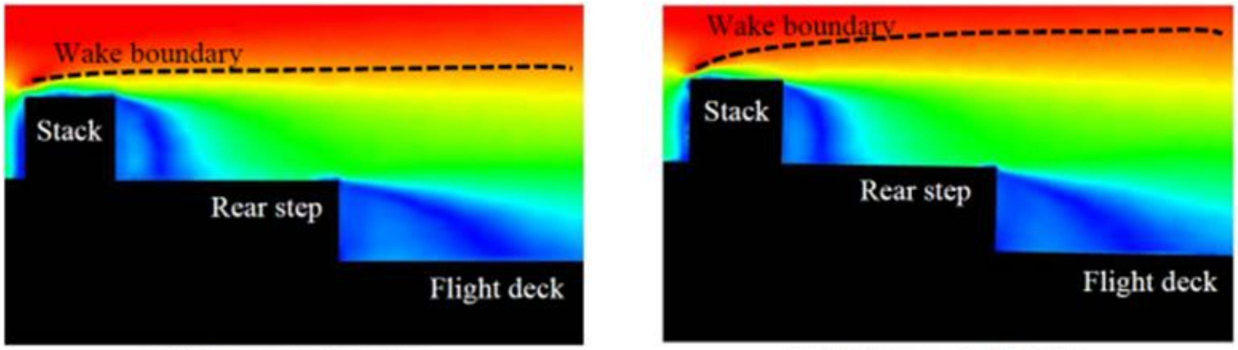

a. 0 degree pitch angle

b. 0.5 degree pitch angle

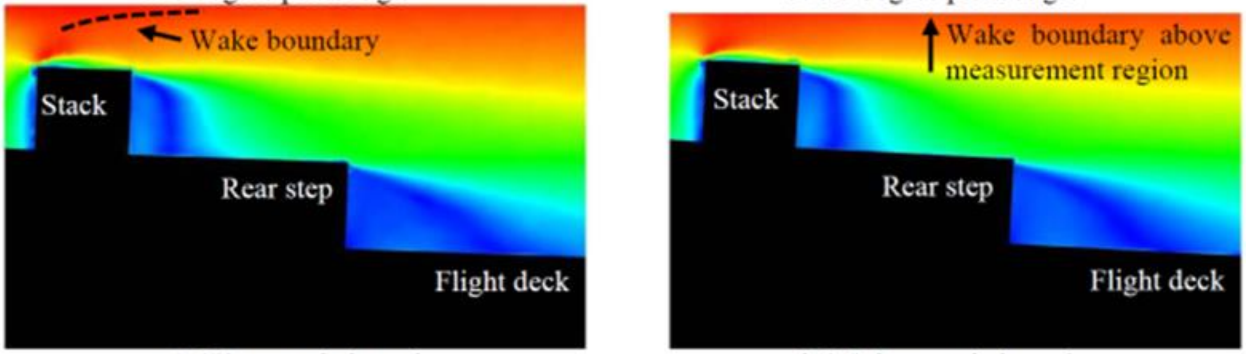

c. 1.5 degree pitch angle

d. 2.5 degree pitch angle

Figure 50: Effect of static pitch angle on mean velocity magnitude; red indicates high velocity and blue indicates low velocity [51]

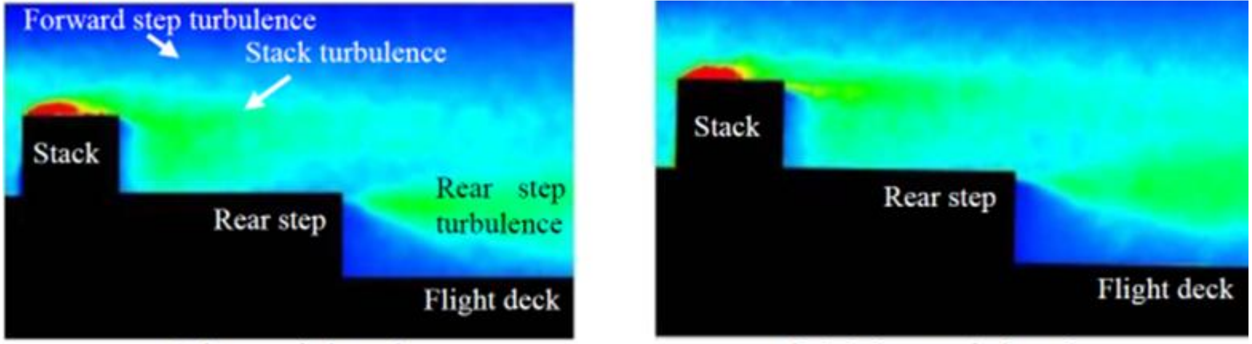

a. 0 degree pitch angle

b. 0.5 degree pitch angle

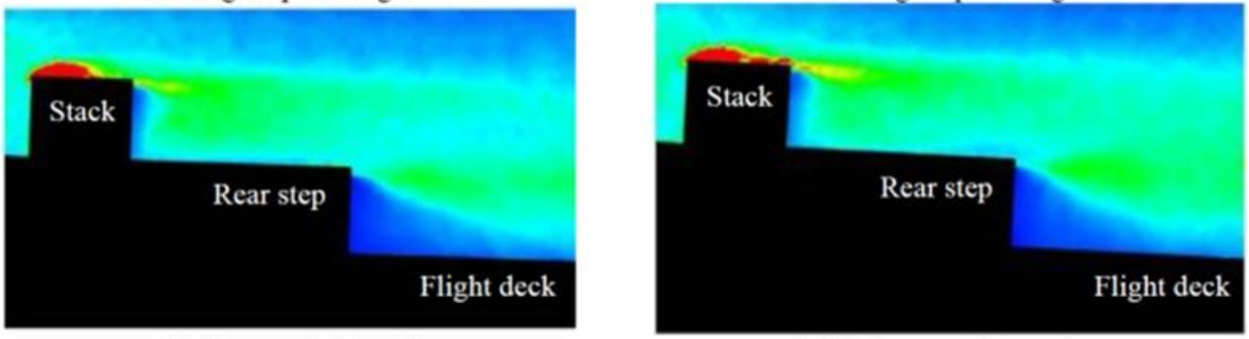

c. 1.5 degree pitch angle

d. 2.5 degree pitch angle

Figure 51: Effect of static pitch angle on TKE; red indicates high TKE and blue indicates low TKE [51]

Dynamic pitching of the ship at 1 and 2 Hz with an amplitude of 2.5° was also considered [51], and instantaneous velocity magnitude contours over one cycle are shown in Figure 52. The influence of deck motion is apparent when cases (b) and (d), corresponding to pitch attitudes of 0° with the bow moving up and down respectively, are examined. In case (d), flow perturbations are observed in the region where freestream was dominant in case (b), as indicated on the figure. These perturbations correspond to wake from the bow and front step that have convected downstream from the instance when these components were pitched upwards. Therefore, there is a lag between ship motion and airwake response over the deck. The frequency spectrum of velocity magnitude at a point located horizontally at the hangar and vertically at 1.4 hangar heights is shown in Figure 53, and not surprisingly indicates that there is an additional primary frequency in the wake associated with the ship motion frequency [51].

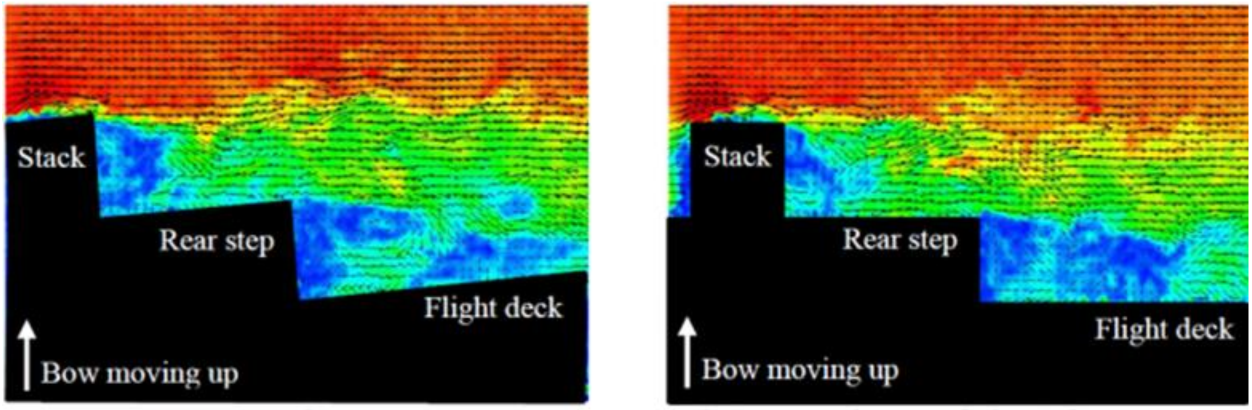

a. Bow moving up

b. Bow moving up, pitch = 0 degrees

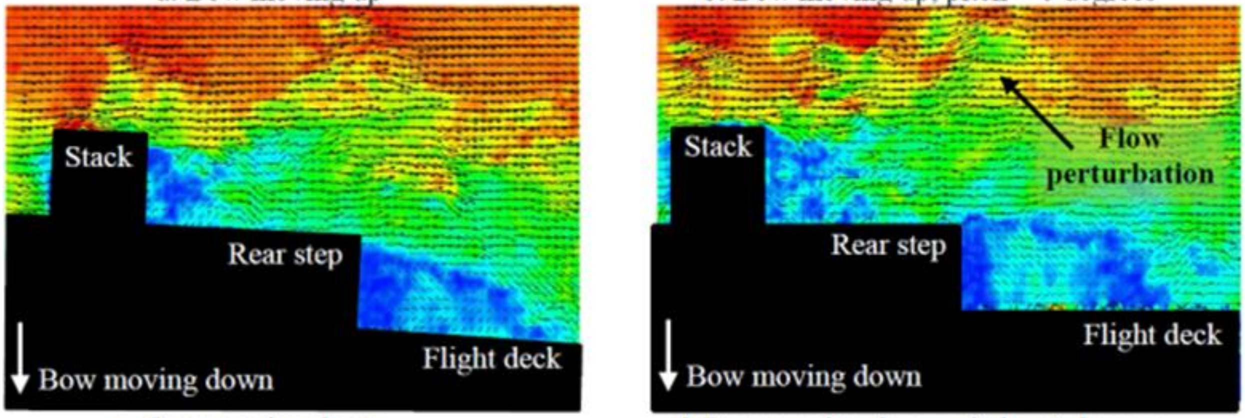

c. Bow moving down

d. Bow moving down, pitch = 0 degrees

Figure 52: Instantaneous contours of velocity magnitude over one period of pitch motion [51]

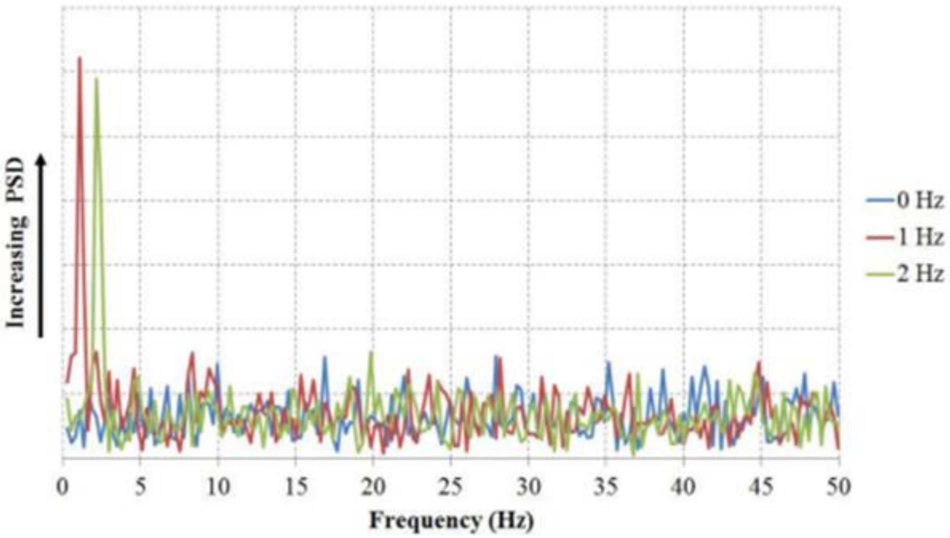

Figure 53: Spectrum of velocity magnitude at a point located horizontally at hangar and vertically at 1.4 times hangar height with ship oscillating in pitch attitude [51]

Similar observations were made by Yuan et al. [52] in experimental investigations of flow over a 1/50 scale model of a Canadian Patrol Frigate (CPF) - Figure 54 - wherefour probes were used to measure airwake velocities on the deck. Isolated single DOF heave, roll and pitch motions at 0.08 Hz with amplitudes of 1.5 m, 3.4° and 5°, respectively, were considered for a headwind condition. Figure 55 shows the frequency spectra of velocity magnitude, and, not surprisingly, exhibits peaks at the ship motion frequency of 0.08 Hz heave and pitch excitation cases. The influence of roll motion on velocity magnitude is minimal, although this may not be the case for oblique WOD conditions, where deck roll attitude can cause the horizontal edges of the deck to effectively act as backward facing steps that can produce large regions of separation [55].

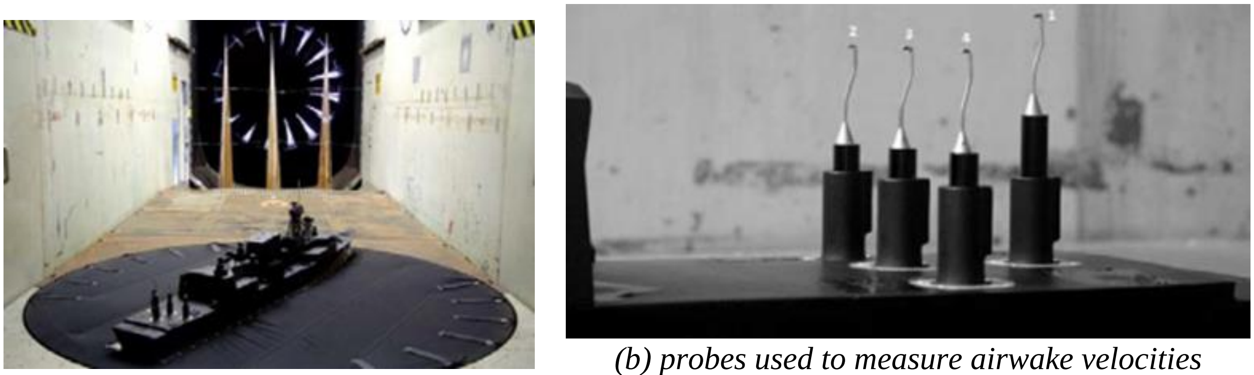

(a) wind tunnel setup

(b) probes used to measure airwake velocities

Figure 54: Model of CPF used by Yuan et al. during experimental investigations of influence of ship motion on airwake [52]

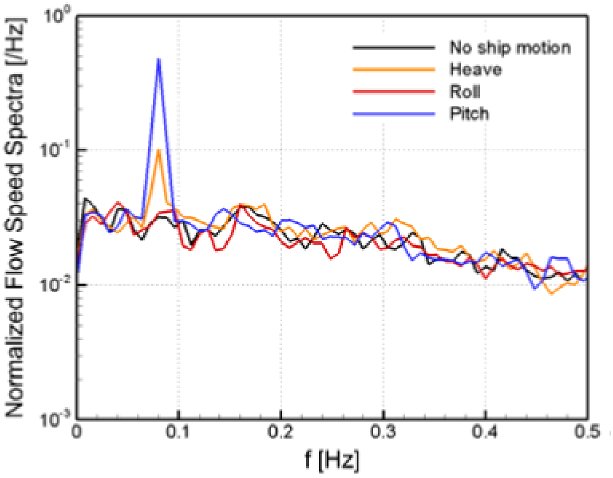

Figure 55: Spectrum of velocity magnitude measured by probe #3 from Figure 54(b) for isolated single DOF deck motion [52]

CFD investigations of the influence of ship motion using an ONR Tumblehome[1] (ONRT) ship geometry (i.e. Figure 56) were undertaken by Dooley et al. [53]. Dooley et al. noted that in addition to inducing deck motion, waves can influence the airwake by "pumping" air onto the ship, and thus performed CFD simulations that accounted for wave motion, wave-induced ship motion, ship forward speed and wind-at-sea [53]. Sea states #3 (SS3) and #6 (SS6) were simulated using wind speeds of 15 kts and 35 kts, respectively, and four simulations are performed for each sea state:

a) no wave motion and no ship motion included (baseline),
b) wave motion included but no ship motion (designated as "NM/WW" in figures),
c) no wave motion but ship motion included (designated as "WM/NW" in figures), and
d) both wave and ship motions included (designated as "WM/WW" in figures).

For conditions (b) and (d), the wave and ship motions determined from case (d) are superimposed individually in the simulation. The REX CFD code - a dynamic overset, unsteady Reynolds Averaged Navier-Stokes (URANS) or DES/DDES solver with unique capabilities for ship hydro/aerodynamics - was used. Combined heave and pitch motions are considered, and ship motion for one wave cycle is shown in Figure 57, where a wave phase of 0° corresponds to the time instance when the wave crest or peak is at the bow and the wave trough is at $\lambda = 0.6\,L$, where λ is the wave length and $L = 154$ m is the ship length. From Figure 57, the magnitudes of pitch and heave motion for SS6 are approximately four times greater than those for SS3. The influence of SS3 motion was found to be minimal [53] and thus, this report will discuss findings from the SS6 simulations.

---

[1] The ONRT ship represents the research version of the U.S. Navy Zumwalt class destroyer DDG-100, which was designed to have a small radar cross section.

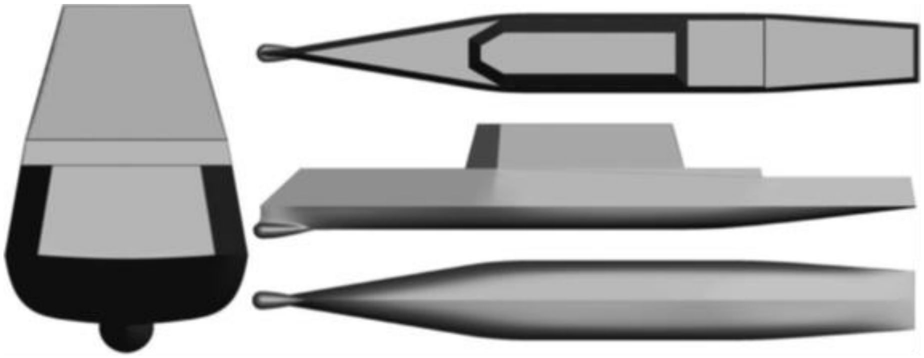

Figure 56: ONR Tumblehome ship geometry [53]

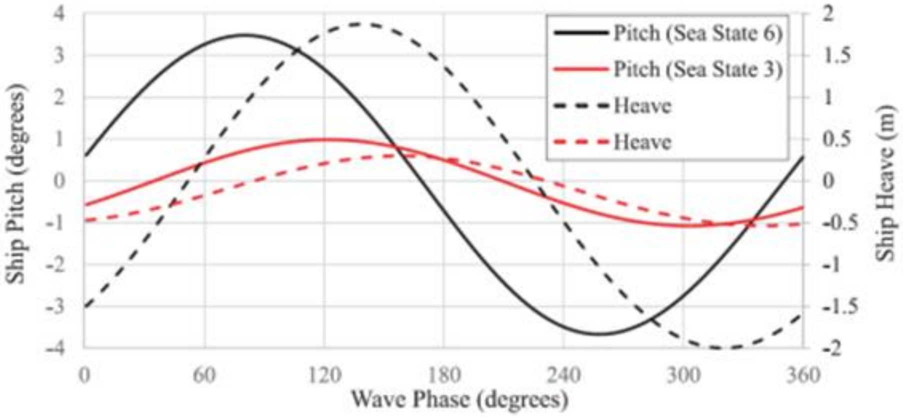

Figure 57: Ship pitch and heave motions through one wave encounter period for SS3 and SS6 [38]; 0° corresponds to the instance when the wave crest or peak is at the bow and the wave trough is at $\boldsymbol{\lambda = 0.6\ L}$, where $\boldsymbol{\lambda}$ is the wave length and $\boldsymbol{L = 154}$ m is the ship model length [53]

The influence of ship motion on flow features is depicted in Figure 58, where instantaneous isosurfaces of vortical structures over a period of motion are plotted for SS6 [53]. From the figure, the “V” deck-edge vortices from the bow occur periodically during the cycle, progressively disappearing as the bow reaches motion peaks. The necklace vortex between the hull and superstructure persists during the wave cycle, with its strength decreasing as the bow pitches up and increasing as the bow pitches down. The detached structures on the top and behind the superstructure also persist through the cycle. The recirculation region aft of the superstructure expands when the bow pitches up and contracts when the bow pitches down, indicating a translation of the deck impingement location of the shear layer shed from the superstructure top-aft-edge. Note that this shear layer translation occurs due to ship motion and represents a separate phenomenon from the shear layer flapping [12] described previously.

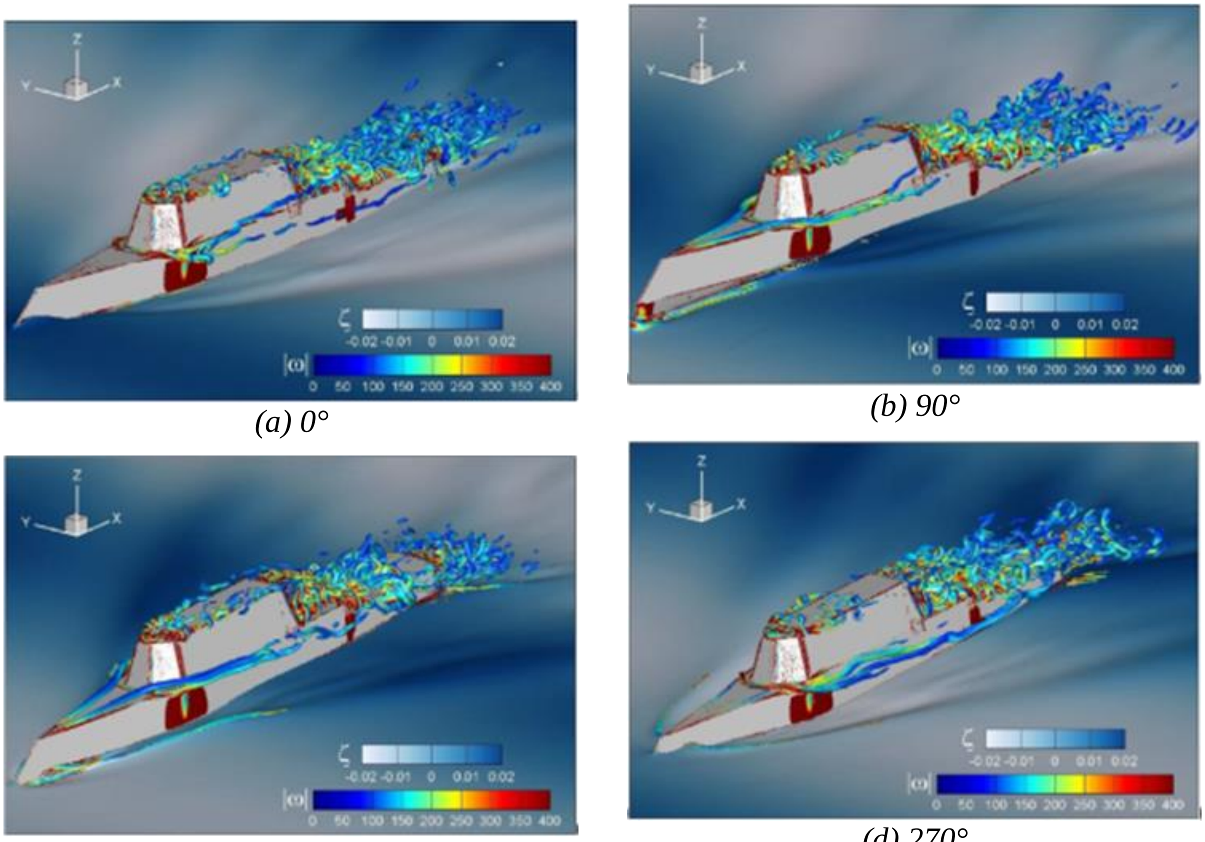

(a) 0° *(b) 90°*

(c) 180° *(d) 270°*

Figure 58: Isosurfaces of vortical structures for ONRT advancing at 15 kts in a 35 kts headwind (SS6) with wave and ship motion; 0° corresponds to the instance when the wave crest or peak is at the bow and the wave trough is at $\boldsymbol{\lambda = 0.6\ L}$, where $\boldsymbol{\lambda}$ is the wave length and $\boldsymbol{L = 154}$ m is the ship model length [53]

Root-mean-square contours of longitudinal and vertical velocity fluctuations for SS6 are shown in Figure 59, where velocities are nondimensionalized using a speed of $U_0 = 25$ kts [53]. Ship motion increases the RMS of both velocity components aft of the superstructure and stern when compared to the baseline, most notably for the longitudinal component. The influence of ship motion is further displayed on Figure 60, where phase-averaged deviations in longitudinal Δu_T and vertical Δw_T velocities from baseline mean velocities are plotted over one wave period. Phase-averaged velocities are obtained by time-averaging velocities recorded at specific wave phase angles during the simulation. Large changes of approximately $\pm 0.25 U_0$ are noted immediately aft of the superstructure in the longitudinal velocity component. Closer to center of the flight deck, where piloted operations take place, the deviations in longitudinal and vertical velocities are approximately $\pm 0.1 U_0$ and $\pm 0.2 U_0$, respectively. Note that the Dirichlet boundary condition used to model the ship geometry results in an upward velocity above the flight deck when the deck moves upward and conversely, generates a downward velocity when it moves downward [53].

Phase-averaged longitudinal and vertical velocities at a point located 30 ft above the center of the flight deck are shown in Figure 61, where the wave encounter period is 8.5 s [53]. The vertical displacement of mid-flight deck location is also shown on the figure. There is a ~90° lag evident between ship motion and the longitudinal velocity response in the WM/WW and WM/NW cases in Figure 61. The existence of this lag reinforces findings from Sydney et al. [51], discussed above. Peak-to-peak amplitude of the time-averaged longitudinal velocity reaches $0.25U_0$ relative to the baseline, while that of the vertical velocity reaches $0.1U_0$ in Figure 62. The vertical velocity response is also noted to be in phase with ship motion.

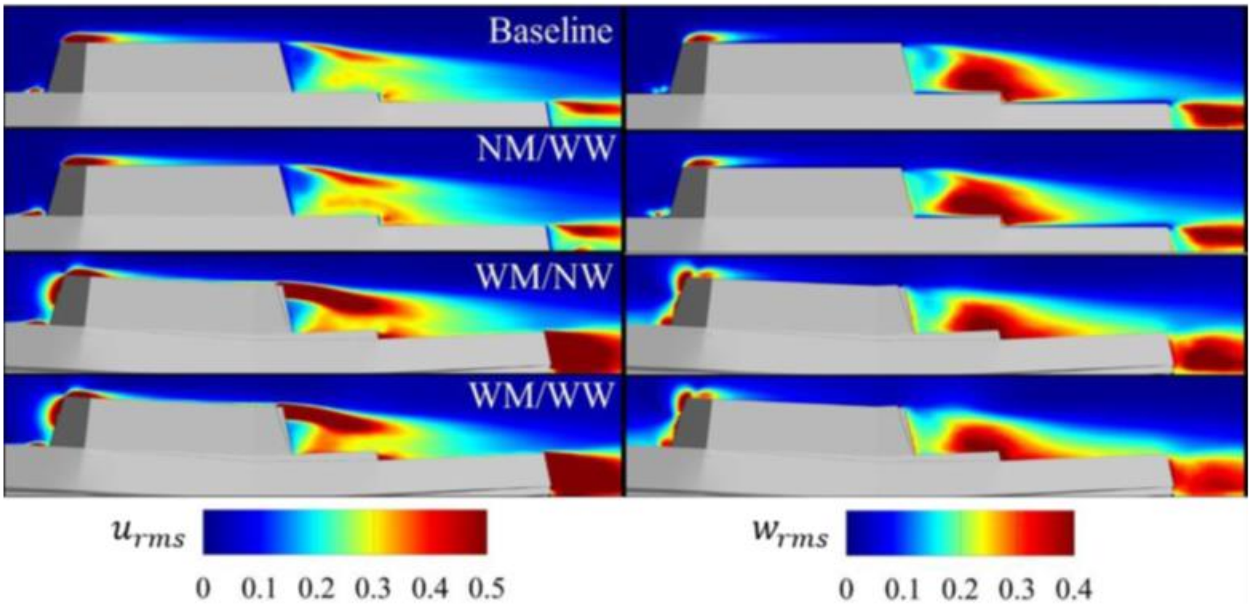

Figure 59: RMS of longitudinal (left) and vertical (right) velocity fluctuations for ONRT advancing at 15 kts in 35 kt headwind; "NM/WW" stands for "no ship motion/with wave motion", "WM/NW" for "with ship motion/with wave motion", "WM/WW" for "with ship motion/with wave motion"; velocities are nondimensionalized using an arbitrary speed of $\boldsymbol{U_0 = 25}$ *kts [53]*

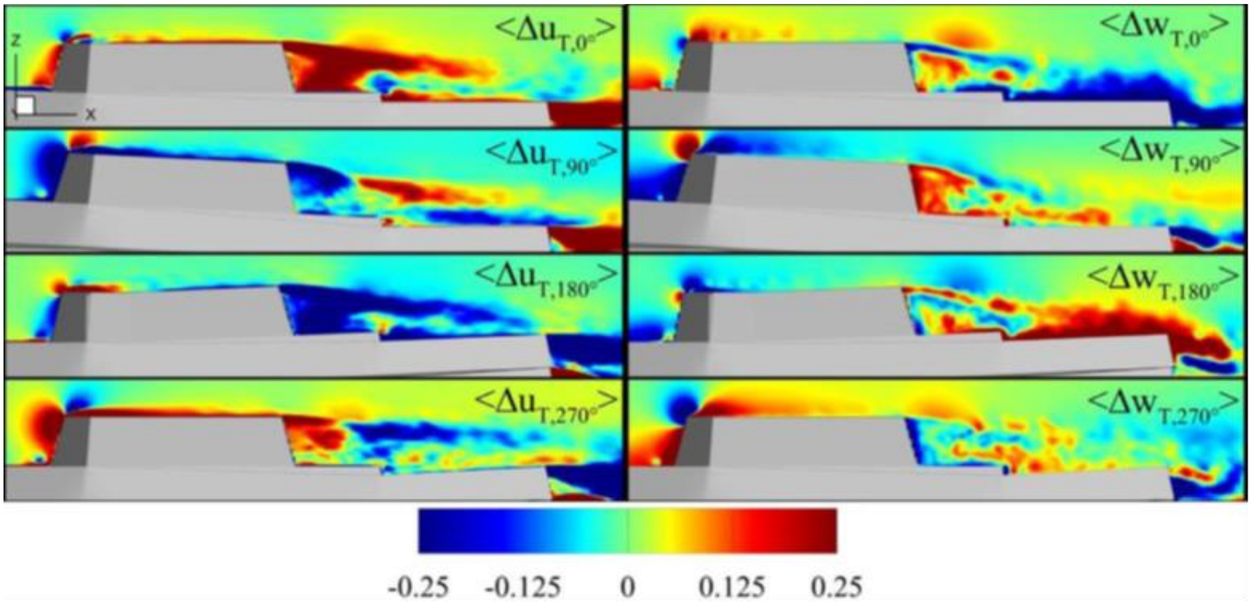

Figure 60: Phase-averaged deviations of longitudinal $\boldsymbol{\Delta u_T}$ (left) and vertical $\boldsymbol{\Delta w_T}$ (right) velocities from baseline over one wave cycle period; 0° corresponds to the instance when the wave crest or peak is at the bow and the wave trough is at $\boldsymbol{\lambda = 0.6\,L}$, where $\boldsymbol{\lambda}$ is the wave length and $\boldsymbol{L = 154}$ m is the ship model length; velocities are nondimensionalized using an arbitrary speed of $\boldsymbol{U_0 = 25}$ kts [53]

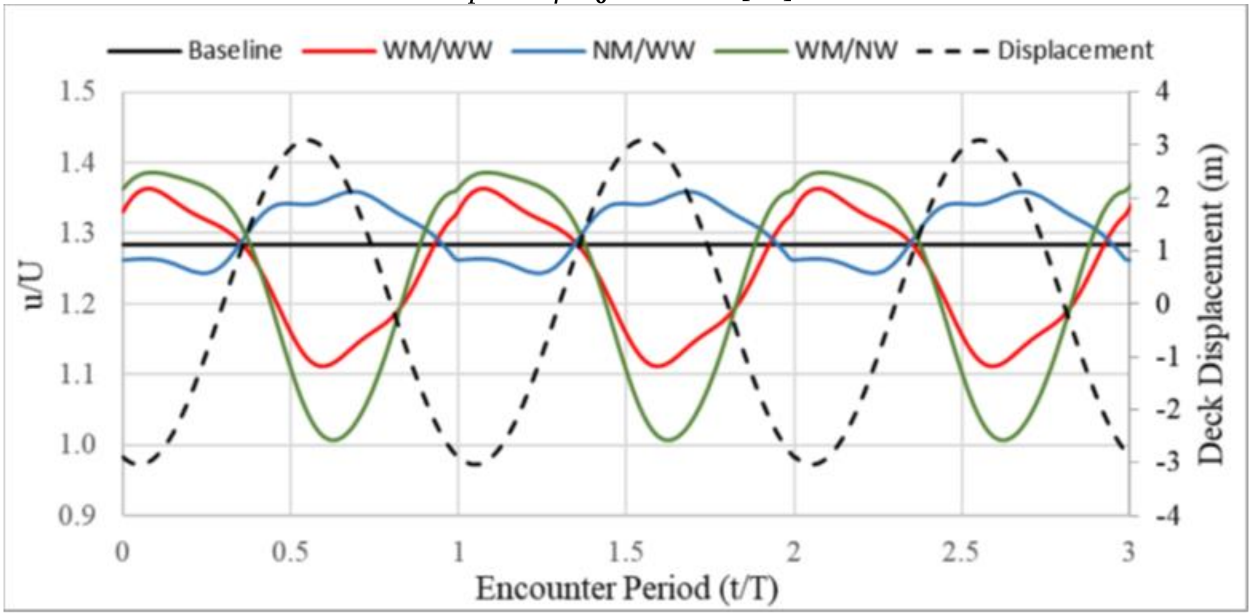

Figure 61: Phase-averaged longitudinal velocity at a point 30 ft above the center of the flight deck of ONRT advancing at 15 kts with a 35 kt headwind (SS6); wave encounter period is 8.5 s [53]

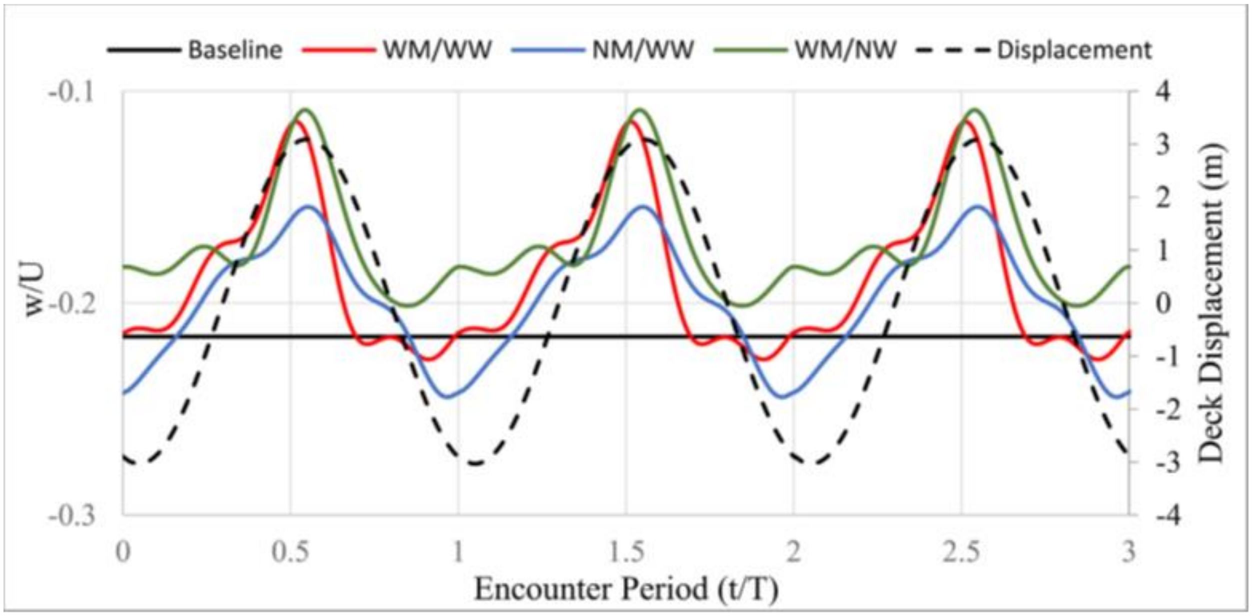

Figure 62: Phase-averaged vertical velocity at a point 30 ft above the center of the flight deck of the ONRT advancing at 15 kts with a 35 kt headwind (SS6); wave encounter period is 8.5 s[53]

Dooley et al. also investigate the influence of ship motion on helicopter dynamics using one-way and two-way coupled simulations [53]. One-way coupled simulations are performed using 3 scaled versions of a simplified SH-60 Seahawk rotor: a full-scale rotor with $D = 16.35$ m, a 50% scaled down rotor representative of a Robinson R22 rotor, and a 4.5% scaled down rotor representative of a drone. Simulations are performed with the rotor hovering 30 ft above the center of the flight deck. Time histories of rotor thrust are shown in Figure 63. All three rotors exhibit a degree of periodicity. The 0.045D rotor is noted to be most sensitive to the airwake, producing fluctuations with the largest magnitudes in Figure 63. In the context of the present ONR effort, this finding indicates the size of the rotor is an important factor to take into consideration when identifying airwake features that influence vehicle dynamics. The corresponding thrust frequency spectra for the three rotors are shown in Figure 64, where f_e is the wave encounter frequency. Thrust fluctuations for all three rotors are periodic with the wave encounter frequency f_e. Peaks are also evident at $2f_e$

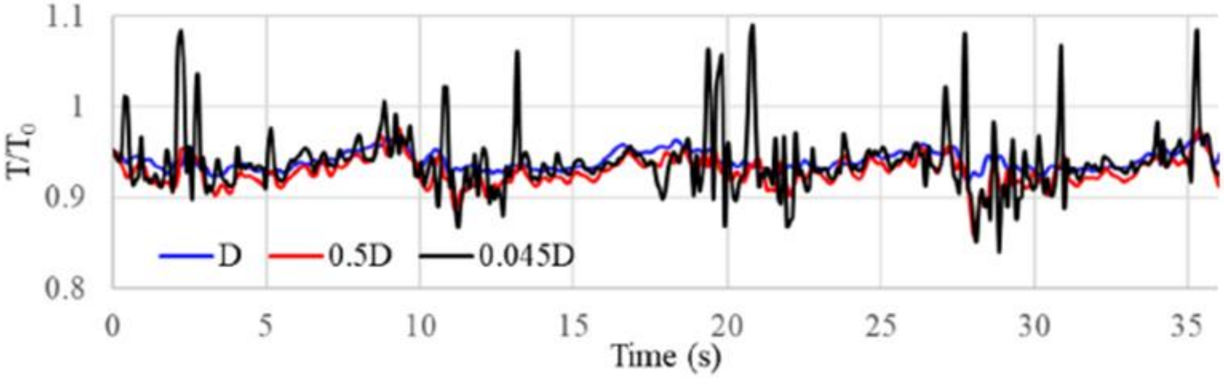

Figure 63: Instantaneous thrust produced by three scaled versions of a simplified SH-60 helicopter rotor model located 30 ft above the center of the flight deck of the ONRT ship advancing at 15 kts with a 35 kt headwind (SS6) during one-way coupled simulations [53]

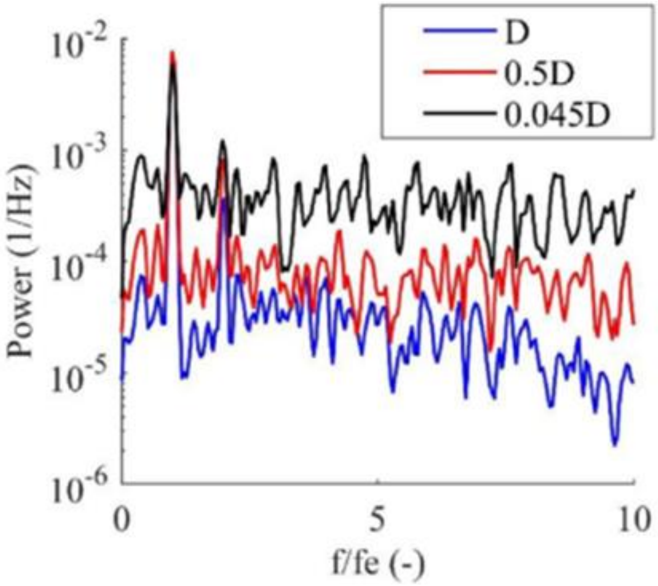

Figure 64: Frequency response function corresponding to thrust time-histories in Figure 63; $\boldsymbol{f_e}$ *is the wave encounter frequency [53]*

Two-way coupled simulations were performed using a generic helicopter loosely modeled after the SH-60 Seahawk helicopter [53]. The helicopter model had a forward speed of 15 kts to hold hover 30 ft above the center of moving ship deck (SS6). Trim was not performed, and the aircraft was held stationary above the deck using constant main and tail rotor collective inputs only. Time histories of the vertical force generated by the helicopter are shown in Figure 65 for three cases: isolated helicopter, helicopter hovering above advancing ship with no motions, and helicopter hovering above advancing ship deck with motion. The black line indicates instantaneous values while the red line represents a moving-average over one main rotor rotation. Ship motion causes the vertical force to change in a sinusoidal manner with peak changes of approximately 5 kN, relative to the 85 kN mean baseline. Note that these changes are a combined result of periodic ship airwake and dynamic ground effect from the moving deck, where part of the helicopter rotor downwash is redirected back towards to the rotor. Power spectral density plots of the vertical force shown in Figure 66 reveal periodicity with the wave encounter frequency f_e. Note that the CFD results presented by Dooley et al. [53] were not validated against experiments or full-scale test data.

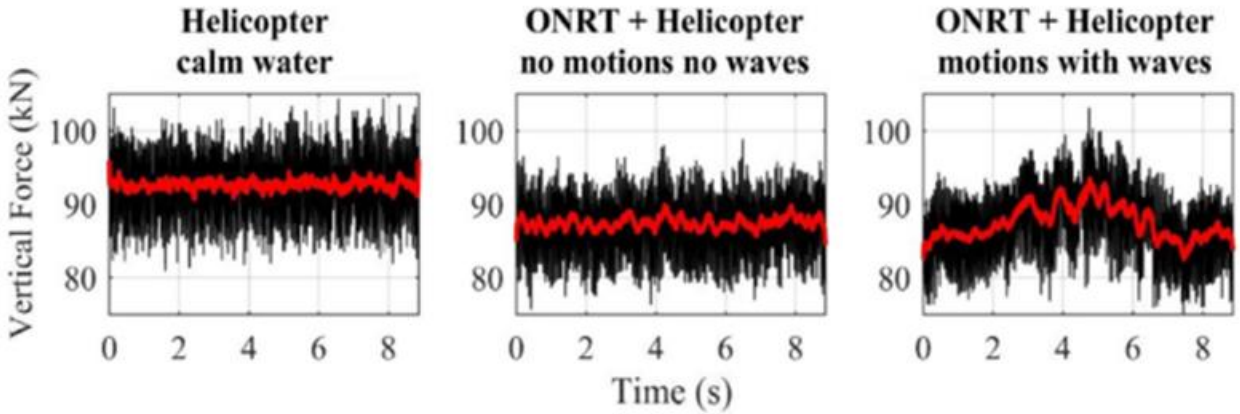

Figure 65: Time-histories of vertical force generated by a simplified SH-60 helicopter model located 30 ft above the center of the flight deck of the ONRT ship advancing at 15 kts with a 35 kt headwind (SS6) during two-way coupled simulations; black line indicates instantaneous values and red line represents a moving-average over one main rotor rotation [53]

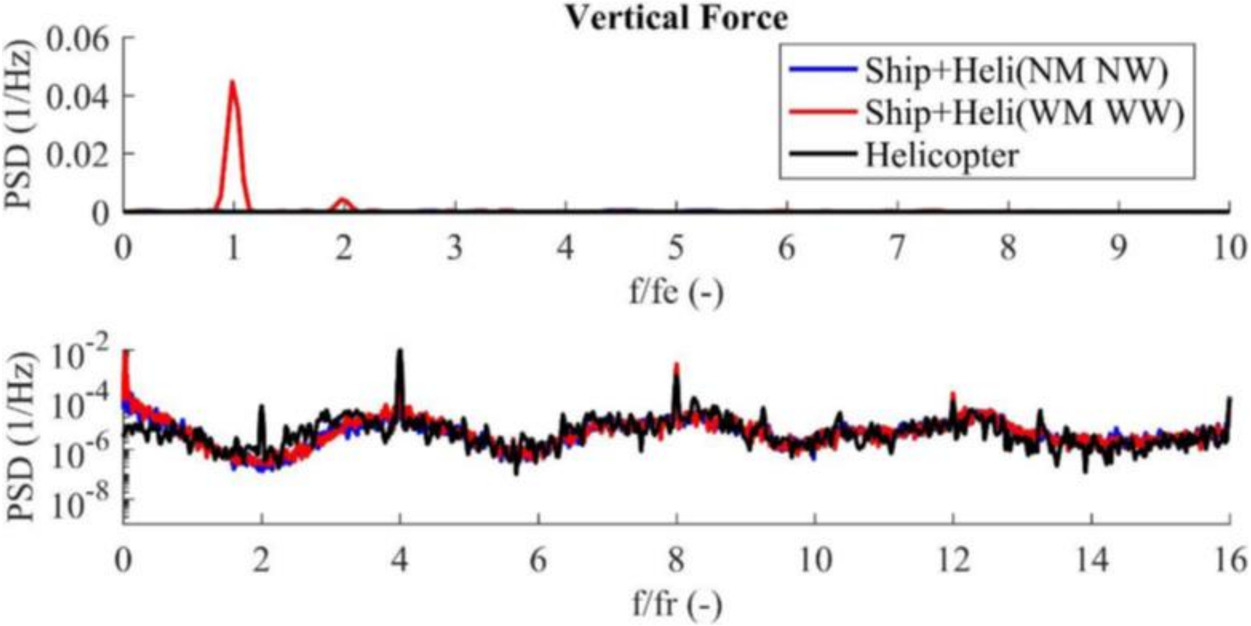

Figure 66: Frequency response functions corresponding to vertical force time-histories in Figure 65; $\boldsymbol{f_e}$ is the wave encounter frequency, and $\boldsymbol{f_r}$ is the main rotor rotational frequency [53]

Experimental investigations of the influence of ship motion on ship airwake were performed by Krebill [54] using a 1/77 scale model of the ONRT ship geometry in a water channel as shown in Figure 67. Heave and pitch motions were considered. These motions were applied at the CG of the ship model. PIV measurements were made for both static and dynamic ship configurations along the planes shown in Figure 68. Laser Doppler velocimetry (LDV) measurements at the point indicated in Figure 68 within PIV domain was used to verify the PIV measurements. Sea states #3 to #6 were investigated using different combinations of motion amplitude, frequency, and periods as indicated in Table 1. From the mean longitudinal and vertical velocity contours for the four sea states shown in Figure 69 and Figure 70, respectively, flow features remain similar between the sea states [54]. In this report, results from SS5 investigations will be considered.

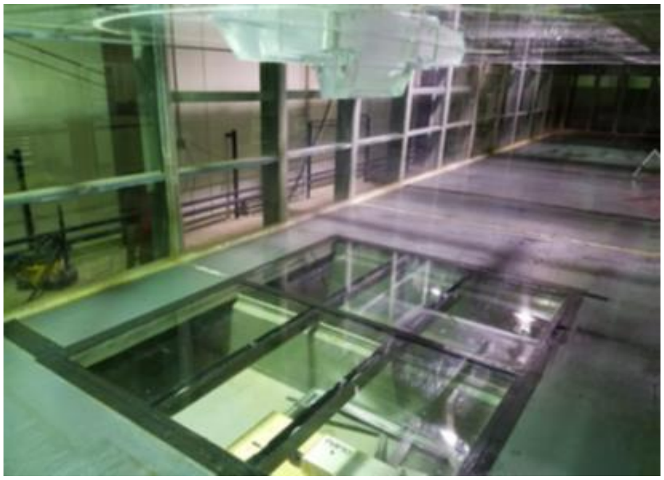

Figure 67: ONRT model in flume channel [54]

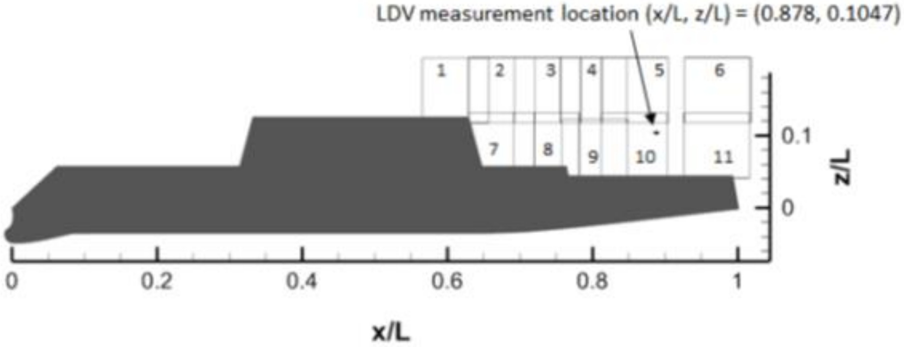

(a) static tests

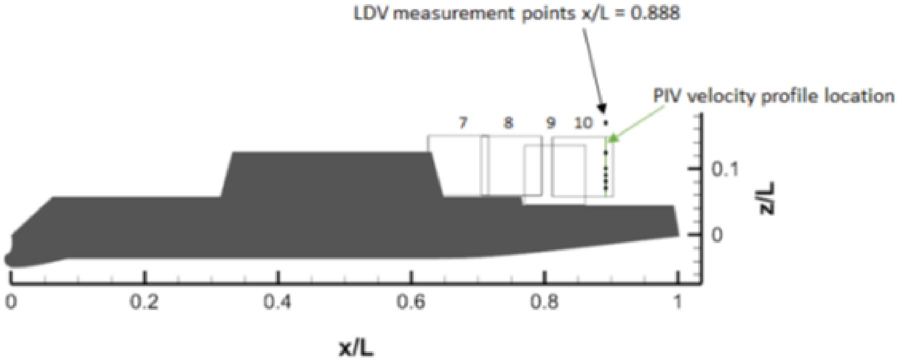

(b) dynamic tests

Figure 68: PIV and LDV measurement locations [54]

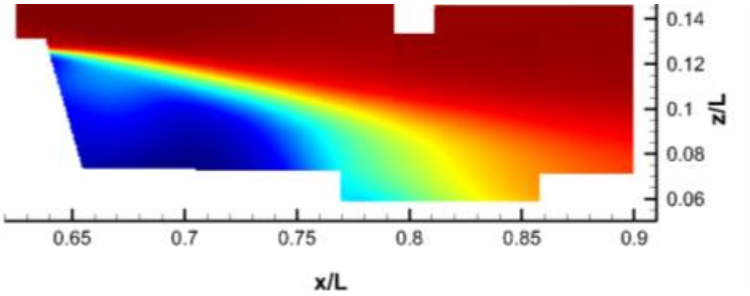

(a) SS3

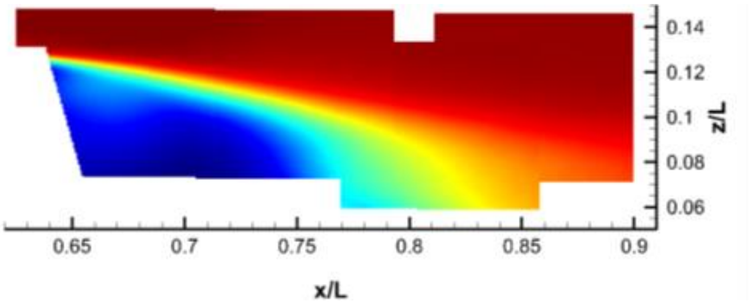

(b) SS4

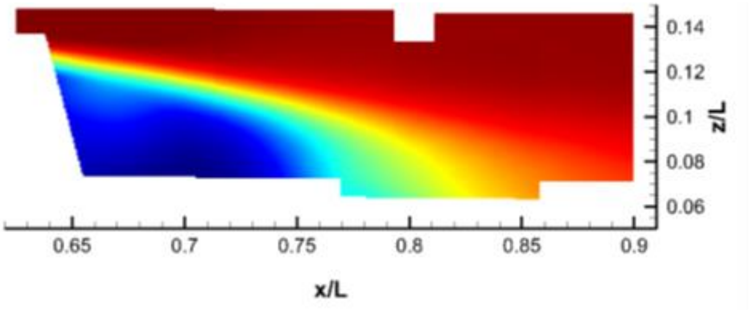

(c) SS5

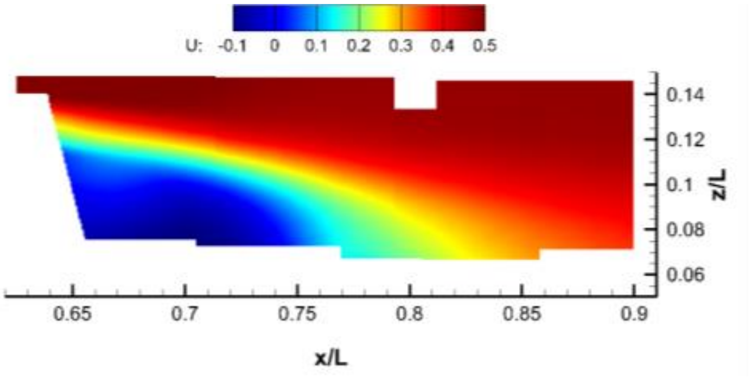

(d) SS6

Figure 69: Mean longitudinal velocity contours recorded during water channel experiments for SS3 to SS6; velocity values are given in meters-per-second [54]

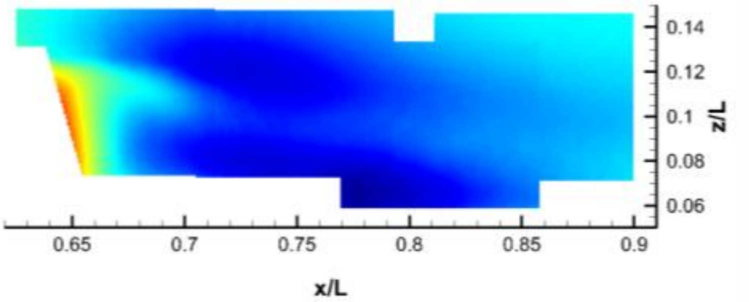

(a) SS3

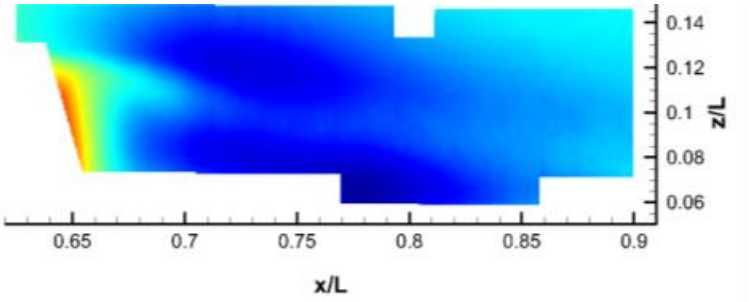

(b) SS4

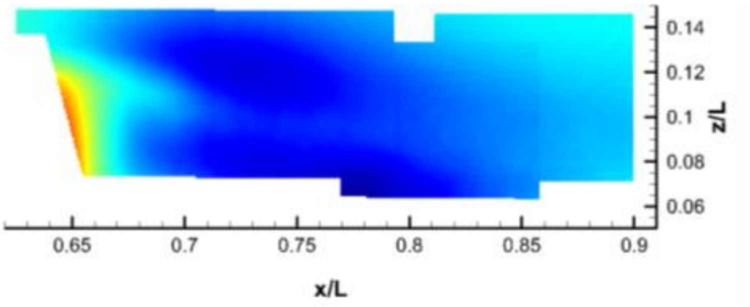

(c) SS5

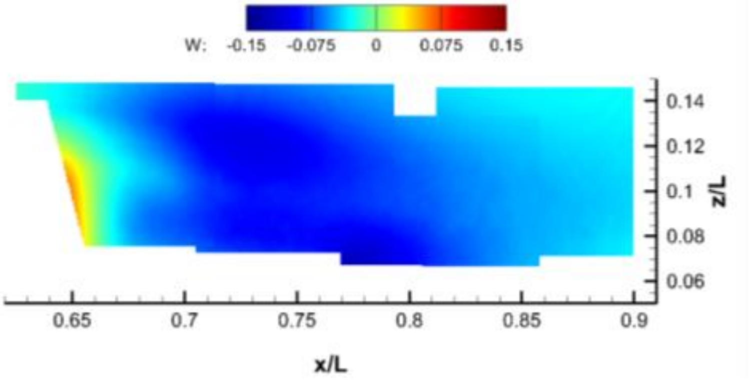

(d) SS6

Figure 70: Mean vertical velocity contours recorded during water channel experiments for SS3 to SS6; velocity values are given in meters-per-second [54]

Table 1: Test matrix used to emulate sea states #3 - #6 in Ref. [54]

Sea-State		***SS3***	***SS4***	***SS5***	***SS6***
Motion Frequency (Hz)		*0.33*	*0.28*	*0.26*	*0.17*
Motion Period (s)		*3.00*	*3.53*	*3.78*	*5.93*
Heave	***Amplitude (m)***	*0.00527*	*0.0082*	*0.0153*	*0.025*
	Offset from mean (m)	*-0.00141*	*-0.00141*	*-0.00139*	*-0.00147*
Pitch	***Amplitude (m)***	*1.07*	*1.50*	*2.49*	*3.58*
	Offset from mean (deg)	*-0.0734*	*-0.0783*	*-0.0947*	*-0.141*
	Lead (deg)	*37.2*	*43.3*	*53.3*	*59.0*

Mean longitudinal velocity contours at different phase angles[2] of ship motion are shown in Figure 71 [54], and illustrate that the shear layer impingement location translates up and down in the $0.77 \leq x/L \leq 0.85$ region of the deck during the motion. Mean vertical velocity contours at different phase angles of ship motion are shown in Figure 72 [54]. From the figure, the shear layer shed from the superstructure top-aft-edge juts into the recirculation region for phase angles 45° and 90°. The shear layer then starts receding to its original location from 135° onwards. Also evident from the figure is existence two distinct downwash regions separated by a smaller magnitude downwash region in the 90° and 135° phase contour plots, which are a consequence of the ship model changing directions.

Similar to the previous studies discussed in this section, Krebill observed airwake velocities at a position $(x/L, z/L) = (0.888{,}0.110)$ (see Figure 68) to be periodic with wave encounter frequency f_e for all sea states considered as shown in Figure 73 [54]. For SS5 and SS6, a secondary peak is evident at $2f_e$, which the author attributes the secondary peak to the measurement location going in and out of the two vertical velocity downwash regions shown in Figure 72 for phase angles of 90° and 135°. Krebill also examines mean velocities measured for static ship orientations corresponding to different phases of ship motion and notes larger velocity fluctuations in the static measurements, implying static tests provide conservative estimates of the influence of ship motion [54].

---

[2] Note that a definition of ship motion in terms of phase angle is not provided by the author. However, based on the translation of the shear layer impingement location in Figure 71, it is probable that motion is defined such that the ship bow pitches downward and the deck upwards between 0° and 180°, and in the opposite directions between 180° and 360°, with the switch in directions occurring at 90° and 270°.

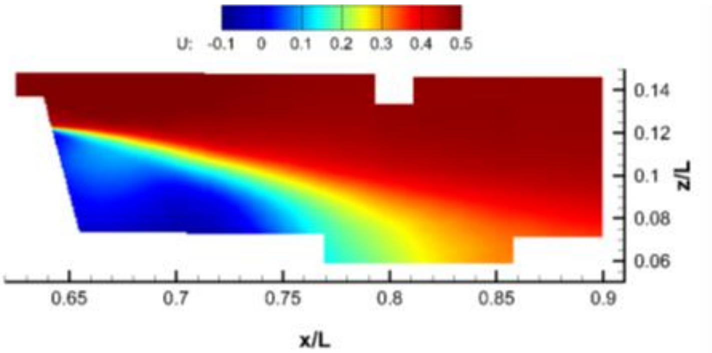

(a) 0°

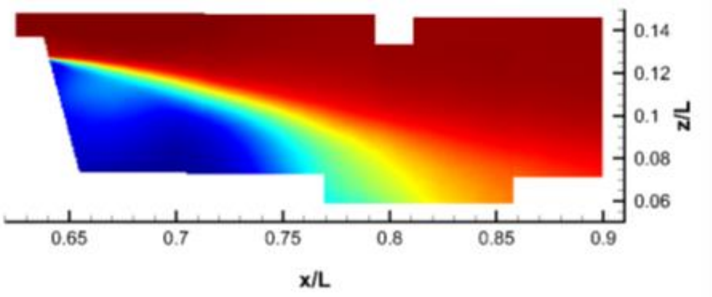

(b) 45°

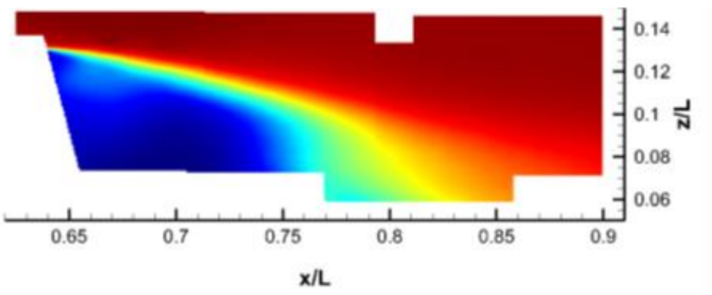

(c) 90°

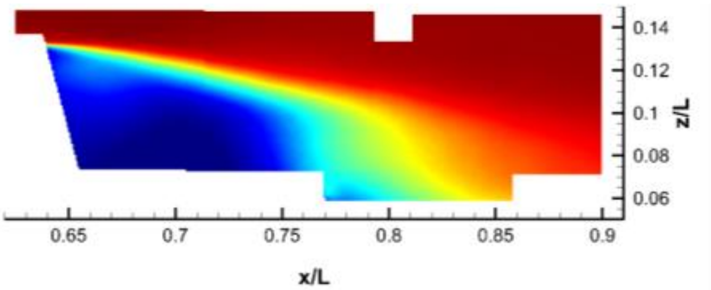

(d) 135°

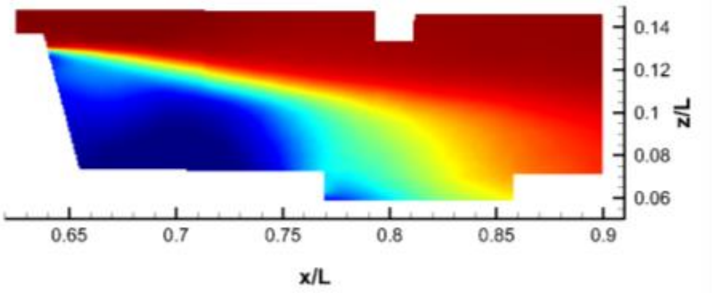

(e) 180°

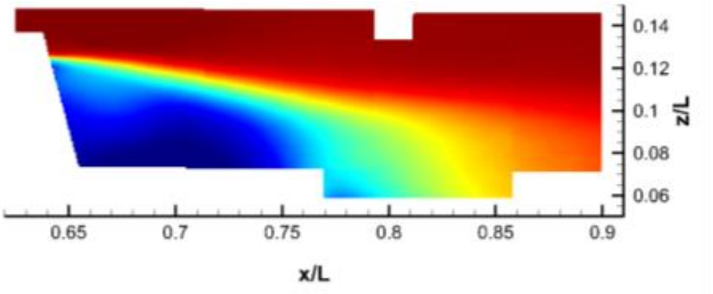

(f) 225°

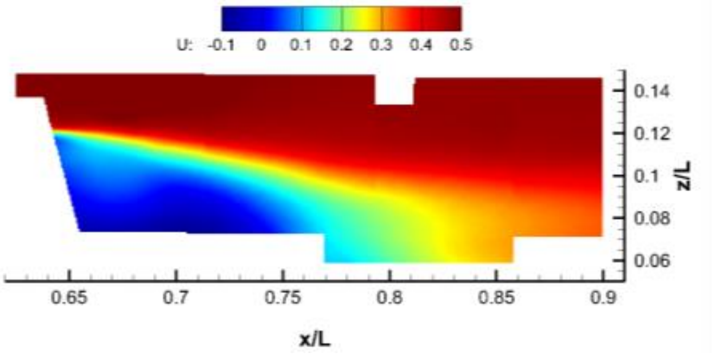

(g) 270°

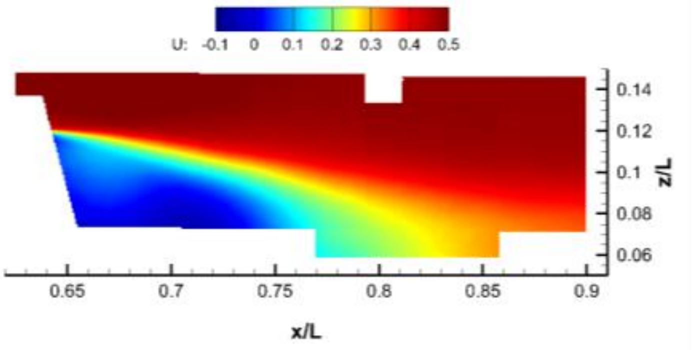

(h) 315°

Figure 71: Mean longitudinal velocity contours for different phase angles of ship motion; velocity values are given in meters-per-second [54]

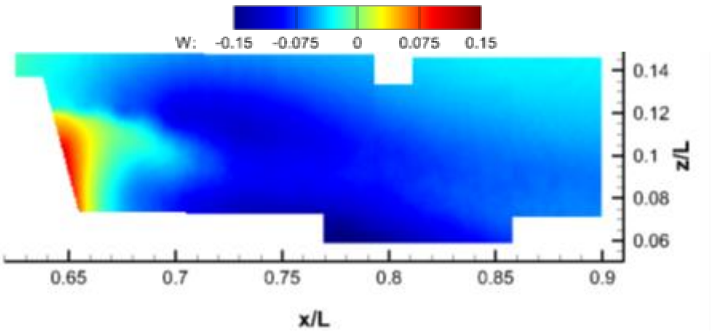

(a) 0°

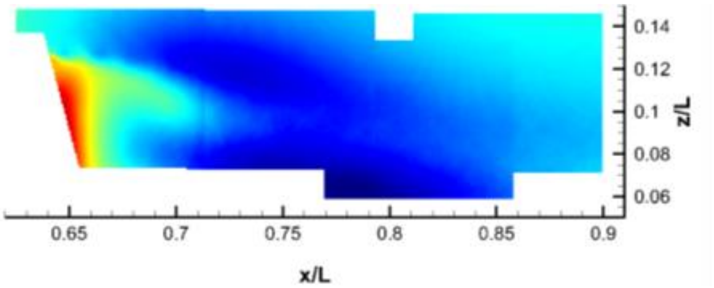

(b) 45°

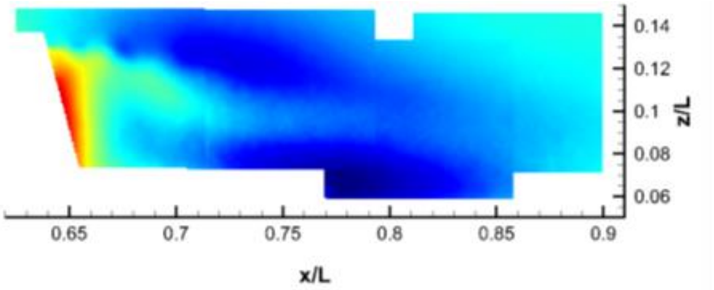

(c) 90°

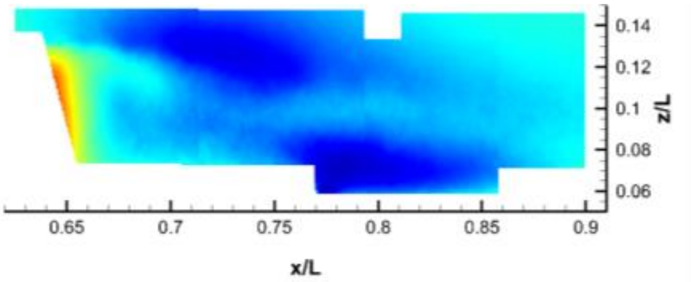

(d) 135°

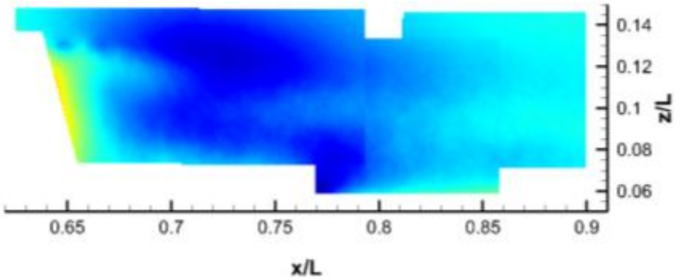

(e) 180°

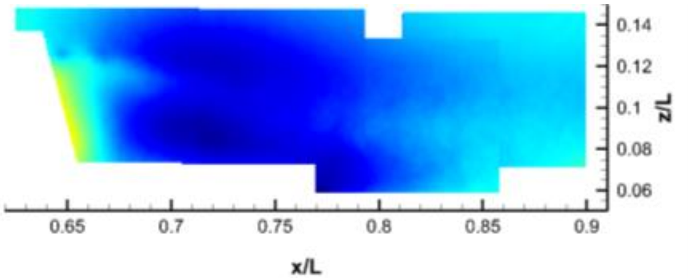

(f) 225°

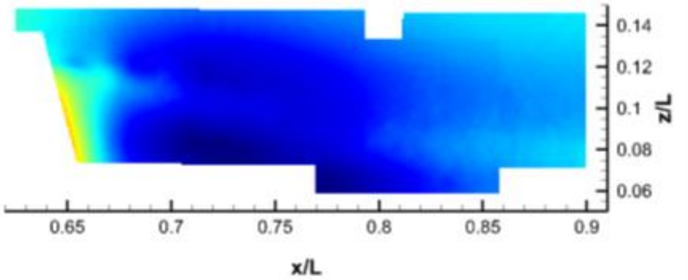

(g) 270°

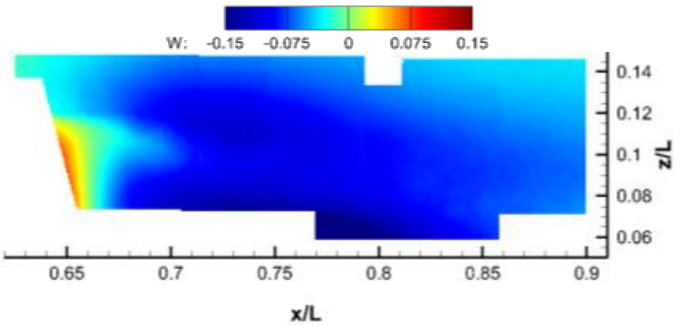

(h) 315°

Figure 72: Mean vertical velocity contours for different phase angles of ship motion; velocity values are given in meters-per-second [54]

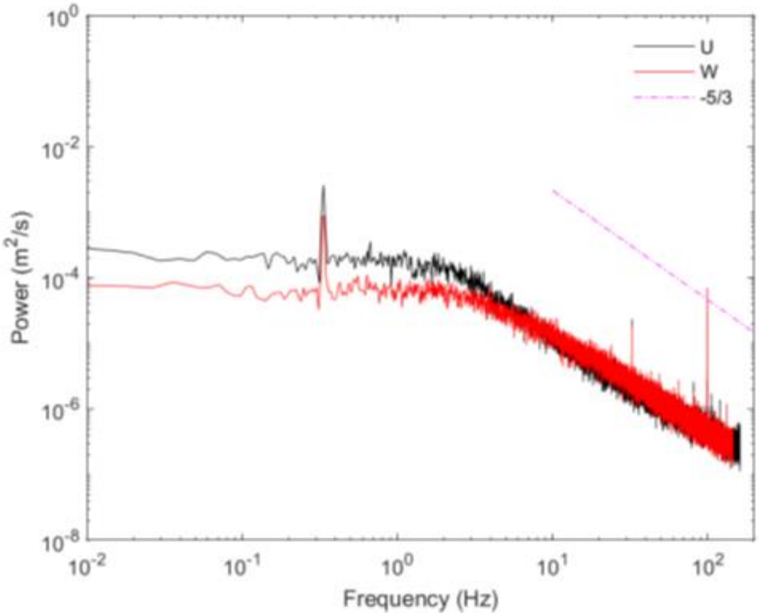
U
W
-5/3
Power (m^2/s)
10^0
10^{-2}
10^{-4}
10^{-6}
10^{-8}
10^{-2}
10^{-1}
10^0
10^1
10^2
Frequency (Hz)

(a) SS3

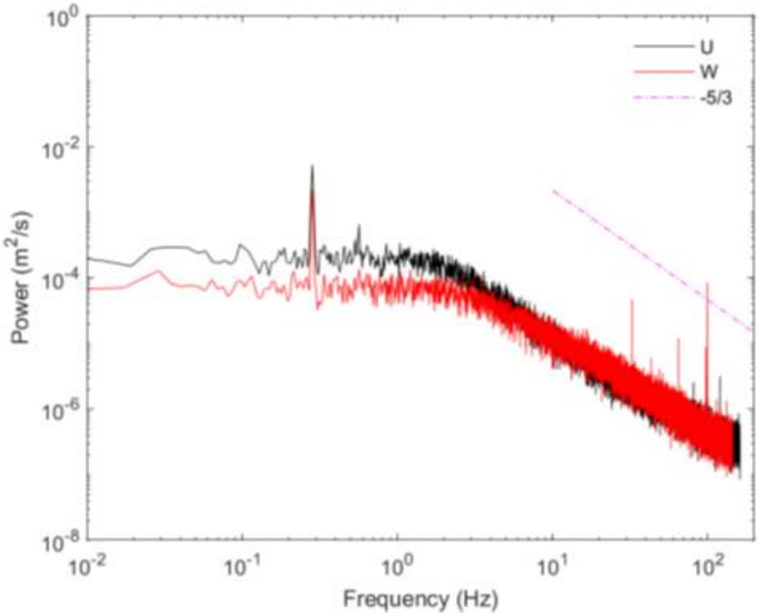
U
W
-5/3
Power (m^2/s)
10^0
10^{-2}
10^{-4}
10^{-6}
10^{-8}
10^{-2}
10^{-1}
10^0
10^1
10^2
Frequency (Hz)

(b) SS4

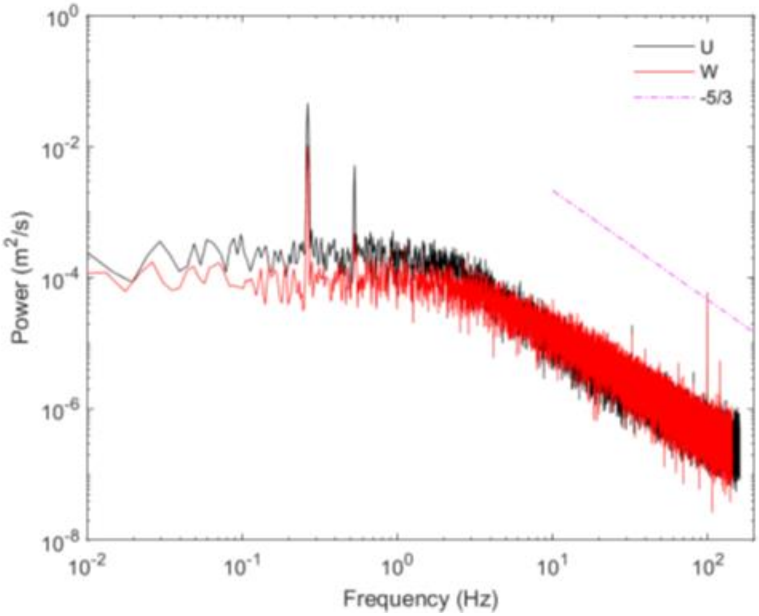

(c) SS5

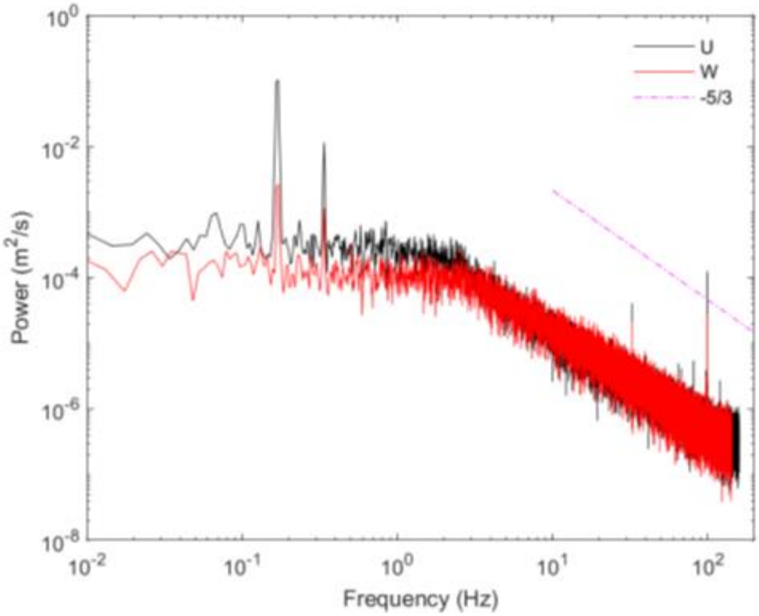

(d) SS6

Figure 73: Frequency spectra of longitudinal and vertical velocities recorded at $(\boldsymbol{x/L}, \boldsymbol{z/L}) = (\boldsymbol{0.888}, \boldsymbol{0.110})$ *(see Figure 68) during water channel experiments [54]*

Wake Parametrization

Work has been previously performed at CDI to parametrize fluctuating velocity components in the airwake of a landing helicopter assault (LHA) class ship to allow for predictions of flow unsteadiness to circumvent computational and data storage limitations associated with CFD based solutions [56]. The approach used a stochastic representation of the unsteady velocity components and a data reconstruction algorithm that preserved the spatial correlations relationships that resulted due to vortex structures in the ship airwake. Realistic velocity fluctuation predictions were obtained from the resulting model when compared to those obtained via CFD. The model however, was dependent on previously obtained CFD data and thus dependent on the configuration under consideration. A configuration independent methodology was proposed in an early publication by Woofield et al. [57], where flow over the edges and faces of a ship structure were first characterized as one of three fundamental flow patterns depending on the incoming wind direction: corner flow (further categorized as separated or vortex corner flow), lee rotor flow and profile drag flow, illustrated in Figure 74. Each flow patten was associated with a dataset of velocity increments which could be accessed for a given edge/surface and wind-over-deck angle. A simplified standard deviation-based turbulence model was also introduced but its influence during piloted simulation could not be assessed due to unforeseen simulation issues. The generic airwake model showed good agreement with wind tunnel velocity data in the transverse plane but discrepancies were noted in the streamwise plane. Despite the lack of turbulence, the authors note that favorable responses were obtained from pilots during helicopter-shipboard simulations with the generic model and emphasize the need for further testing of the methodology with more representative turbulence models.

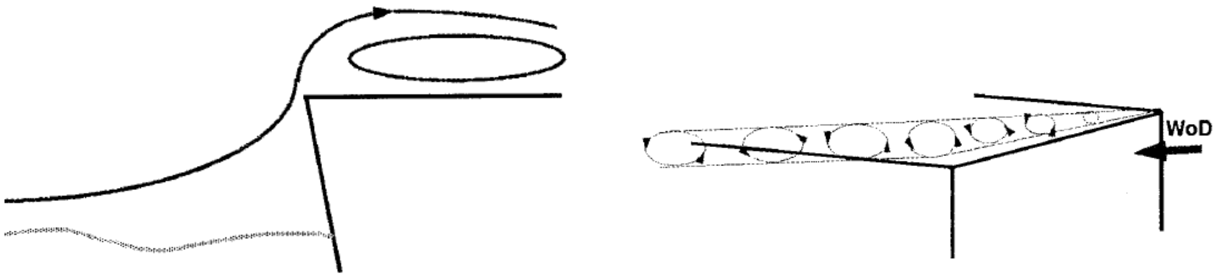

(a) separated corner flow

(b) vortex corner flow

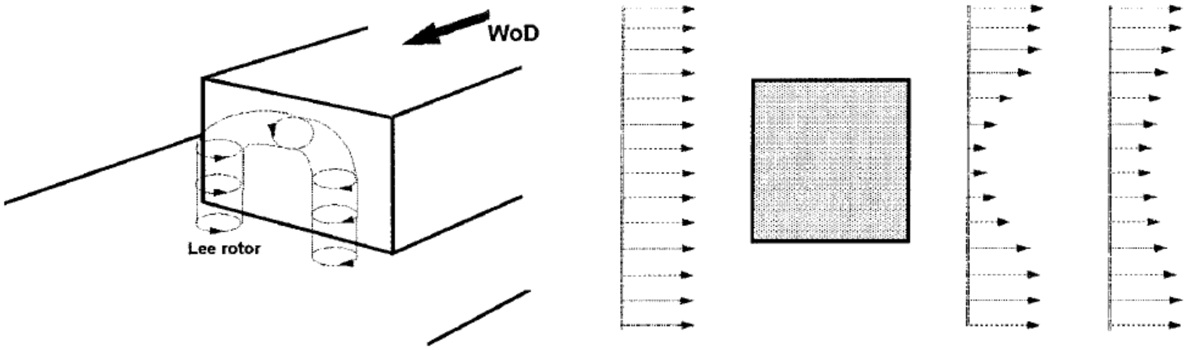

(c) lee rotor flow

(d) pressure drag flow

Figure 74: Flow patterns used to parametrize airwake in Ref. [57].

Generic airwake models have also been derived for flow over urban settings (e.g. Ref. [58]) and further review of relevant literature is needed at this point to identify parametrization techniques suitable for the project.

CFD Based Airwake Study

The literature review described above allows us to identify flow features that are of interest to the ship-helicopter DI scenario:

a) shear layers shed from edges of bluff body obstacles,
b) deck-edge vortices that develop due to pressure gradients between side and top surfaces, and
c) corner vortices that originate in oblique WOD conditions.

Steady characterization of these flow features in terms of Strouhal number, and unsteady characterization in terms of parameters such as turbulence intensity and TKE were provided where available in the literature.

To supplement these findings, CDI is undertaking CFD based airwake simulations using the CGE/VorTran-M CFD flow solver (see [59-61] for more detail). The results of these CFD predictions will be used to quantify the strength of the flow features of interest with respect to parameters such as wind speed, obstacle dimensions, upstream turbulence level and position relative to the obstacle. Characterization of vortices in terms of Strouhal number allows for scaling of dominant periodic flow features but does not provide information on the strength of these vortices. Quantifying and parametrizing the strength of dominant vortices is important to establish a fundamental understanding of the influence of ship airwake on aircraft dynamics and handling qualities. This quantification also represents an aspect of the ship-helicopter DI that has not been explicitly addressed in the literature. The CFD simulations will also be used to further investigate the flow features associated with corner winds, since the surveyed literature focused primarily on surface level pressure measurements. Spatial and temporal velocity distributions associated with corner winds will be assessed. Initial simulations will be performed for a wall-mounted rectangular prism. Results obtained using this configuration will be first checked against results from the surveyed literature before further assessment of vortex strengths and corner wind flow features is carried out.

Plans for the Next Reporting Period

In the next reporting period, we will build upon the understanding of the types of flowfields experienced by naval aviators described above and continue to quantify the scales and nature of the relevant primary flow structures based on the ongoing CFD predictions. Development of representative "canonical" surrogate flowfields will be undertaken. We will also request access to use NAVAIR/MFS' CASTLE simulation environment, the example helicopter model and the V-22 tiltrotor model for the duration of this project.

References

1. Smith, M.J., A. Jones, A. Grubb, and J. Lefebvre. *Identification and Quantification of the Role of Turbulence in Aircraft/Ship Aerodynamics*. *ONR Annual Review*. 2020. Arlingon, VA.
2. Silva, M.J., D.A. Wachspress, D.P. Gaublomme, E.W. Hayden, T.S. Davis, and T. Fean. *The Role of Modeling & Simulation in the Mitigation of V-22 Tiltrotor Formation Flight Wake-Induced Roll-off*. *72nd Annual Forum of the American Helicopter Society*. 2016. West Palm Beach, FL.
3. Whitehouse, G.R. and R.E. Brown. *Modelling a Helicopter Rotor's Response to Encounters with Aircraft Wakes*. in *28th European Rotorcraft Forum*. 2002. Bristol, UK.

4. Whitehouse, G.R. and R.E. Brown. *Helicopter Rotor Response to Wake Encounters in Ground Effect*. in *59th Annual Forum of the American Helicopter Society*. 2003. Phoenix, AZ.
5. Whitehouse, G.R. and R.E. Brown, *Modelling the Mutual Distortions of Interacting Helicopter and Aircraft Wakes.* Journal of Aircraft, 2003. **Vol. 40**(No. 3): p. pp. 440-449.
6. Whitehouse, G.R. and R.E. Brown, *Modelling a Helicopter Rotor's Response to Wake Encounters.* The Aeronautical Journal, 2004. **Vol. 108**(No. 1079): p. pp. 15-26.
7. Whitehouse, G.R., *Helicopter Response to Vortex Encounters in the Near-Airfield Environment*, 2003, PhD Thesis, Department of Aeronautics Imperial College London.
8. ADS-33E-PRF. *Aeronautical Design Standard Performance Specification Handling Qualities Requirements for Military Rotorcraft*. in *US Army Aviation and Missile Command, Aviation Engineering Directorate*. 2000. Redstone Arsenal, Alabama.
9. Hansen, A.C., J.A. Peterka, and Cermak.J.E., *Wind-Tunnel Measurements in the Wake of a Simple Structure in a Simulated Atmoshpheric Flow*, 1975: NASA-CR-2540.
10. Becker, S., H. Lienhart, and F. Durst, *Flow Around Three-Dimensional Obstacles in Boundary Layers.* Journal of Wind Engineering and Industrial Aerodynamics, 2002. **Vol. 90**(No. 4-5): p. pp. 265-279.
11. Forrest, J.S., I. Owen, G.D. Padfield, and S.J. Hodge, *Ship-Helicopter Operating Limits Prediction Using Piloted Flight Simulation and Time-Accurate Airwakes.* Journal of Aircraft, 2012. **Vol. 4**(No. 4): p. pp. 1020-1031.
12. Driver, D.M., H.L. Seegmiller, and J.G. Marvin, *Time-Dependent Behavior of a Reattaching Shear Layer.* AIAA Journal, 1987. **Vol. 25**(No. 7): p. pp. 914-919.
13. Eaton, J.K. and J.P. Johnston, *Review of Research on Subsonic Turbulent-Flow Reattachment.* AIAA Journal, 1981. **Vol. 19**(No. 9): p. pp. 1093-1100.
14. Eaton, J.K. and J.P. Johnston, *Low Frequency Unsteadiness of a Reattaching Turbulent Shear Layer*, in *Turbulent Shear Flows 3*. 1982, Springer. p. pp. 162-170.
15. Abbott, D.E. and S.J. Kline, *Experimental Investigations of Subsonic Turbulent Flow Over Single and Double Backward-Facing Steps.* ASME Journal of Basic Engineering, 1962. **Vol. 84**(No. 3): p. pp. 317-325.
16. De Brederode, V.A.S.L., *Three-Dimensional Effects in Nominally Two-Dimensional Flow.*, 1974, PhD Thesis, Imperial College of Science, Technology and Medicine.
17. Spazzini, P.G., G. Iuso, M. Onorato, N. Zurlo, and G.M. Di Cicca, *Unsteady Behavior of Back-Facing Step Flow.* Experiments in Fluids, 2001. **Vol. 30**(No. 5): p. pp. 551-561.
18. Kim, J., S.J. Kline, and J.P. Johnston, *Investigation of a Reattaching Turbulent Shear Layer: Flow Over a Backward-Facing Step.* Journal of Fluid Engineering, 1980. **Vol. 102**(No. 3): p. pp. 302-308.
19. Ma, X. and A. Schröder, *Analysis of Flapping Motion of Reattaching Shear Layer Behind a Two-Dimensional Backward-Facing Step.* Physics of Fluids, 2017. **Vol. 29**(No. 11).
20. Hoerner, S.F., *Fluid-Dynamic Drag*. 1965, New York, NY: Hoerner Fluid Dynamics.
21. Yu, D. and A. Kareem, *Parametric Study of Flow Around Rectangular Prisms Using LES.* Journal of Wind Engineering and Industrial Aerodynamics, 1998. **Vol. 77-78**: p. pp. 653-662.
22. Okajima, A., *Strouhal Numbers of Rectangular Cylinders.* Journal of Fluid Mechanics, 1982. **Vol. 123**: p. pp. 379-398.
23. Sousa, J.M.M., *Turbulent Flow Around a Surface-Mounted Obstacle Using 2D-3C DPIV.* Experiments in Fluids, 2002. **Vol. 33**(No. 6): p. pp. 854-862.

24. Hunt, J.C.R., C.J. Abell, J.A. Peterka, and H. Woo, *Kinematical Studies of the Flows Around Free or Surface-Mounted Obstacles; Applying Topology to Flow Visualization.* Journal of Fluid Mechanics, 1978. **Vol. 86**(No. 1): p. pp. 179-200.
25. Yakhot, A., H. Liu, and N. Nikitin, *Turbulent Flow Around a Wall-Mounted Cube: A Direct Numerical Simulation.* International Journal of Heat and Fluid Flow, 2006. **Vol. 27**(No. 6): p. pp. 994-1009.
26. Kim, K.C., H.S. Ji, and S.H. Seong, *Flow Structure around a 3-D Rectangular Prism in a Turbulent Boundary Layer.* Journal of Wind Engineering and Industrial Aerodynamics, 2003. **Vol. 91**(No. 5): p. pp. 653-669.
27. Herry, B., *Aerodynamic Study of a 3D Backward Facing Double Step Applied to Safer Launch and Recovery of Helicopters on Ships*, 2010, PhD Thesis, Université de Valenciennes et du Hainaut Cambrésis.
28. Larose, G.L. and A. D'Auteuil, *On The Reynolds Number Sensitivity of The Aerodynamics of Bluff Bodies With Sharp Edges.* Journal of Wind Engineering and Industrial Aerodynamics, 2006. **Vol. 94**(No. 5): p. pp. 365-376.
29. Healey, J.V., *Establishing A Database for Flight in the Wakes of Structures.* Journal of Aircraft, 1992. **Vol. 29**(No. 4): p. pp. 559-564.
30. Kareem, A., *Measurements of Pressure and Force Fields on Building Models in Simulated Atmospheric Flows.* Journal of Wind Engineering and Industrial Aerodynamics, 1990. **Vol. 36**(No. 1): p. pp. 589-599.
31. Tinney, C.E. and L.S. Ukeiley, *A Study of a 3-D Double Backward-Facing Step.* Experiments in Fluids, 2009. **Vol. 47**(No. 3): p. pp. 427-438.
32. Polsky, S. and C.W.S. Bruner. *A Computational Study of Unsteady Ship Airwake*. *NATO Research and Technology Organisation Applied Vehicle Technology Panel Symposium*. 2003. Leon, Norway: .
33. Cherry, B.E. and M.M. Constantino. *The Burble Effect: Superstructure and Flight Deck Effects on Carrier Air Wake*. *American Society of Naval Engineers Launch & Recovery Symposium 2010*. 2010. Arlington, VA.
34. Sezer-Uzol, N., A. Sharma, and L.N. Long, *Computational Fluid Dynamics Simulations of Ship Airwake.* Proceedings of the Institution of Mechanical Engineers, Part G: Journal of Aerospace Engineering,, 2005. **Vol. 219**(No. 5): p. pp. 369-395.
35. Forrest, J.S. and I. Owen, *An Investigation of Ship Airwakes Using Detached-Eddy Simulation.* Computers and Fluids, 2010. **Vol. 39**(No. 4): p. pp. 656-673.
36. Lee, D., N. Sezer-Uzol, J.F. Horn, and L.N. Long, *Simulation of Helicopter Shipboard Launch and Recovery with Time-Accurate Airwakes.* Journal of Aircraft, 2005. **Vol. 42**(No. 2): p. 448-461.
37. Polsky, S.A. and D.S. Miklosovic. *CFD Study of Bluff Body Wake From a Hangar With Comparison to Experimental Data*. *29th AIAA Applied Aerodynamics Conference*. 2011. Honolulu, HI: AIAA-2011-3351.
38. Polsky, S.A. and C. Bruner. *Time-accurate Computational Simulations of an LHA Ship Airwake*. in *18th AIAA Applied Aerodynamics Conference*. 2000. Denver, CO: AIAA 2000-4126.
39. Rajagopalan, G., D. Schaller, A.J. Wadcock, G.K. Yamauchi, J.T. Heineck, and M.J. Silva. *Experimental and Computational Simulation of a Model Ship in a Wind Tunnel*. *43rd AIAA Aerospace Sciences Meeting and Exhibit*. 2005. Reno, NV: AIAA-2005-1347.

40. Kumar, K.V., M.P. Mathew, S.N. Singh, S.S. Sinha, and R. Vijayakumar. *Experimental Investigation of Flow Over The Flight Deck of a Generic Aircraft Carrier*. *Warship 2018: Procurement of Future Surface Vessel*. 2018. London, UK: Royal Institution of Naval Architects.
41. Cvengros, M., *CFD Simulations of Unsteady LHA Ship Airwake in OpenFOAM*, 2018, Royal Institute of Technology: Stockhom, Sweden.
42. Kelly, M.F., *The Development, Validation, and Integration of Aircraft Carrier Airwakes for Piloted Flight Simulation*, 2018, University of Liverpool: Liverpool, UK.
43. Watson, N.A., M.F. Kelly, I. Owen, S.J. Hodge, and M.D. White, *Computational and Experimental Modelling Study of the Unsteady Airflow over the Aircraft Carrier HMS Queen Elizabeth.* Ocean Engineering, 2019. **Vol. 172**: p. pp. 562-574.
44. Kozmar, H., *Surface Pressure on a Cubic Building Exerted by Conical Vortices.* Journal of Fluids and Structures, 2020. **Vol. 92**.
45. Liu, T., H. Zhang, and D. Xin, *Experimental Study on Mitigating Extreme Roof Suctions by Passive Vortex Generators.* Journal of Wind Engineering and Industrial Aerodynamics, 2021. **Vol. 219**.
46. Asghari Mooneghi, M. and R. Kargarmoakhar, *Aerodynamic Mitigation and Shape Optimization of Buildings: Review.* Journal of Building Engineering, 2016. **Vol.6**: p. pp. 225-235.
47. He, J. and C.C.S. Song, *A Numerical Study of Wind Flow around the TTU Building and the Roof Corner Vortex.* Journal of Wind Engineering and Industrial Aerodynamics, 1997. **Vols. 67-69**: p. pp. 547–558.
48. Kawai, H., *Structure of Conical Vortices Related With Suction Fluctuation on a Flat Roof in Oblique Smooth and Turbulent Flows.* Journal of Wind Engineering and Industrial Aerodynamics, 1997. **Vol. 69-71**: p. pp. 579-588.
49. Kozmar, H., *Characteristics of Natural Wind Simulations in The TUM Boundary Layer Wind Tunnel.* Theoretical and Applied Climatology,, 2011. **Vol. 106**(No. 1-2): p. pp. 95-104.
50. Daley, W.H.I., *Flow Visualization of the Airwake Around a Model of a TAWARA Class LHA in a Simulated Atmospheric Boundary Layer*, 1988, Naval Postgraduate School: Monterey, CA.
51. Sydney, A.J., J.P. Ramsey, and J.I. Milluzzo. *Time-Resolved PIV Measurements of Ship Motion and Orientation Effects on Airwake Development*. *35th AIAA Applied Aerodynamics Conference*. 2017. Denver, CO: AIAA-2017-4230.
52. Yuan, W., A. Wall, and R. Lee. *Simulations of Unsteady Airwakes Behind Ships in Motion*. *31st Congress of the International Council of the Aeronautical Sciences*. 2018. Belo Horizonte, Brazil.
53. Dooley, G., J. Ezequiel Martin, J.H.J. Buchholz, and P.M. Carrica, *Ship Airwakes in Waves and Motions and Effects on Helicopter Operation,*. Computers and Fluids, 2020. **Vol. 208**.
54. Krebill, A., *Effect of Ship Motion on Ship Airwake Aerodynamics*, 2020, The Univeristy of Iowa: Iowa City, IA.
55. Tai, T. *Effect of Ship Motion on DD-963 Ship Airwake Simulated by Multizone Navier-Stokes Solution*. *Twenty-First Symposium on Naval Hydrodynamics*. 1997. Trondheim, Norway.

56. Keller, J.D., G.R. Whitehouse, and A.H. Boschitsch, *CFD Methodology Validation Report for Ship Airwake Model and Database*, 2007, CDI Report No. 07-04.
57. Woofield, A.A. and B.N. Tomlinson. *Ship Airwakes - A New Generic Model for Piloted Simulation*. *NATO AGARD Symposium on flight simulation – Where are the challenges?* 1995. AGARD-CP-577.
58. Kastner-Klein, P. and M.W. Rotach, *Mean Flow and Turbulence Characteristics in an Urban Roughness Sublayer*. Boundary-Layer Meteorology, 2004. **Vol. 111**(No. 1): p. pp. 55-84.
59. Keller, J.D., R.M. McKillip Jr., D.A. Wachspress, and T.B. Curbishley, *Model Based Aircraft Upset Detection and Recovery System*, 2007, CDI Report No. 07-07, Final Report Under Contract No. NNL07AA63P.
60. Keller, J.D., G.R. Whitehouse, A.H. Boschitsch, J. Nadal, J. Jeffords, and M. Quire. *Computational Fluid Dynamics for Flight Simulator Ship Airwake Modeling*. in *Interservice/Industry Training, Simulation, and Education Conference (I/ITSEC) 2007*. 2007. Orlando, FL.
61. Horn, J.F., J.D. Keller, G.R. Whitehouse, and R.M. McKillip Jr., *Analysis of Urban Airwake Effects on Heliport Operations at the Chicago Children's Memorial Hospital*, 2011, Illinois Department of Transportation http://www.dot.il.gov/aero/CMH/Analysis%20of%20Urban%20Airwake.pdf.